

THE EFFECTS OF ULTRASOUND ON CONVECTION-ENHANCED DELIVERY

A Dissertation

Presented to the Faculty of the Graduate School

of Cornell University

In Partial Fulfillment of the Requirements for the Degree of

Doctor of Philosophy

by

John Chee Keong Foo

May 2018

©2018 John Chee Keong Foo

THE EFFECTS OF ULTRASOUND ON CONVECTION-ENHANCED DELIVERY

John Chee Keong Foo, Ph.D.

Cornell University 2018

Neurological diseases such as glioblastoma multiforme are difficult to treat because the blood-brain barrier prevents most therapeutic drugs administered through the bloodstream from entering the brain. One way of overcoming this is by infusing the drug directly into the diseased site in the brain using either a needle or a cannula, a technique known as convection-enhanced delivery (CED). CED uses a pressure gradient to disperse the drug farther than if the drug were dispersed solely by diffusion. However, once the drug has been injected into the brain, physicians lose the ability to control the spatial distribution of the drug. Ultrasound focused via time-reversal acoustics (TRA) has been shown to further increase the distribution volume of CED infusions, raising the possibility that TRA-focused ultrasound may be used to direct the distribution of substances infused into brain tissue. In this dissertation, ultrasound focused adjacent to the infusion site did not appear to affect the distribution of Evans blue-labeled bovine serum albumin (EBA) in 0.2% wt/vol agarose gels or in vivo in the caudate putamen of rodent brains. Ultrasound focused at the site of infusion did not affect the distribution volumes of tracers when they were co-infused with microbubbles, but did significantly increase the distribution volume of EBA when it was co-infused with 20-nm, but not 40-nm, polystyrene particles. Results from a diffusion model suggest that ultrasound may have enhanced the convective phase rather than the diffusive phase of these infusions. Examination of rodent brain sections using fluorescence microscopy showed a distribution of EBA interspersed with regions of low Evans

blue intensity that coincided with axon bundles, suggesting that the distribution of substances in the caudate putamen is not uniform even within seemingly homogeneous gray matter. This may partially account for the disappointing results from advanced CED clinical trials so far.

BIOGRAPHICAL SKETCH

John Foo is a biomedical engineer and scientist with a passion for teaching and mentoring students. He credits his strong interest in science and math to the rigorous public education system in Singapore. John graduated from the University of Michigan with a B.S.E. in Biomedical Engineering and a minor in Japanese. He is currently honing his research and teaching skills by pursuing his Ph.D. in Biomedical Engineering at Cornell University. John lives in New York City with his husband and their Pomeranian.

To Daniel Hickey, for sharing this journey with me.

ACKNOWLEDGEMENTS

This dissertation would not have been possible without the support of so many people that creating a comprehensive list could very well result in a whole chapter of my thesis. This is instead a short list of those most directly involved in the development of this dissertation.

My dissertation committee—William Olbricht, Chris Schaffer, Ronald Harris Warrick, and Abraham Stroock—for guiding me to think like a scientist and illustrating the immense value of robust controls.

Peter Doerschuk and Jan Lammerding—for regularly checking in on my progress.

Belinda Floyd—What would I do without you? You handle everything else so I can focus on my research.

Armen Sarvazyan and Sergey Tsusaranov—for the development of the TRA-CED system and ongoing support.

Raghu Raghavan—for your ideas and guidance in the MRI project and the Ekos project.

Glenn Swan and Brian Bowman—for helping me design and build equipment to facilitate my research.

Wen Ming Luh—for helping me develop my MRI protocol.

Olbricht lab, especially:

Justin Rosch—you have been an integral part of my life at Cornell, both in and out of the lab.

I'm so privileged to have you as my lab mate, friend, and... radio show co-host!

Austin Jarrett, Carrie D'Aprix, and Sruthi Chandran—for assisting me with so many experiments! Experiments are also way more fun when you're around.

George Lewis and Manjari Sistla—for all your advice on ultrasound and the related work from our lab.

Schaffer-Nishimura Labs, especially:

Mohammad Haft Javaherian—for helping me figure out the most efficient way to analyze my data. You easily saved me an additional six months of coding and debugging.

George Calvey—for helping me ablate piezoelectric discs into microscopic pieces.

Wang lab, especially:

Cynthia Wisnieff—for patiently introducing me to MRI and QSM, and helping me develop my experiment protocol.

Zhe Liu—for helping me troubleshoot my protocol and data analysis, and staying with me overnight at the NYC MRI facility so I could get all my scans done before the 6 AM C2C bus leaves.

Adie Lab, especially:

Jeffrey Mulligan—for our discussions about science and teaching as well as your patient explaining of signal processing and other wave concepts to me.

Akanksha Agrawal—for helping me with my viscosity measurements.

Rohit Singh—for showing me how to use the ZetaSizer, repeatedly.

Shivaun Archer, Iwijn DeVlaminck, David Lipson, and Bruce Johnson—for giving me multiple opportunities to grow as an educator.

CTI and CIRTl, especially:

Derina Samuel—for accepting me into the GTAF program, which has since unlocked many teaching and professional development opportunities for me.

Kimberly Williams—for helping me develop and implement my two Teaching-as-Research projects.

Colleen McLinn—for providing professional development opportunities and external venues to present my work.

Elliot Shapiro and David Faulkner—for giving me the opportunity to develop and teach my very own First-Year Writing Seminar!

ELI, especially:

Linda Tompkins—for building my confidence in my abilities and helping me develop as both a team player and a leader.

Anne Poduska—for helping me develop further as a leader and your advice in navigating the complexities of grad school and the job market.

COE and CTLC, especially:

Amy Kohut—Leaping off a 30 ft. telephone pole when you're terrified of heights? Check.

Annie Socci—Survive a night alone at the Boundary Waters Canoe Area Wilderness at -20 °F? Check.

Chris Leeming—Empower a group of undergraduates to survive a weekend in the wilderness with just a knife and a water bottle? Check. Ph.D., bring it on!

Jan Allen and Janna Lamey—for providing support and resources like the Perspective Series and the Academic Writing Bootcamp.

Bailey Cooper and Meghnaa Tallapragada—for helping me with my Flipped Classroom Teaching-as-Research project.

Samson Lai—for your encouragement and guidance since before I even started grad school.

The Cornell and Ithaca community— for banding together to help Dan and me after our apartment burned down. Many people helped us with donations and other means. In particular, I thank:

John Novarr—for giving us and the other displaced students a free place to stay for the remainder of that semester.

Liz Wayne—for organizing a GoFundMe for us and making sure we were not overwhelmed.

Gregory Fedorchek—for raising donations for us.

Justin Rosch, Lindsey Crawford, and Rambert Nahm—for buying us food, supplies and the Minions and orange T-shirts.

Aniqua Rahman—for buying us supplies.

Daniel J. and Irene Hickey—for buying us supplies and clothing.

Amy Kohut and Carol James—for providing support and checking in on us.

Red Cross—for immediate necessities and a voucher to replace my glasses.

ISSO—for emergency funds to help get us back on our feet.

Everyone who helped me in preparing for my B Exam, especially:

Alexandra McGregor and Gregory Fedorchek—for setting up the room and the refreshments so I could focus on my exam.

Gregory Fedorchek, Jason Jones, Mitch Pender, Nozomi Nishimura, David Small, Oliver Bracko, Mohammad Haft Javaherian, Yu-Ting Cheng, Jiahn Choi, Daniel Rivera, and Jeffrey Mulligan—for all the helpful feedback on my practice B Exam.

Jane Foo—for knowing just the right time to check in.

All my family and friends—for always being there when I need you.

Portions of this work were supported by the NIH grants 1R21CA164935 and 1S10RR025145.

I have been personally supported by the McMullen Fellowship, Howard Hughes Medical Institute Med-into-Grad Fellowship, John S. Knight Buttrick-Crippen Fellowship, Engineering Learning Initiatives Fellowship, and teaching assistantships from the Nancy E. and Peter C. Meinig School of Biomedical Engineering and the Robert Frederick Smith School of Chemical and Biomolecular Engineering.

TABLE OF CONTENTS

1	INTRODUCTION	1
2	EVALUATING THE EFFECTS OF CONVECTION AND DIFFUSION ON A GADOLINIUM TRACER IN CONVECTION-ENHANCED DELIVERY	14
2.1	Introduction	14
2.2	Materials and Methods	16
2.2.1	Agarose Gel Phantom	16
2.2.2	Gadolinium Infusion and MRI Scans	16
2.2.3	Post-processing MRI scans	17
2.2.4	Modeling the diffusion and convection of gadolinium from a continuous point source in water	20
2.3	Results	22
2.3.1	Gadolinium concentration profiles from MRI scans	22
2.3.2	Gadolinium distribution volume and V_d/V_i from MRI scans	26
2.3.3	Gadolinium concentration profiles derived from pure diffusion model	29
2.3.4	Gadolinium distribution volumes and radii derived from pure diffusion model	30
2.4	Discussion	33
2.4.1	Limitations of the MRI protocol using quantitative susceptibility mapping	36
2.5	Conclusion.....	36

3	THE EFFECT OF TIME-REVERSAL ACOUSTICS FOCUSED ULTRASOUND ON THE DISTRIBUTION OF CONVECTION-ENHANCED DELIVERED DYE AND MICROBUBBLES IN AGAROSE GELS AND RAT BRAINS	37
3.1	Introduction	37
3.2	Materials and Methods	39
3.2.1	Development of the TRA-focused ultrasound system and needle hydrophones	39
3.2.2	Preparation of Tracers.....	40
3.2.3	Characterization of the Region of Ultrasound Focus in Water and Agarose Gel...	41
3.2.4	Characterization of the Region of Ultrasound Focus in the Rat Brain In Vivo	44
3.2.5	Agarose Gel Experiments with Ultrasound Focused Adjacent to Site of Infusion.	46
3.2.6	Imaging and Image Analysis of Agarose Gel Experiments.....	48
3.2.7	In Vivo Rat Experiments with Ultrasound Focused Adjacent to or at Site of Infusion.	48
3.2.8	Imaging and Image Analysis of In Vivo Rodent Experiments	55
3.2.9	Statistical Analysis.....	56
3.3	Results	57
3.3.1	Characterization of the Region of Ultrasound Focus in Water and Agarose Gel...	57
3.3.2	Characterization of the Region of Ultrasound Focus in the Rat Brain In Vivo	64
3.3.3	Agarose Gel Experiments with Ultrasound Focused Adjacent to Site of Infusion.	68

3.3.4	In Vivo Rat Experiments with 0.5 MHz Ultrasound Focused Adjacent to Site of Infusion.	71
3.3.5	In Vivo Rat Experiments with 0.5 or 1 MHz Ultrasound Focused at the Site of Infusion.	82
3.4	Discussion	86
3.4.1	Possible implications due to differences in the needle hydrophone	87
3.4.2	Possible implications due to differences in the TRA setup	88
3.4.3	Possible implications due to differences in the type of microbubbles or dye used	89
3.5	Conclusion.....	92
4	THE EFFECT OF TIME-REVERSAL ACOUSTICS FOCUSED ULTRASOUND ON THE DISTRIBUTION OF CONVECTION-ENHANCED DELIVERED DYE AND POLYSTYRENE NANOPARTICLES IN RAT BRAINS	94
4.1	Introduction	94
4.2	Materials and Methods	96
4.2.1	Preparation of Tracers.....	96
4.2.2	Animal Surgery and Experiment	99
4.2.3	Imaging and Image Analysis	100
4.2.4	Assessing the distribution of EBA using the Reflectance Images	100
4.2.5	Assessing the concentration profiles of EBA using the Reflectance Images	103

4.2.6	Assessing the distribution of EBA and 20-nm and 40-nm polystyrene particles using Fluorescence Microscopy.....	108
4.2.7	Statistical Analysis.....	109
4.3	Results.....	109
4.3.1	Assessing the mean distribution volumes and V_d/V_i ratios of EBA from the Reflectance Images.....	109
4.3.2	Assessing the concentration profiles of EBA from the Reflectance Images.....	113
4.3.3	Assessing the mean distribution volumes of EBA and the 20-nm and 40-nm polystyrene particles using Fluorescence Microscopy.....	115
4.4	Discussion.....	119
4.4.1	Limitations of the model of diffusion from an instantaneous spherical source of constant concentration.....	122
4.5	Conclusion.....	123
5	ASSESSING THE DISTRIBUTION OF EVANS BLUE-LABELED BOVINE SERUM ALBUMIN INFUSED VIA CONVECTION-ENHANCED DELIVERY INTO THE RAT CAUDATE PUTAMEN.....	124
5.1	Introduction.....	124
5.2	Materials and Methods.....	125
5.2.1	Animal Surgery and Infusion.....	126
5.2.2	Histochemical Staining.....	126

5.2.3	Imaging and Image Analysis	127
5.2.4	Statistical Analysis.....	128
5.3	Results	128
5.3.1	Co-localization of low Evans blue intensity circular and oval regions with high Fluoromyelin intensity regions	128
5.3.2	Comparison of Evans blue fluorescence intensity within and outside the axon bundle.....	134
5.4	Discussion	137
5.5	Conclusion.....	139
6	EVALUATION OF RADially-EMITTED ULTRASOUND ON THE DISTRIBUTION OF EVANS BLUE DYE ADMINISTERED VIA CONVECTION-ENHANCED DELIVERY IN A MILK-AGAROSE BRAIN PHANTOM	141
6.1	Introduction	141
6.2	Materials and Methods	142
6.2.1	Ultrasonic catheter	143
6.2.2	Infusions into milk-agarose gel.....	143
6.2.3	Imaging and Analysis	146
6.3	Results	147
6.3.1	Characterization of ultrasonic catheter	147
6.3.2	Distribution volumes of 1% Evans blue dye in milk-agarose gels.....	150

6.4	Discussion	152
6.5	Conclusion.....	154
7	STUDENT ADAPTATION TO THE MODULAR USE OF THE FLIPPED CLASSROOM IN AN INTRODUCTORY BIOMEDICAL ENGINEERING COURSE.....	155
7.1	Introduction	155
7.2	Methods.....	158
7.2.1	The Flipped Biotransport Module.....	158
7.2.2	Data collection	161
7.2.3	YouTube Viewership Data	161
7.2.4	Online Survey	161
7.2.5	Classroom Observations	162
7.3	Results	162
7.3.1	Results from YouTube Viewership Data.....	162
7.3.2	Results from online survey	165
7.3.3	Demographic Information.....	165
7.3.4	Prior Experience with the Flipped Classroom model	165
7.3.5	Student Perceptions about the use of the Flipped Classroom model for the Biotransport Module	166
7.3.6	Student Suggestions to make the Biotransport Module more conducive for learning.	170

7.3.7	Student Suggestions to make the transition to the Flipped Module smoother.....	172
7.3.8	Results from Student Work.....	173
7.3.9	Results from Classroom Observations.....	175
7.3.10	Instructor Reflections on Flipping the Classroom	175
7.4	Discussion	176
7.5	Conclusions	178
7.6	Acknowledgements	178
8	REFERENCES	180

LIST OF FIGURES

Figure 1.1: Using time-reversal acoustics to focus ultrasound.....	7
Figure 1.2: The components of the TRA-CED system.....	9
Figure 2.1: Agarose gel phantom for MRI.....	19
Figure 2.2: Mean gadolinium concentrations along the vertical axis.....	23
Figure 2.3: Mean gadolinium concentrations along the left-right horizontal axis.....	24
Figure 2.4: Mean gadolinium concentrations along the anterior-posterior horizontal axis.....	25
Figure 2.5: Mean distribution volumes during and after the infusion.....	27
Figure 2.6: Mean V_d/V_i during the infusion.....	28
Figure 2.7: Gadolinium concentration profiles based on diffusion model.....	31
Figure 2.8: Comparison of distribution volumes and radii.....	32
Figure 3.1: Coordinate system based on position of reverberator.....	43
Figure 3.2: In vivo rat brain experimental setup.....	45
Figure 3.3: Agarose gel experimental setup.....	47
Figure 3.4: Acoustic pressure profiles of focused 0.5 MHz ultrasound at $\pm 1.5V$ in water.....	59
Figure 3.5: Acoustic pressure profiles of focused 0.5 MHz ultrasound at $\pm 45V$ in water.....	60
Figure 3.6: Acoustic pressure profiles of focused 1 MHz ultrasound at $\pm 3V$ in water.....	61
Figure 3.7: 2D acoustic pressure profile of focused 0.5 MHz ultrasound at $\pm 1V$ in water.....	62
Figure 3.8: Complex-shape focal region of 0.5 MHz ultrasonic waves.....	63
Figure 3.9: Acoustic pressure profiles of focused 0.5 MHz ultrasound at $\pm 1.8V$ in rat brain.....	65
Figure 3.10: XY acoustic pressure profile of focused 0.5 MHz ultrasound at $\pm 1.8V$ in rat brain.....	66
Figure 3.11: XZ acoustic pressure profile of focused 0.5 MHz ultrasound at $\pm 1.8V$ in rat brain.....	67

Figure 3.12: Representative ultrasound and no-ultrasound control experiments in agarose gel ..	69
Figure 3.13: Right/left radii and area ratios of distribution volumes.....	70
Figure 3.14: Mean distribution volumes of EBA in rat brain, focus adjacent to needle tip	72
Figure 3.15: Mean rostral:caudal V_d ratios of EBA in rat brain, focus adjacent to needle tip.	73
Figure 3.16: Mean distribution volumes of EBA, unsonicated, with and without microbubbles. 74	
Figure 3.17: Mean dyed areas of rat brain slices along Caudal-Rostral axis, all experiments	75
Figure 3.18: Mean dyed areas of rat brain slices along Caudal-Rostral axis, 8MPa, 2 mm.....	76
Figure 3.19: Mean dyed areas of rat brain slices along Caudal-Rostral axis, 8MPa, 1 mm.....	77
Figure 3.20: Mean dyed areas of rat brain slices along Caudal-Rostral axis, 8MPa, no μ B.	79
Figure 3.21: Mean dyed areas of rat brain slices along Caudal-Rostral axis, 1 mm, μ B.....	80
Figure 3.22: Mean distribution volumes of EBA, focus at needle tip	84
Figure 3.23: Mean distribution volumes of EBA vs EB.....	85
Figure 4.1: Reflectance intensity line profile and fitting to diffusion model.....	104
Figure 4.2: EBA-dyed areas in brain sections containing the tip of the infusion needle.....	111
Figure 4.3: Mean dyed areas of rat brain slices along Caudal-Rostral axis, 0.2MPa.....	112
Figure 4.4: Means of D^* and a from diffusion model	114
Figure 4.5: Fluorescent images of brain slices in TxR and TRITC channels.....	116
Figure 4.6: Mean EBA distribution volumes based on fluorescent and reflectance images	117
Figure 4.7: Mean nanoparticle distribution volumes	118
Figure 5.1: Fluorescent images of rat caudate putamen with Fluoromyelin.....	130
Figure 5.2: Fluorescent images of rat caudate putamen without Fluoromyelin	131
Figure 5.3: Aligned images of Evans blue channel of a single rat.	133
Figure 5.4: Means of Evans blue and Fluoromyelin In/Out fluorescence intensity ratios	136

Figure 6.1: Experimental setup with ultrasonic catheter	145
Figure 6.2: 1D acoustic pressure profile of ultrasonic catheter	148
Figure 6.3: Radial ultrasound moved dye up to 3.5 mm away from tip of catheter.	149
Figure 6.4: Mean distribution volumes of Evans blue	151
Figure 7.1: Screenshot of the Intro to Biofluid Transport video lecture.....	160
Figure 7.2: Student response to use of Flipped Classroom model.....	167
Figure 7.3: Student response to different aspects of the biotransport module.....	168
Figure 7.4: Student response to transition and adaptation to Flipped Classroom.....	169

LIST OF TABLES

Table 2.1: Summary of parameters for model of diffusion from a continuous point source.....	21
Table 3.1: Summary of μ B experiment parameters, ultrasound focused adjacent to infusion site	52
Table 3.2: Summary of μ B experiment parameters, ultrasound focused at infusion site	53
Table 3.3: Characteristics of microbubbles used in in vivo rat brain experiments.....	54
Table 4.1: Mean diameters and ζ -potentials of EBA and BSA-coated nanoparticles.	98
Table 4.2: Summary of nanoparticle experiment parameters	102
Table 4.3: Summary of parameters for fitting line profile data to diffusion model.....	107
Table 7.1: YouTube data on viewership of video lectures.	164
Table 7.2: Pre-class online quiz response rate	174

CHAPTER 1

INTRODUCTION

Despite advances in medicine, many diseases afflicting the brain remain difficult to treat. For example, the most common malignant tumor affecting the adult human brain is glioblastoma multiforme¹. Even with surgical debulking, radiation therapy, and the increasing number of chemotherapeutic drugs available, patients with this highly aggressive tumor face dismal odds—only a third survive the first year after diagnosis, and the likelihood of survival only continues to plunge further^{1,2}. Complete resection of the primary tumor is made difficult due to the invasive nature of gliomas, and nearly all patients experience a recurrence of the tumor close to the original site^{3,4}.

One major reason that brain diseases are so difficult to treat is the presence of the blood-brain barrier. Unlike blood capillaries in the rest of the body, the endothelial cells lining the capillaries of the brain are connected by tight junctions, which allow only very small molecules to pass from the bloodstream into brain tissue⁵. While the blood-brain barrier prevents many blood-borne pathogens from entering the brain, it also prevents many drugs that patients with brain diseases need from passing through as well. Only very small (<400 Da) lipophilic drugs can easily pass through the blood-brain barrier, severely limiting the chemotherapeutic drug options for patients⁵⁻⁷. Of the drugs that can bypass the blood-brain barrier, the systemic concentration required to achieve a therapeutic dose in the brain may be too toxic⁸.

Attempts to bypass the blood-brain barrier using drug-releasing wafer implants have had little success. Gliadel wafers have been implanted in the resection cavity of glioblastoma patients to deliver the chemotherapeutic drug BCNU, but the rate of drug elimination far outpaces its diffusion in the brain, resulting in only a few millimeters of drug penetration that is insufficient to kill all the remaining cancer cells⁹.

One promising delivery method to bypass the blood-brain barrier is convection-enhanced delivery (CED)^{10,11}. This method involves infusing the drug of choice directly to the diseased brain tissue via a needle or catheter. This targeted delivery reduces the exposure of healthy tissue to the toxic drug, while the pressure gradient generated by the infusion forces the drug to penetrate further into the diseased tissue than is possible by diffusion alone. For example, MRI studies have shown that CED can achieve distribution volumes more than five times the volume of infusion in non-human primate brains¹². In addition, CED allows the local delivery of these chemotherapeutic agents, thereby potentially reducing the systemic toxic effects of the treatment.

However, advanced clinical trials involving CED, including the only two Phase III studies conducted so far, have had disappointing results¹³⁻¹⁶. The Phase III TF-CRM107 study, which involved the delivery of a human transferrin (TF) conjugated to a diphtheria toxin (CRM107), was aborted after an intermediate analysis showed a dismal response rate of 39%¹⁶. While the Phase III Randomized Evaluation of CED of IL13-PE38QQR with Survival Endpoint (PRECISE) trial comparing CED-delivered cintredekin besudotox with Gliadel wafers implants for the treatment of glioblastoma multiforme was completed, it found no significant difference in the median survival between both groups of patients¹⁵. A third clinical trial, the Phase III

SAPPHIRE study, was terminated at the recruitment stage for not being able to recruit the projected number of patients¹⁷. Despite the potential of this delivery modality as demonstrated from animal studies and even some Phase I/II clinical trials, ultimately, the increases in drug distribution and concentration from CED remain insufficient. A retrospective study analyzing diffusion tensor magnetic resonance images from the PRECISE trial estimated that, on average, only a fifth of the 2-cm region surrounding the resection cavity that is at highest risk of recurrence was covered by the drug¹³. A further limitation of CED is that once the drug has been infused into the brain tissue, doctors lose the ability to control the subsequent path the drug takes¹⁸.

One potential method to further increase drug distribution and concentration is through the use of ultrasound. Ultrasound is sound or pressure waves with frequencies above the audible range for humans, i.e., above 20 kHz. Common diagnostic ultrasound applications such as fetal monitoring typically employ frequencies above 3 MHz, whereas therapeutic ultrasound applications such as blood-brain barrier disruption often use frequencies between 20 kHz to 3 MHz, although there are many exceptions¹⁹⁻²¹.

Ultrasound has been shown to improve the delivery of molecules across different tissues, including those delivered to the brain via CED²²⁻²⁵. Potential mechanisms have included increasing the permeability of the tissue, acoustic radiation force, mixing from cavitation, and heating. For example, by measuring the electrical conductivity across sagittal tissue sections, Liu et al. (2010) found that four-hour applications of unidirectional ultrasound at therapeutic frequencies to porcine brain and human brain tumor tissues in vitro increased the permeability of

the tissue to a variety of molecules, including the chemotherapeutic drug BCNU. Additionally, the application of unidirectional unfocused ultrasound in vivo increased the distribution of liposomes administered via CED into the corona radiata of a non-human primate²².

Lewis et al. (2010) not only demonstrated that ultrasound can increase the distribution of infused Evans blue dye in rodent brains, they also fortuitously created standing waves in two rat brains that resulted in the dye forming bands in intervals that matched the node-to-node or antinode-to-antinode distance of the standing waves²⁴. This formation of bands of infused dye within brain tissue (or any poroelastic medium for that matter) as a result of standing waves is the only observation of such behavior reported in the literature that we are aware of. At present, the exact mechanisms responsible for these bands of dye forming within the rat brain are still unknown. However, the trapping of micro- and nanoscale particles at the nodes or antinodes of standing waves in fluids²⁶⁻²⁹ and the similar trapping of one immiscible liquid within another³⁰ have been demonstrated and are due to acoustic radiation force. The combination of these findings suggests the possibility that acoustic radiation force may be acting directly on the dye as opposed to (or perhaps together with) increasing the permeability of the brain extracellular matrix. Regardless of mechanism, Lewis et al. suggested that ultrasound may be used to control the spatial distribution of infused molecules into the brain tissue post-infusion.

Ultrasound can also be focused to specific targets such as tumors or other diseased tissues to maximize local effects while minimizing unwanted effects elsewhere. For example, O'Neill et al. (2009) used pulsed high intensity focused ultrasound (HIFU) to increase the distribution of systemically-delivered nanoparticles in the calf muscle of mice³¹. By using a

control group of mice that were subjected to the same thermal dose, the authors were able to rule out hyperthermia as a major contributor for the increase in nanoparticle distribution. While cavitation may have been a possible mechanism, their data seemed to suggest that acoustic radiation force-induced displacements played a key role in affecting the structural integrity of the calf muscle, leading to increased uptake of the nanoparticles.

While focusing ultrasound in muscle tissue can easily be done using conventional methods like multi-element phased arrays, the brain presents more challenges due to the presence of the skull, which is uneven in thickness and comprises both cortical and trabecular bone, making it a highly dissipative material. Thankfully, this problem can be addressed using the principles of time-reversal acoustics (TRA)³²⁻³⁴.

Lewis et al. (2010) developed a TRA-CED system that uses TRA to focus ultrasound at the tip of the infusion needle²⁴. This was done by adding a hydrophone to the tip of the infusion needle to serve as a reference point at the site of infusion. Once the infusion needle is in place, the TRA-CED system can be set up for focusing ultrasound. Each element of a multi-element reverberator positioned outside the skull would emit ultrasound waves in sequence. Each ultrasound wave would get distorted as it enters the skull, and once within, would reflect around the cranial cavity repeatedly until it is completely dissipated (Figure 1.1A). While this is occurring, the hydrophone would simultaneously be recording the times at which it detects the ultrasound wave ever since the wave was emitted from the reverberator, thereby creating a time profile for each element (Figure 1.1B). Once these time profiles are reversed, the TRA-CED system is then ready to focus ultrasound (Figure 1.1C). When the system is now activated, each element in the

reverberator would send out a series of waves based on the reversed time profiles. In doing so, this series of waves will eventually converge and constructively interfere, creating a pulse of high acoustic pressure at the site of infusion (Figure 1.1D). The components of the TRA-CED system are summarized in Figure 1.2.

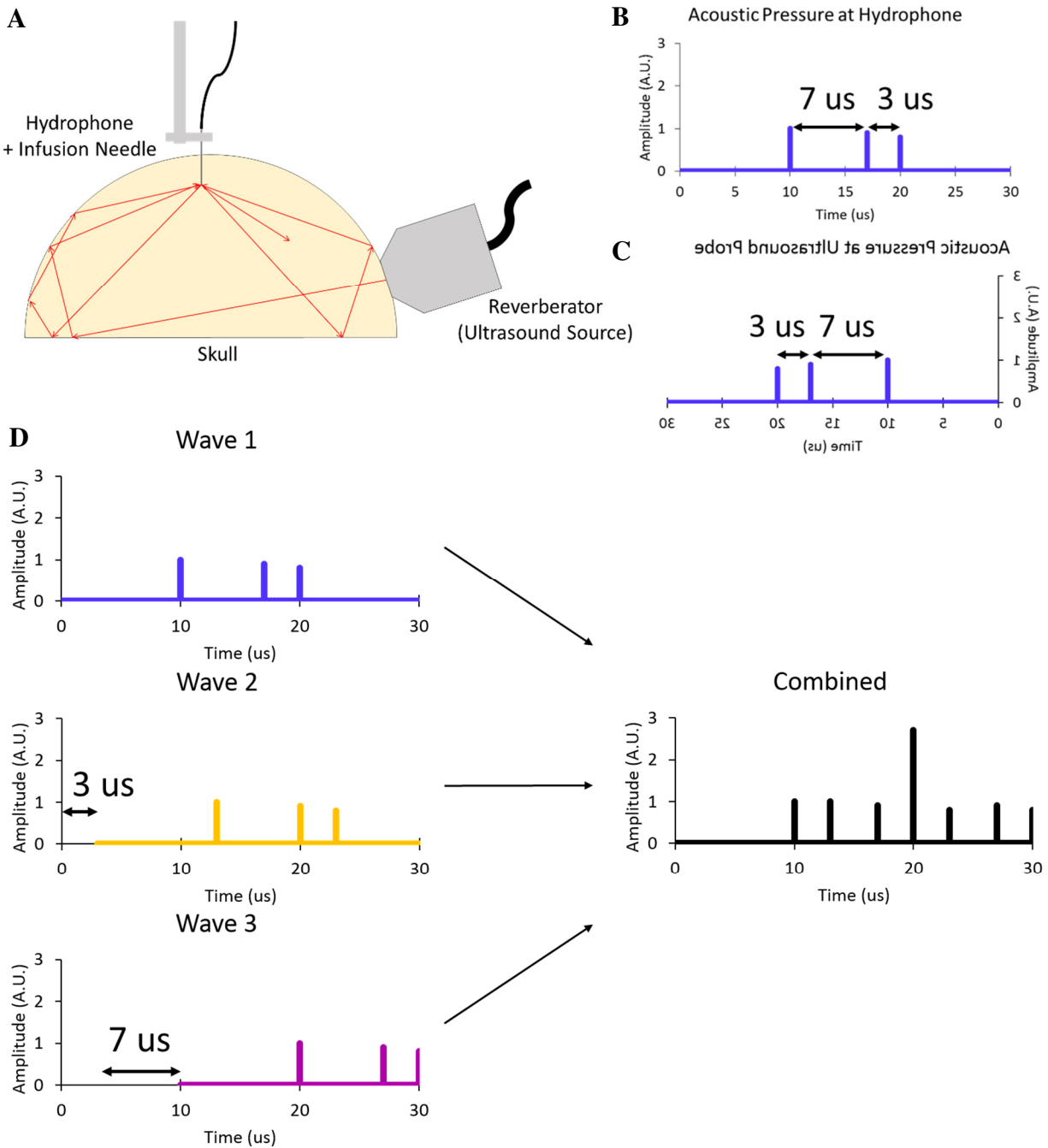


Figure 1.1: A) A hydrophone at the tip of the infusion needle records the acoustic pressure due to the ultrasound wave emitted by the reverberator. B) A simplified example of the acoustic pressure time profile as recorded by the hydrophone. A peak in acoustic pressure occurs whenever the hydrophone detects the ultrasound wave. The second and third peaks occur 7 and

10 μs after the initial peak. C) The time-reversed signal. In this configuration, the second and third peaks occur 3 and 10 μs after the initial peak. D) The original ultrasound wave is repeatedly emitted at intervals corresponding to the time-reversed signal, i.e., the second and third ultrasound waves are emitted 3 and 10 μs after the first ultrasound wave is emitted. These ultrasound waves interfere constructively at the 20- μs time point, resulting in a large increase in acoustic pressure at the tip of the infusion needle/hydrophone.

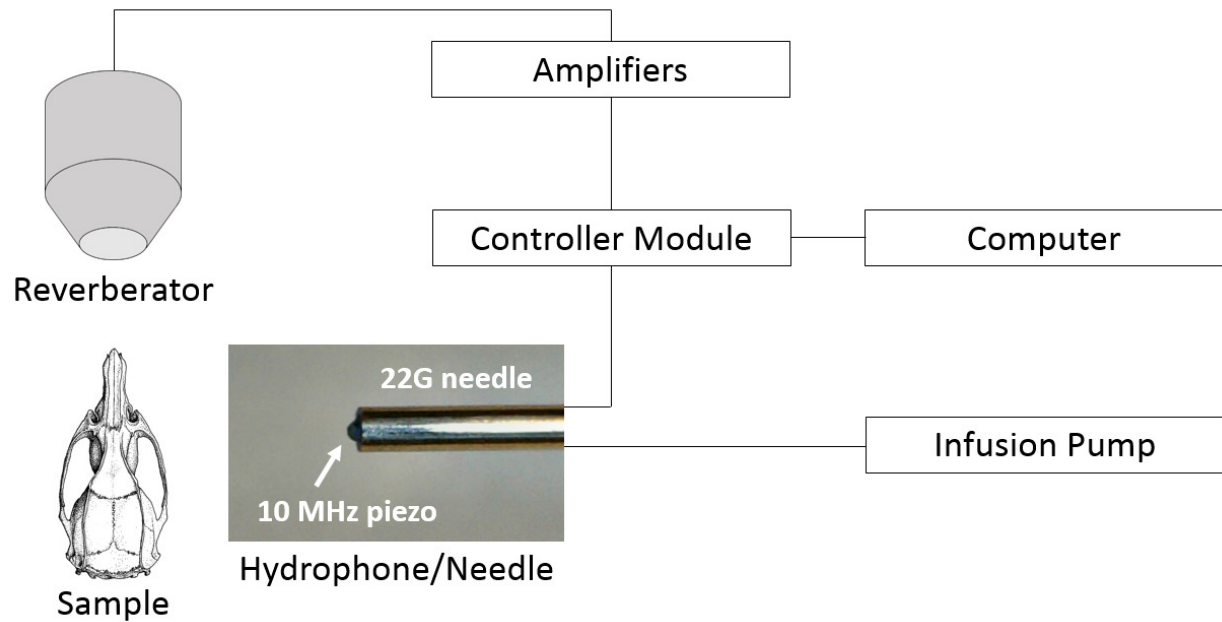


Figure 1.2: The components of the TRA-CED system. The infusion needle is connected to the infusion pump while the hydrophone at the tip of the infusion needle is connected to the controller module. Acoustic pressures detected by the hydrophone are converted into electrical signals that are sent to the computer via the controller module. The computer time-reverses and processes the input signals to generate an optimized output signal that would focus ultrasound waves at the hydrophone. This signal is sent via the controller module to the amplifiers for amplification, and then to the reverberator to generate the ultrasound waves.

Olbricht et al. (2013) then used this TRA-CED system to focus ultrasound at the tip of an infusion needle during convection-enhanced delivery of both Evans blue (960 Da) and Evans blue-labeled bovine serum albumin (~66 kDa) into rodent brain tissue. Their results showed that TRA-focused ultrasound increased the distribution volumes of the two tracers by up to a factor of two as compared to convection-enhanced delivery alone²³. The addition of lipid-encapsulated microbubbles to either of those dyes further increased their distribution volumes, even in the absence of ultrasound. While the exact reason for the increase in distribution volumes due to TRA-focused ultrasound is unknown, the authors mention that acoustic cavitation and the resulting microstreaming are often the underlying mechanisms for ultrasound-enhanced mass transfer^{23,35}. Acoustic cavitation of lipid-encapsulated microbubbles in the bloodstream has been shown to disrupt the blood-brain barrier³⁶, but it is unclear how such microbubbles behave when infused directly into brain tissue. This is because these microbubble diameters are on the order of micrometers^{37,38}, which is at least an order of magnitude larger than the average pore size of the extracellular space in the brain^{39,40}.

An alternative to using TRA to focus ultrasound at the site of a co-infusion of dye and microbubbles is the use of systemically-administered microbubbles to amplify the effects of focused ultrasound prior to infusion. Recently, Wang et al. (2017) used a single-element focused ultrasound transducer to focus ultrasound in the caudate-putamen of mice prior to the direct infusion of either gadolinium-labeled albumin (~74 kDa) or an adeno-associated virus (~4 MDa) carrying the gene for green fluorescent protein at the same site⁴¹. To enhance the effects of the ultrasound, the authors administered microbubbles systemically into the mice via tail-vein injection just prior to sonication. The authors found a significant increase in the distribution

volume of gadolinium-labeled albumin in sonicated brains when MRI scans were performed 120 mins, but not 30 mins, post-infusion. The authors also found increased distribution of AAV transduced cells in sonicated brains. Because the mouse brains were sonicated prior to the infusion of the macromolecules, these results suggest that ultrasound can prime brain tissue in a manner that, given sufficient time, leads to increased distribution of infused macromolecules. Potential mechanisms include increased intercellular permeability within the sonicated region as a result of shear forces generated by acoustic radiation force, or cavitation-induced increases in vascular permeability that allows the macromolecules to exit the extracellular space and reenter further from the site of infusion⁴¹.

In both the Olbricht et al. and the Wang et al. studies, histological analyses showed that aside from tissue damage resulting from CED, there was little to no additional tissue damage from exposure to ultrasound with their experimental settings. For the Olbricht et al. study, infusions that included microbubbles appeared to show more hemorrhages and edema around the needle track as compared to infusions with dye only, independent of whether ultrasound was applied²³. For the Wang et al. study, no additional tissue damage from ultrasound was observed in mice that were euthanized 3 hours or 2 weeks post-infusion as compared to non-sonicated mice⁴¹. These results suggest that focused ultrasound may be used safely to enhance the effects of CED within the brain.

The aim of this dissertation is to further investigate the effects of ultrasound on convection-enhanced delivery.

In chapter 2, we used MRI to measure the distribution volumes and concentration profiles of a small tracer administered via CED into very low percentage weight per volume agarose gels, which are commonly used as brain phantoms to assess the efficacy of CED. The V_d/V_i ratios reported in the literature as well as from our MRI scans are larger than would be expected based on the porosity of these gels. Our results from models of diffusion and convection suggest that this may be partially explained by the high diffusivity of this MRI tracer in very low percentage weight per volume agarose gels, making porosity a poor parameter for estimating the distribution volumes in these gels.

In chapter 3, we used TRA-focused ultrasound to sonicate locations at or adjacent to the site of CED infusion in agarose gels and in vivo in rodent brains to determine whether it can be used to expand or shape the distribution volumes of the infused tracers. Even when the tracers were co-infused with phospholipid-encapsulated microbubbles, TRA-focused ultrasound did not appear to have a significant effect on the size or shape of the distribution volumes of the infused tracers.

In chapter 4, we used TRA-focused 0.5 MHz ultrasound to sonicate sites of CED infusion in vivo in rodent brains to determine whether doing so increases the distribution volume of a macromolecular tracer mixed with either 20- or 40-nm polystyrene particles. Our results show that TRA-focused ultrasound significantly increased the distribution volume of the macromolecular tracer when it was mixed with 20-nm, but not 40-nm, particles. Results from fitting concentration line profiles to a diffusion model suggest that the increase is due to enhancement of convection rather than diffusion.

In chapter 5, we histologically identified axon bundles within the rodent caudate putamen that are responsible for the uneven distribution of tracers observed in CED studies involving fluorescent imaging. We found that the concentration of Evans blue–labeled bovine serum albumin within these axon bundles is approximately 67% of the concentration in the surrounding grey matter. This suggests the importance of accounting for the non-uniform distribution of chemotherapeutic drugs administered via CED to ensure that therapeutic concentrations are achieved and maintained during treatment.

In chapter 6, we evaluated the effects of radially-emitted ultrasound on the distribution of Evans blue dye administered via CED in 0.2% wt/vol agarose gels created with milk and water in a 1:1 ratio. We observed that ultrasound does not appear to significantly increase the distribution volume of Evans blue as compared to no ultrasound, and that heat generated by the ultrasound transducer may be a confounding factor.

In chapter 7, we progress from research in biomedical engineering to research in biomedical engineering education. In this chapter, we explored how students in an Introduction to Biomedical Engineering course adapted to a mid-semester Biotransport module that used the Flipped Classroom model. Our survey results indicated that the majority of respondents did not find it difficult to adapt to the mid-semester Flipped Classroom module, and we identified ways to smoothen the transition for students who have difficulty adapting.

CHAPTER 2

EVALUATING THE EFFECTS OF CONVECTION AND DIFFUSION ON A GADOLINIUM TRACER IN CONVECTION-ENHANCED DELIVERY

2.1 Introduction

Glioblastoma multiforme is a malignant brain tumor with poor survival outcomes for patients despite aggressive treatments such as surgical debulking, radiation, and chemotherapy^{1,2}. One reason is the presence of the blood-brain barrier, which limits most systemically-administered chemotherapeutic drugs from entering the affected brain regions at sufficient volumes and concentrations^{5,42}. Convection-enhanced delivery (CED) is a promising method for delivering drugs to the brain^{10,11}. In CED, fluid containing a drug is infused through a needle directly into the brain interstitium near targeted tissue sites. Near the needle tip, transport of infused fluid in CED is dominated by convection, i.e., bulk flow of the fluid due to a pressure gradient generated by the infusion pump. However, because the fluid velocity decreases with increasing distance from the tip, diffusion, i.e., movement of fluid molecules down a concentration gradient, also becomes important at sufficiently large distances from the needle tip.

To evaluate the efficacy of CED, very low percentage (~0.2–0.6) weight-per-volume (wt/vol) agarose gels are commonly used as brain-mimicking phantoms^{43–50}. The key parameter investigators use to estimate the extent of infusate coverage is the ratio V_d/V_i , where V_d is the

distribution volume of a tracer (the volume of tissue or gel covered by the tracer) and V_i is the volume of the tracer infused. Using magnetic resonance imaging (MRI), Chen et al. found V_d/V_i values of 10 for 0.6% wt/vol agarose gel and 7.1 for brain tissue⁴⁸. This is surprising, because gels with such low agarose content should have extremely low volume fractions of agarose fibers (<0.01)⁵¹ and thus have porosities near one⁵², whereas brain tissue has a porosity around 0.15–0.20⁵³. The porosity is the ratio of pore volume to total volume⁵⁴ and represents the volume fraction of space within a given material through which the infused fluid can flow. As such, if transport of the fluid were governed completely by convection, then the ratio V_d/V_i should be close to the inverse of the porosity. Thus, the expected values of V_d/V_i are 1.0 for agarose gels and 5.0–6.7 for brain tissue.

Delineating mechanisms that determine the value of V_d/V_i in agarose gels is challenging. Numerous studies involving the infusion of tracers in gels and in vivo in brains via CED have been conducted^{10,23,55–57}, but in many of those studies, V_d was determined by imaging slices of tissue or gel after the experiment and then interpolating the dyed areas, which is tedious and subject to error. With MRI, not only can the V_d be determined at multiple time points throughout the experiment while the gels or brains are still intact, it also enables the measurement of the full concentration profile of the tracer from the needle tip to the farthest extent of tracer penetration⁵⁸. This provides additional information to assess the roles of convection and diffusion as well as other possible mechanisms that influence tracer transport in agarose gels.

The objective of this study is to determine the value of V_d/V_i as well as the tracer concentration profiles of CED infusions in low percentage wt/vol agarose gels over multiple time points. This

may allow us to better understand why the value of V_d/V_i in such infusions are much higher than expected based on porosity. This would in turn allow us to better interpret the results of CED experiments in agarose gels when they are used to model CED within the brain.

2.2 Materials and Methods

2.2.1 Agarose Gel Phantom

To form the gel sample, 170 mL of 0.2% wt/vol agarose in distilled water was heated and allowed to come to a rolling boil. The solution of agarose was then allowed to cool to 50°C before it was poured into a 240-mL plastic container. Two solutions of gadolinium (Magnevist, Bayer Healthcare, MW = 938 Da) of differing concentrations (2.5 mM and 1.25 mM) were made and placed into small balloons. These gadolinium-filled balloons served as reference gadolinium concentrations in magnetic resonance imaging scans. The small balloons were then placed into the plastic container, and the agarose was allowed to solidify around them. We used a total of 4 gel phantoms in this study.

2.2.2 Gadolinium Infusion and MRI Scans

The gadolinium tracer was infused into the gel through an MRI-compatible polyether-etherketone (PEEK) needle (PlasticsOne, Roanoke, VA) with an internal diameter of 0.19 mm and an external diameter of 0.36 mm. The dimensions of the needle resemble those of a 28G needle, which is typically used in CED treatments. Prior to infusion, a T2*-weighted scan (TR =

57.0, Number of TEs per scan = 11, Flip Angle = 20) lasting approximately 4.5 min was performed. Then, the 2.5-mM gadolinium was infused into the agarose gel at a rate of 1 $\mu\text{L}/\text{min}$. Once the infusion was started, a series of eight scans was performed consecutively. After the final scan, the infusion was stopped, and an additional four scans were obtained with the needle left in place. All scans were performed in a 3 Tesla GE750 MRI Scanner and had a voxel size of $0.6*0.6*1 \text{ mm}^3$.

The T2*-weighted scans were then post-processed using Quantitative Susceptibility Mapping and analyzed using ITK-SNAP⁵⁹. The voxel exhibiting the maximum susceptibility (in parts per billion) in each scan was located. Using this voxel as the center point, the susceptibilities of the surrounding voxels that lie along the vertical axis and two horizontal axes—left-right and anterior-posterior—at various time points before, during, and after the infusion were measured. In addition, the value of V_d for the infusion was determined by including only 6-connected neighboring voxels, i.e., voxels that share a face, beginning with the center voxel. The value of V_i was determined by multiplying the infusion rate by the infusion duration.

2.2.3 Post-processing MRI scans

To convert the measured susceptibilities into absolute gadolinium concentrations, a linear relationship was established between susceptibility and concentration using the measured susceptibilities for the three known concentrations in each experiment: the 2.5-mM and 1.25-mM gadolinium concentrations in the two balloons and the 0-mM concentration in plain agarose gel. A linear relationship was constructed for each scan. Then, the susceptibility was converted into

gadolinium concentration using the relationship for the specific scan. Gadolinium concentrations were then plotted with respect to distance from the central voxel, i.e. the voxel with the highest concentration of gadolinium in the scan. Due to intrinsic inaccuracy at low susceptibility values, a threshold of 2.5% of the 2.5-mM gadolinium infusate, i.e., 0.0625 mM, was applied to determine the volumes of distribution.

An example of the agarose gel phantom and a corresponding MRI image is shown in Figure 2.1.

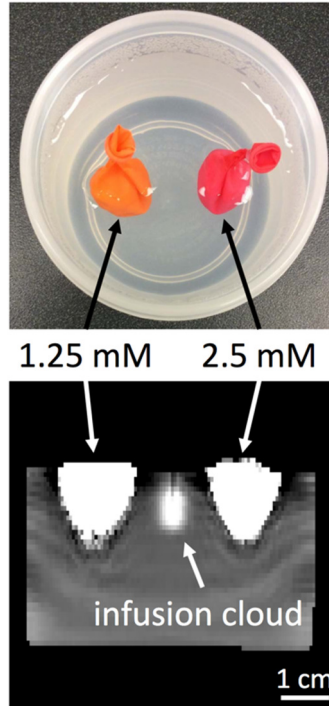


Figure 2.1: Above: Each phantom was made with 170 mL of 0.2% wt/vol agarose gel and was embedded with two balloons containing different concentrations (1.25 mM and 2.5 mM) of gadolinium to serve as reference concentrations. A total of 4 gel phantoms were used. Bottom: The corresponding MR image of the phantom at the end of the experiment is shown. The distribution volume of gadolinium resulting from the infusion of 2.5-mM gadolinium into the center of the gel can be seen between the two gadolinium-filled balloons.

2.2.4 Modeling the diffusion and convection of gadolinium from a continuous point source in water

To model pure diffusion of gadolinium from a continuous point source in water, we used the following equation⁶⁰:

$$c = \frac{q}{4\pi Dr} \operatorname{erfc}\left(\frac{r}{2\sqrt{Dt}}\right)$$

Equation 2.1: Concentration of gadolinium based on diffusion from a continuous point source, where c is the concentration of gadolinium, q is the molar flowrate, D is the diffusivity of gadolinium in water, r is the radius from the point source, and t is the duration of infusion.

Because the agarose gels used in this experiment have very low percentage wt/vol of agarose, i.e., 0.2%, we estimate the parameters for the model using those for water at 25 °C. The parameters used in this diffusion model are summarized in Table 2.1.

To model the gadolinium distribution volume due only to the convection of gadolinium from a continuous point source in water, we used the following equation:

$$V_d = \frac{V_i}{\phi}$$

Equation 2.2: Volume of distribution of gadolinium based on convection from a continuous point source, where V_d is the volume of tracer distribution, V_i is the volume of infused tracer, and ϕ is the porosity of the agarose gel medium. We assumed a flowrate of 1 $\mu\text{L}/\text{min}$, a spherical distribution volume of constant concentration, and a porosity of one in the agarose gel medium.

Table 2.1: Summary of the values assigned to the parameters in the model of diffusion from a continuous point source.

Parameter	Value
c (mM)	2.5
Q ($\mu\text{L}/\text{min}$)	1
q (mmol/s) = $c*Q$	$4.17 * 10^{-8}$
D @ 25 °C (um^2/s)	400 (estimate ⁶¹)
t (min)	1/60 (=1s), 10, 20, 30 40

2.3 Results

2.3.1 Gadolinium concentration profiles from MRI scans

We determined the gadolinium concentration profiles of the infusions along the vertical axis and two horizontal axes—left-right and anterior-posterior—at various time points before, during, and after the infusion. The concentration profiles after 30 minutes of infusion for the vertical, left-right, and anterior-posterior axes are shown in Figure 2.2, Figure 2.3, and Figure 2.4, respectively.

For a perfect spherical infusion, we would expect the concentration profile to be symmetrical along all three axes. However, the concentration profiles obtained do not appear symmetrical along these axes.

From Figure 2.2, if we assume that the voxel with the highest intensity corresponds to the tip of the infusion needle, and that the needle is parallel to the vertical axis, this implies that the needle lies along the vertical axis. This may account for the bias in the concentration profile towards the positive region of the vertical axis. Since the needle has a uniform diameter, the increase in susceptibility due to the gadolinium within the needle should be constant along the length of the needle. There is also the possibility of a small amount of backflow of the gadolinium tracer up the needle track that cannot be ruled out.

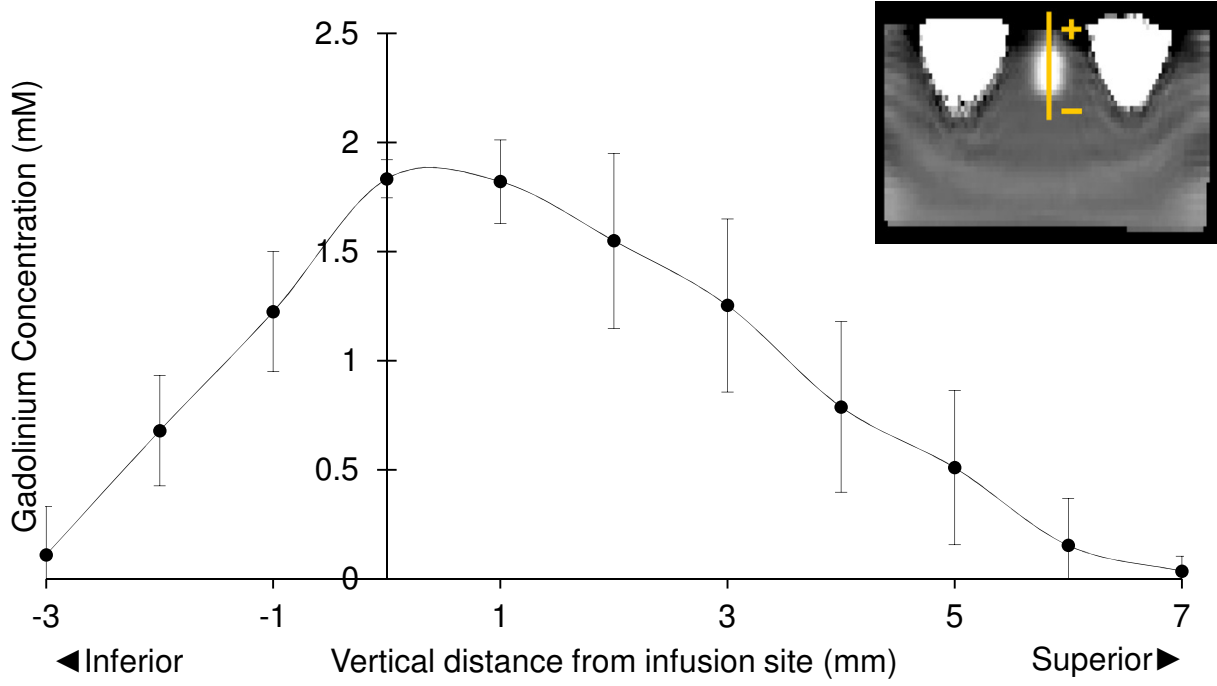


Figure 2.2: The mean gadolinium concentrations along the vertical axis of the infusion cloud after 30 minutes of infusion. Zero corresponds to the needle tip and infusion site, while the positive horizontal axis corresponds to the needle. Error bars represent \pm one standard deviation. (n = 4) There is a slight bias in the concentration profile towards the positive region of the vertical axis.

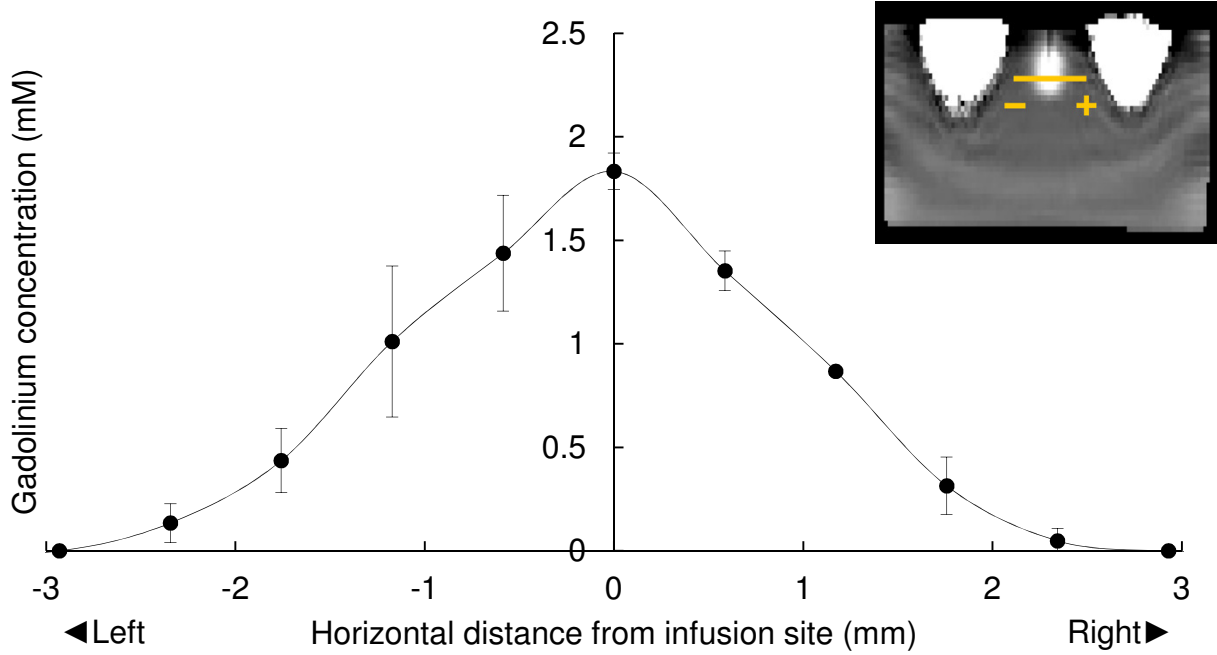


Figure 2.3: The mean gadolinium concentrations along the left-right horizontal axis of the infusion cloud after 30 minutes of infusion. Zero corresponds to the needle tip and infusion site. Error bars represent \pm one standard deviation. (n = 4)

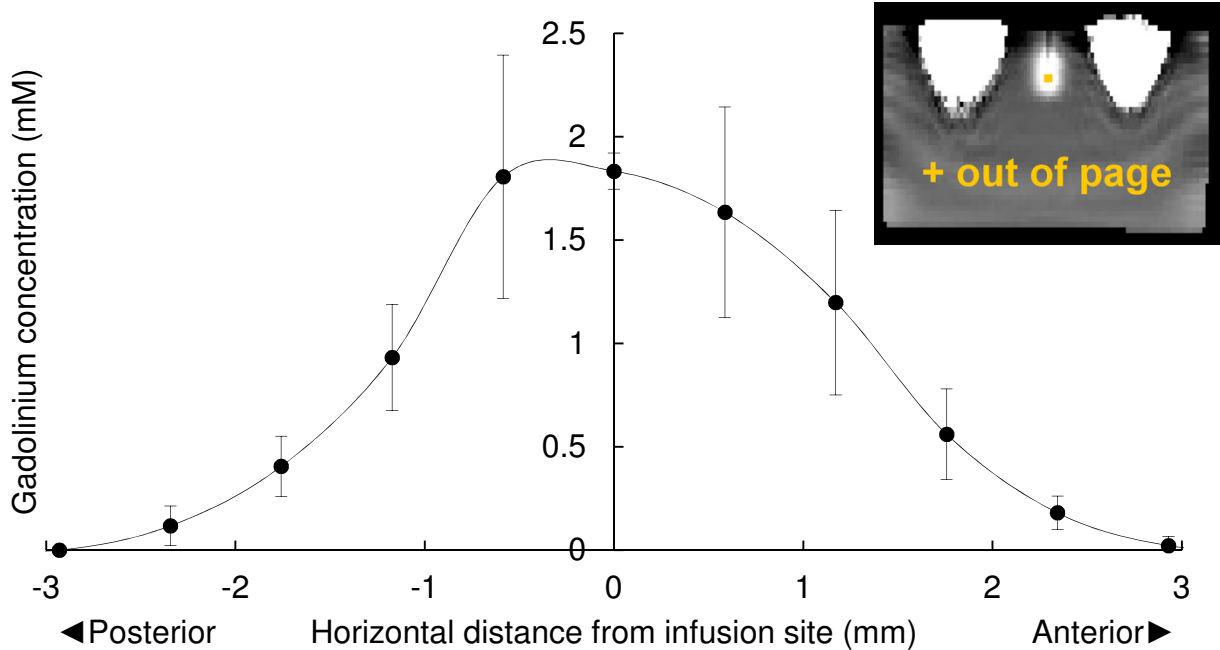


Figure 2.4: The mean gadolinium concentrations along the anterior-posterior horizontal axis of the infusion cloud after 30 minutes of infusion. Zero corresponds to the needle tip and infusion site. Error bars represent \pm one standard deviation. ($n = 4$) There is a slight asymmetry in the concentration profile with minimal initial decrease followed by a steeper drop in concentration when moving posteriorly away from the infusion site.

The gadolinium concentration at each voxel directly below the needle tip, namely, the negative region of the vertical axis, decreased with increasing distance from the needle tip. This is expected as the convective force pushing the gadolinium through the gel is diminished.

Based on the gadolinium concentration profiles in Figure 2.3 and Figure 2.4, the concentration decreased with increasing horizontal distance from the infusion site. The concentration profiles are also not entirely symmetrical along both horizontal axes, which has been previously observed in the literature⁵⁸. One possibility for this asymmetry is that any small amount of backflow that occurred may have traveled preferentially along one side of the needle than the other. Another possibility is that the pressure from the infusion needle may have resulted in a small crack in the gel in which the infused gadolinium could pool.

2.3.2 Gadolinium distribution volume and V_d/V_i from MRI scans

The gadolinium distribution volume was determined using a threshold of 0.0625 mM. The V_d increased linearly (gradient = 4.14) with respect to the infusion duration during the 40-minute infusion, which is expected as the infusion rate was kept constant (Figure 2.5). After the infusion was stopped, the V_d continued to increase linearly with respect to time, although at a different rate (gradient = 1.92).

During the infusion, the V_d/V_i ratio with respect to the duration of the infusion decreased significantly between the first two time points, but then quickly stabilized around 4.4 (Figure 2.6).

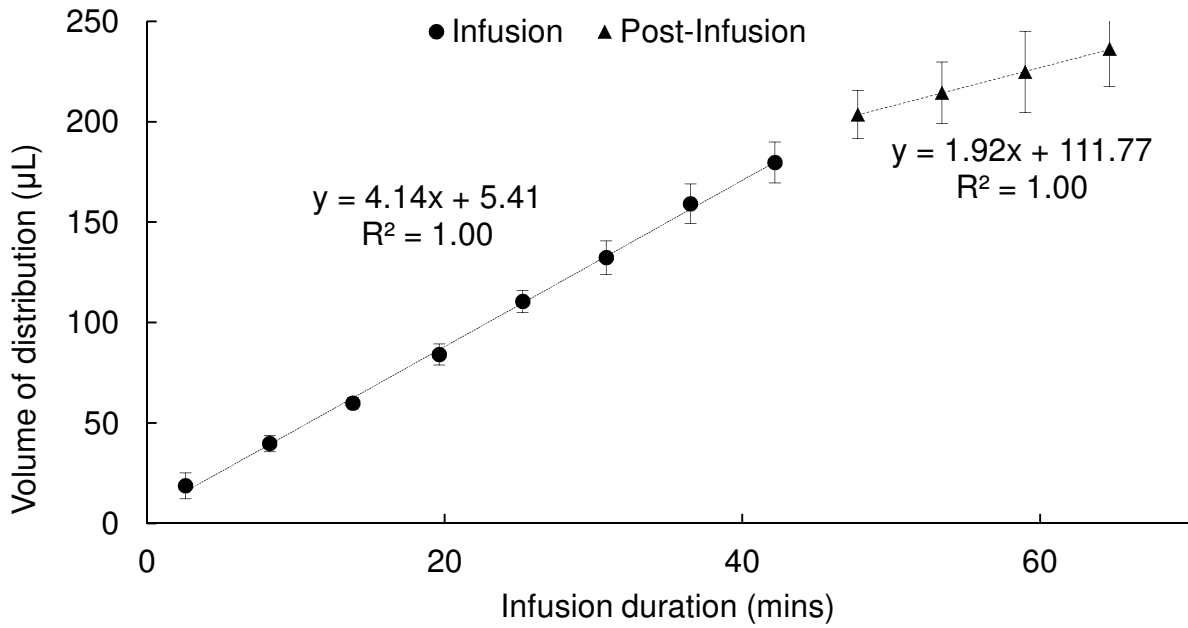


Figure 2.5: Mean distribution volumes during and after the infusion using a threshold of 0.0625 mM. The rate at which V_d increased during the infusion was twice the rate post-infusion. Error bars represent \pm one standard deviation. (n = 4)

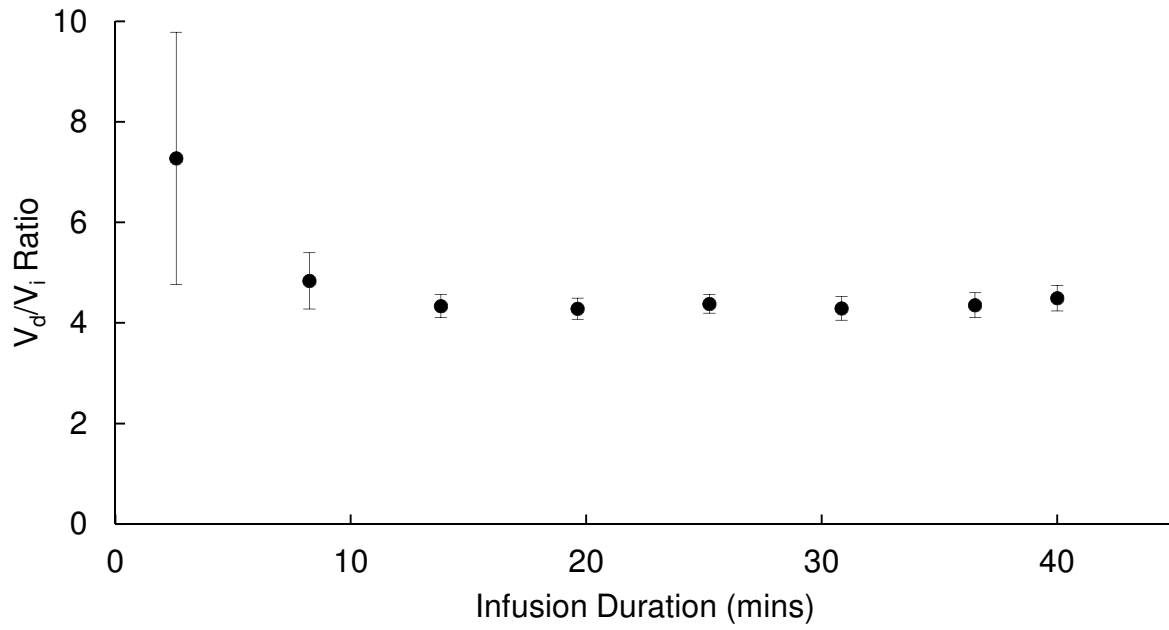


Figure 2.6: Excluding the first time point, the V_d/V_i was ~ 4.4 throughout the duration of the infusion using a threshold of 0.0625 mM. Error bars represent \pm one standard deviation. (n = 4)

2.3.3 Gadolinium concentration profiles derived from pure diffusion model

The expected gadolinium molar concentration profiles derived from the model of diffusion from a continuous point source at multiple time points is shown in Figure 2.7. Using the estimated diffusion coefficient⁶¹ of $400 \text{ } \mu\text{m}^2/\text{s}$ for gadolinium in water at $25 \text{ } ^\circ\text{C}$, the concentration close to the site of infusion is several orders of magnitude larger than the concentration of the infusate itself (Figure 2.7A). This buildup suggests that most of the gadolinium is unable to diffuse away fast enough from the point source. Focusing on the concentration profiles between the threshold of 0.0625 mM and the infusate concentration of 2.5 mM , it is apparent that although the farthest distance the gadolinium reached increased with longer infusion durations, this distance is increasing at a decreasing rate (Figure 2.7B).

The distribution volumes from the MRI data, the pure diffusion model, and the pure convection model were compared across multiple time points during the infusion (Figure 2.8A). With the threshold set at 0.0625 mM , i.e., 2.5% of infusate gadolinium concentration, the distribution volumes based on the MRI data were larger than those based on the pure diffusion model and the pure convection model across all time points. Unlike the distribution volumes from the pure convection model, which all have a constant concentration of 2.5 mM , the distribution volumes from the MRI data and the pure diffusion model are not of constant concentration (e.g., Figure 2.3 and Figure 2.7), making them highly dependent on the threshold used. For example, using a threshold of 0.5 mM , i.e., 20% of infusate gadolinium concentration, the distribution volumes

based on the pure diffusion model are now slightly smaller than those based on the pure convection model.

2.3.4 Gadolinium distribution volumes and radii derived from pure diffusion model

The mean farthest distance the gadolinium spread from the infusion site along the horizontal axes from the MRI data as well as the radii of the spherical distribution volumes based on the pure diffusion model and the pure convection model were compared across multiple time points during the infusion (Figure 2.8B). The mean farthest distance the gadolinium spread from the infusion site along the vertical axis from the MRI data was not included as the concentration profile was skewed towards the superior axis, reflecting the teardrop shape of the distribution volume. With the threshold set at 0.0625 mM, the radii based on the pure diffusion model was larger than those based on the pure convection model. The mean farthest distance the gadolinium spread from the infusion site along the horizontal axes from the MRI data tended to fall in between the radii of the two models. Like with determining the distribution volumes, the mean farthest distance the gadolinium spread from the infusion site from the MRI data and the radii based on the pure diffusion model are highly dependent on the threshold used. Using a threshold of 0.5 mM again, for example, the radii based on the pure diffusion model are now slightly smaller than those based on the pure convection model.

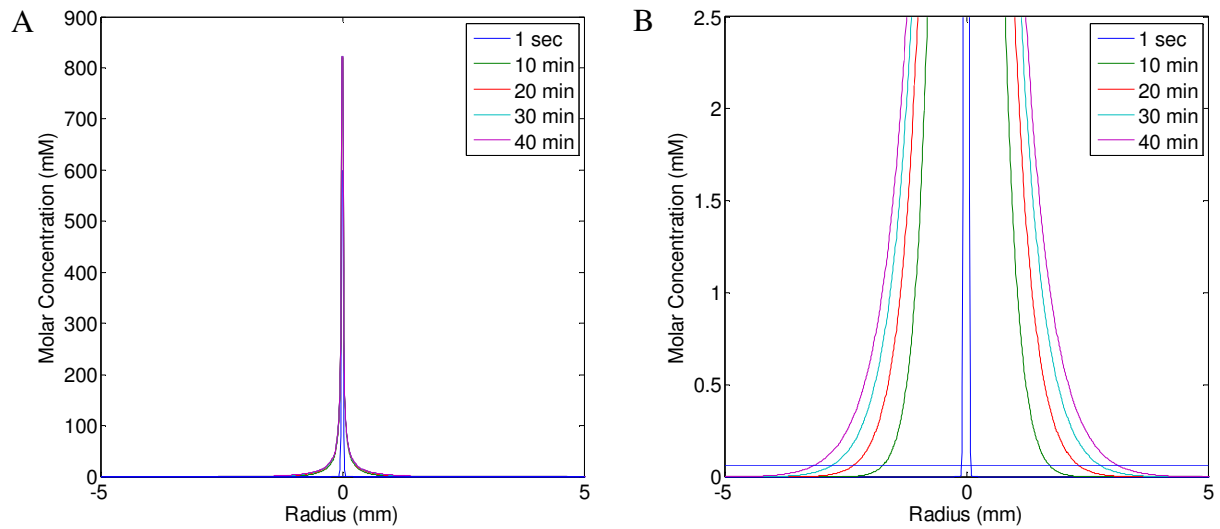


Figure 2.7: A) The expected gadolinium molar concentration profiles after 1 s and 10, 20, 30, and 40 min of infusion of 2.5-mM gadolinium at a flowrate of 1 $\mu\text{L}/\text{min}$ in water. Using an estimated $D = 400 \text{ um}^2/\text{s}$, the concentration close to the site of infusion is several orders of magnitude larger than the concentration of the infusate. B) The same concentration profiles zoomed in to the range of 2.5 mM and below. The horizontal line represents the threshold of 0.0625 mM used to determine the volumes of distribution. Although the farthest distance the gadolinium reached increased with longer infusion durations, the increases in distance decreased with time.

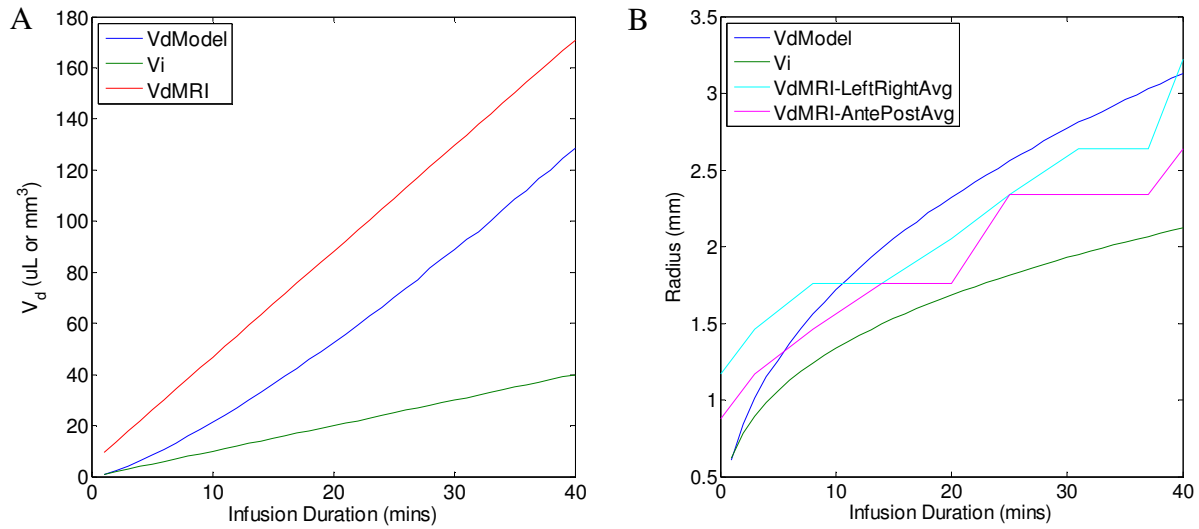


Figure 2.8: A) Comparison of the distribution volumes with respect to infusion duration based on the linear regression equation obtained from the MRI data ($V_d\text{MRI}$) and the expected distribution volumes based on only diffusion from a continuous point source ($V_d\text{Model}$) and on only convection (V_i). With a threshold of 0.0625 mM, the distribution volumes for $V_d\text{MRI}$ are larger than those from $V_d\text{Model}$ and V_i . B) Comparison of the radii of the spherical distribution volumes with respect to infusion duration based on only diffusion from a continuous point source ($V_d\text{Model}$) and on only convection (V_i). The mean farthest distance the gadolinium spread from the infusion site from the MRI data along the left-right axis ($V_d\text{MRI-LeftRightAvg}$) and anterior-posterior axis ($V_d\text{MRI-AntePostAvg}$) are plotted as well. The lower mean farthest distance the gadolinium spread along these two axes is likely due to the teardrop shape of the distribution volumes based on the MRI scans, since the mean farthest distance the gadolinium traveled along the superior axis is about double that along the inferior axis.

2.4 Discussion

Convection-enhanced delivery is a promising drug delivery modality that bypasses the blood-brain barrier to administer chemotherapeutic agents to the brain for the treatment of devastating diseases such as glioblastoma multiforme. Very low percentage wt/vol agarose gels are often used to evaluate the efficacy of CED, but the V_d/V_i ratios obtained are much higher than expected from media with porosities near one.

When we modeled the distribution volume based solely on convection, we assumed that the distribution volume was spherical and of constant concentration, and that the porosity of the medium was one. As such, the V_d/V_i ratio predicted from this model is independent of the concentration threshold used. This, however, is not the case for the distribution volumes based on the MRI data or the diffusion model, as the concentration of gadolinium decreases radially away from the site of infusion. As such, the V_d/V_i ratio based on the MRI data or the diffusion model can be approximately one if the threshold concentration is changed. For example, raising the threshold concentration to 0.5 mM would result in a V_d/V_i ratio of approximately one based on the diffusion model. For our study, we selected a threshold of 0.0625 mM, i.e., 2.5% of the 2.5-mM gadolinium infusate, due to intrinsic inaccuracy at low susceptibility values for the MRI scans, and used the same threshold for our diffusion model.

When we used this threshold of 0.0625 mM on our MRI data, we got a mean V_d/V_i ratio of 4.4 for our CED infusions of 2.5-mM gadolinium in 0.2% wt/vol agarose gels. This V_d/V_i ratio is much more than the unity that would be expected based on the volume fraction of agarose fibers,

thus appearing to validate the results of Chen et al.⁴⁸ However, this result must be carefully interpreted. Chen et al. hypothesized that the large V_d/V_i ratio they obtained may be due to the agarose polysaccharides having a significant volume of hydration that is inaccessible to low molecular weight hydrophilic tracers⁴⁸. After all, Arnott et al. did suggest that agarose gels comprise a network of highly aggregated bundles of double helix chains, with relatively large inter-bundle voids⁶². However, the equation used to calculate the volume fraction of agarose fibers based on agarose concentration does not take this volume of hydration that is inaccessible to macromolecules into account⁵¹. Furthermore, a V_d/V_i ratio of 4.4 suggests a porosity of 0.23 and thus a volume fraction of agarose fibers of 0.77, both of which are highly unlikely for 0.2% wt/vol agarose gel. As such, the larger than expected V_d/V_i ratio cannot be explained solely by a slight decrease in porosity resulting from inaccessible volumes of hydration.

While the distribution volumes based on the MRI data were teardrop-shaped rather than spherical, it was still interesting to observe that using the concentration threshold of 0.0625 mM, the pure diffusion model predicted a radial spread that was generally larger than the mean spread along both the horizontal axes based on the MRI data as well as the radial spread predicted by the pure convection model. This result suggests that the diffusivity of gadolinium in water or low percentage wt/vol agarose is large enough for the MRI tracer to spread to distances seen in the MRI scans based on diffusion alone. This is clearly very different for a medium like brain tissue, where the geometry of the extracellular space and the presence of dead space microdomains, molecular obstructions, binding sites, and fixed negative charges complicate the diffusive pathway of the tracer⁵³. The difference in diffusivity of the tracer in low percentage wt/vol agarose gels and in brain tissue may help explain why the distribution volumes in agarose gels

are larger than those in brain tissue despite these gels having a porosity almost five times that of brain tissue.

It remains difficult to distinguish between the diffusive and convective mechanisms for CED infusions using this protocol. The constant V_d/V_i ratio observed during the infusion of 2.5-mM gadolinium into 0.2% wt/vol agarose gel at an infusion rate of 1 $\mu\text{L}/\text{min}$ corresponds well to the study by Chen et al. that also showed the V_d/V_i ratio remaining constant over the course of infusions of gadodiamide into 0.6% wt/vol agarose gel at fixed flowrates⁴⁸. On the other hand, Neeves et al. observed a time-dependent increase in the V_d/V_i ratio for infusions of Evans blue into 0.6% wt/vol agarose at an infusion pressure of 5 kPa that they attributed to the increased surface area of the infusion cloud⁵⁵. This difference may be due to their use of constant-pressure rather than constant-flowrate infusion.

We also observed that the distribution volume of the MRI tracer appeared to increase at a constant rate post-infusion, but longer time points are needed to obtain the full evolution of the infusion cloud.

Regardless, the mean V_d/V_i ratio from our MRI experiment is close to the expected V_d/V_i ratio of 5.0–6.7 for brain tissue, suggesting that 0.2% wt/vol agarose may be appropriate for estimating V_d/V_i ratios in brain tissue when evaluating CED infusions using gadolinium as the MRI tracer and flowrates around 1 $\mu\text{L}/\text{min}$.

2.4.1 Limitations of the MRI protocol using quantitative susceptibility mapping

Quantitative susceptibility mapping underestimated the number of moles of infused gadolinium by ~20% using the current experimental parameters. This may be due to voxels under the detection threshold or insufficient spatial resolution. We repeated a scan using an alternate peer-reviewed and published MRI scanning protocol⁶³ to measure gadolinium concentrations, and this aligned with our results. This underestimation may be a limitation of MRI, as Iyer et al. found that compared to autoradiography, T2-MRI underestimated the distribution volumes of ¹⁴C-sucrose and ¹⁴C-dextran in non-human primates by 50–60%⁶⁴.

2.5 Conclusion

Convection-enhanced delivery is a promising method of brain drug delivery that is often evaluated using very low percentage wt/vol agarose gels. However, the V_d/V_i ratios obtained are much higher than is expected from media with porosities near one, and this cannot be explained solely by a slight decrease in porosity resulting from inaccessible volumes of hydration. The diffusivity of MRI tracers like gadolinium in water or low percentage wt/vol agarose may be large enough for them to spread to distances observed in MRI scans of CED infusions based on diffusion alone. The difference in diffusivity of the tracer in low percentage wt/vol agarose gels and in brain tissue may help explain why the distribution volumes in agarose gels are larger than those in brain tissue despite these gels having a porosity almost five times that of brain tissue.

CHAPTER 3

THE EFFECT OF TIME-REVERSAL ACOUSTICS FOCUSED ULTRASOUND ON THE DISTRIBUTION OF CONVECTION-ENHANCED DELIVERED DYE AND MICROBUBBLES IN AGAROSE GELS AND RAT BRAINS

3.1 Introduction

Despite the wide variety of chemotherapeutic drugs currently available⁶⁵, patients with malignant brain tumors such as glioblastoma multiforme continue to have poor prognosis and survival rates^{1,2}. These brain pathologies remain challenging to treat because of the presence of the blood-brain barrier, which inhibits the transfer of many systemically-delivered drugs from entering the brain^{5,42}. This limits the available chemotherapeutic drug options to small lipophilic ones like BCNU⁶⁵ or temozolomide⁶⁶.

A promising method to deliver a wider array of chemotherapeutic drugs directly to the tumor site is convection-enhanced delivery (CED)^{10,11}. This strategy involves inserting a needle into the tumorous region of the brain and uses the pressure gradient generated by an infusion pump to locally administer the drug. While CED-induced bulk flow in principle allows for greater distribution of the infused drug as compared to diffusion alone, whether this greater distribution is actually achieved in practice is highly variable. A retrospective analysis of the Phase III PRECISE trial by Sampson et al. found insufficient distribution of cintredekin besudotox, a

cytotoxin that specifically targets gliomas, even within the 2-cm penumbra of the tumor site¹³. While the authors suggested that better catheter placement may improve the efficacy of CED, this is difficult to achieve even when guided by MRI scans. One potential solution is to have the ability to control the spatial distribution of the drug after it exits the needle, which would not only mitigate small deviations in catheter placements, but may also enhance the distribution volumes of well-placed catheters by steering the drug towards the intended target.

Recently, ultrasound has been used to further increase the distribution volumes of tracers administered via CED in vivo in brain tissue. The ultrasound may be focused^{23,41} or unfocused^{22,67}, and can be used prior⁴¹ or during the infusion^{22,23,67}. In particular, Olbricht et al. demonstrated that using time-reversal acoustics (TRA) to focus 1 MHz ultrasound waves at the tip of the infusion needle increased the distribution volume of Evans blue and Evans blue–labeled bovine serum albumin delivered by CED in vivo in rodent brains²³. When either tracer was co-infused with lipid-encapsulated microbubbles, the distribution volumes of the tracers increased, even in the absence of ultrasound. When ultrasound was then applied to these co-infusions, the distribution volumes of the tracers approximately doubled. The exact mechanism behind this TRA-focused ultrasound-mediated increase in the distribution volumes of tracers delivered via CED remains unclear, although based on other works involving ultrasound-enhanced drug delivery, possible mechanisms include acoustic radiation force that exerts convective forces on the drug or induces shear stresses within the tissue resulting in intercellular gaps^{22,68}, or acoustic cavitation that disrupts the blood-brain barrier^{41,69}.

Because TRA-focused ultrasound has been shown to increase the distribution volumes of infused tracers when it is focused at the site of infusion, there exists the possibility that focusing it adjacent to the site of infusion could steer the infused drug towards or away from the ultrasound focal region. In addition, creating ultrasound focal regions of complex shapes could potentially enhance the distribution volumes of CED infusions. For example, if TRA-focused ultrasound is found to attract the infused drug towards the ultrasound focal region, conforming the focal region to the shape of the tumor would maximize the amount of infused drug flowing towards the tumor. Conversely, if TRA-focused ultrasound is found to repel the infused drug, creating a focal region that borders the tumor would minimize the amount of drug exiting the tumor.

The objective of this study is to build upon this previous work by using TRA to create ultrasound focal regions of complex shapes, and studying the effect of focusing ultrasound using TRA at regions adjacent to or at the site of infusion when tracers are either co-infused with lipid-encapsulated microbubbles or infused alone.

3.2 Materials and Methods

3.2.1 Development of the TRA-focused ultrasound system and needle hydrophones

Artann Laboratories developed a customized TRA-CED system to focus ultrasound waves into regions of varying shapes and sizes. Two reverberators, one 0.5 MHz and one 1 MHz, were used in this study to determine the effect of frequency on the focal region. A lower frequency would

theoretically minimize heating of tissue while maximizing the mechanical effects of the ultrasound²⁰.

Needle hydrophones that would allow for CED infusions as well as for measuring acoustic pressure and setting the reference points for TRA-focusing were constructed in-house. These needle hydrophones were developed by placing miniature piezoelectric transducers at the tips of 2.5"-long 22G stainless steel tubing (McMaster Carr #5560K59) with a nominal outer diameter of 710 μm . These piezoelectric transducers measure 1000 μm (length) by 125 μm (width) by 200 μm (height), and are cut from larger piezoelectric discs with a central resonance frequency of 10 MHz (Steiner & Martins, Inc. #SMD10T02F412ST) using laser ablation. A pair of 36G enamel-coated motor winding wires (McMaster Carr #7588K27) was soldered to each piezoelectric transducer and then threaded through the steel tubing, exiting through a hole in the tubing about 1" from the end. The wires were then attached to a double-twisted cable and soldered in place. The end of the steel tubing was then attached via a flanged tubing connector (Basi #MD-1510) to microdialysis FEP Teflon tubing (Basi #MF-5164) with an internal diameter of 120 μm .

3.2.2 Preparation of Tracers

0.25% wt/vol Evans blue (EB) dye was prepared by adding reverse-osmosis deionized (RODI) water to 0.25 g of Evans blue (MP Biomedicals #151108) to a total volume of 100 mL. 5% wt/vol Evans blue-labeled bovine serum albumin (EBA) was prepared by adding 1X PBS (Sigma #P3813) to a mixture of 0.25 g of bovine serum albumin (Sigma #B4287-5G) and 0.022g of Evans blue to a total volume of 5 mL. The dyes were then filtered using a syringe filter with a

0.2- μ m nylon membrane (PALL #4433). The 0.25% wt/vol Evans blue dye was stored at room temperature while the 5% wt/vol Evans blue-labeled bovine serum albumin was divided into 100- μ L aliquots and frozen at -20 °C for storage, and thawed and vortexed just prior to use.

3.2.3 Characterization of the Region of Ultrasound Focus in Water and Agarose Gel

All the peak-to-peak acoustic pressure profiles of ultrasound focal regions generated by the TRA-CED system use the coordinate system described in Figure 3.1. These focal regions were generated in rectangular plastic containers filled with reverse-osmosis deionized water or 0.2% wt/vol agarose gel. Ultrasound transmission gel was applied to the reverberator face prior to placing it against the side of the plastic container. The needle hydrophone was then placed in the middle of the plastic container. The TRA-CED system was then used to focus ultrasound at the location corresponding to the tip of the needle hydrophone. The needle hydrophone was then translated in 0.1-mm intervals along the three axes of the coordinate system using a motorized stereotax while measuring the peak-to-peak acoustic pressures. This allowed for the plotting of one-dimensional line profiles and two-dimensional plane profiles of the acoustic pressure of focal regions generated from a single TRA reference point.

To generate focal regions of complex shapes, the TRA-CED system combines regular-shape focal regions generated at multiple TRA reference points. The positions of these regular-shape focal regions are determined by first positioning a hydrophone at the desired locations and recording them in the TRA-CED system. For example, to create a rectangular focal region, six

reference points in a row were first recorded in the TRA-CED system by positioning the needle hydrophone at each point in the row.

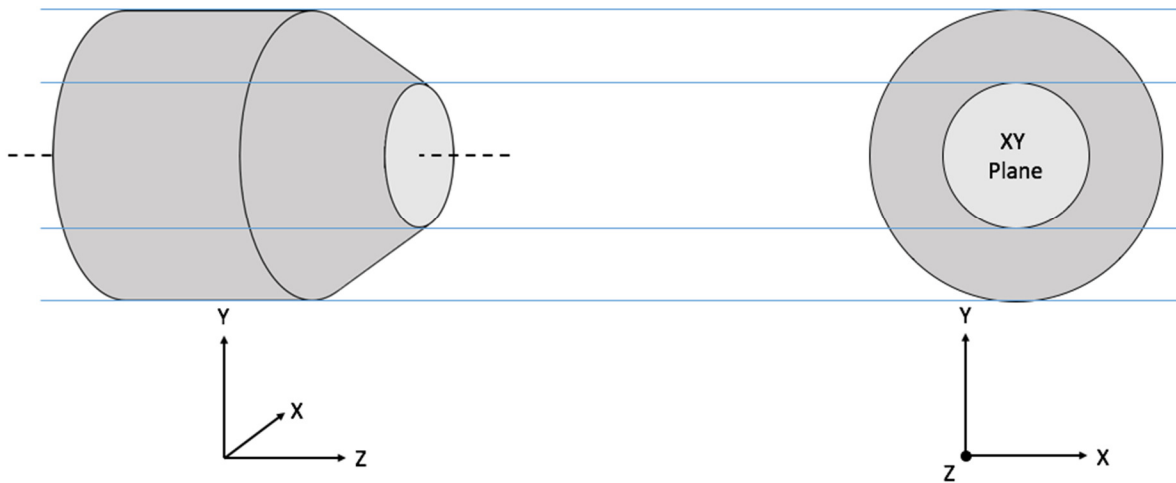


Figure 3.1: The coordinate system used in this chapter is set with respect to the orientation of the reverberator. The XY-plane is parallel to the flat surface on the front face of the reverberator, while the Z-axis coincides with the axis of the reverberator. The coordinate $(0,0,0)$ corresponds to the location of the tip of the needle hydrophone when the first reference point is created—this also corresponds to the center of the region of focused ultrasound generated based on that reference point.

3.2.4 Characterization of the Region of Ultrasound Focus in the Rat Brain In Vivo

A male albino Sprague Dawley rat weighing 321 g was anesthetized using 2% isoflurane gas mixed with oxygen. A heating pad was used to maintain the body temperature of the rat during the experiment. A 1-cm diameter burr hole was drilled on the right side of the rat skull, and the dura mater was removed. After the brain was exposed, ultrasound transmission gel was applied onto the front face of the 0.5 MHz reverberator, which was then positioned on top of the rodent skull (Figure 3.2). The needle hydrophone was inserted medially into the rat brain to a position 0.7 mm anterior, 5.4 mm inferior, and 2.9 mm lateral to bregma; this position coincides with the center of the caudate putamen⁷⁰. The TRA-CED system was then set up to focus ultrasound at the location corresponding to the tip of the needle hydrophone. After the ultrasound focal region was generated, the needle hydrophone was translated in 0.2-mm intervals along the x axis (medial-lateral of rodent skull) of the coordinate system using a manual stereotax while measuring the peak-to-peak acoustic pressures. For translations along the y (rostral-caudal) and z (inferior-superior) axes, the needle hydrophone had to first be removed from the rodent brain, translated, and then reinserted back into the brain at the new location, since not doing so would result in the needle hydrophone ripping the brain tissue with each translation. This allowed for the plotting of one-dimensional line profiles of the acoustic pressure of a focal region generated from a single TRA reference point. For the two-dimensional plane profile, the translation intervals along the y and z axes were increased to 0.5 mm to reduce structural damage to the rodent brain while the profile was obtained. At the end of the experiment, the rat was euthanized with a lethal dose of pentobarbital.

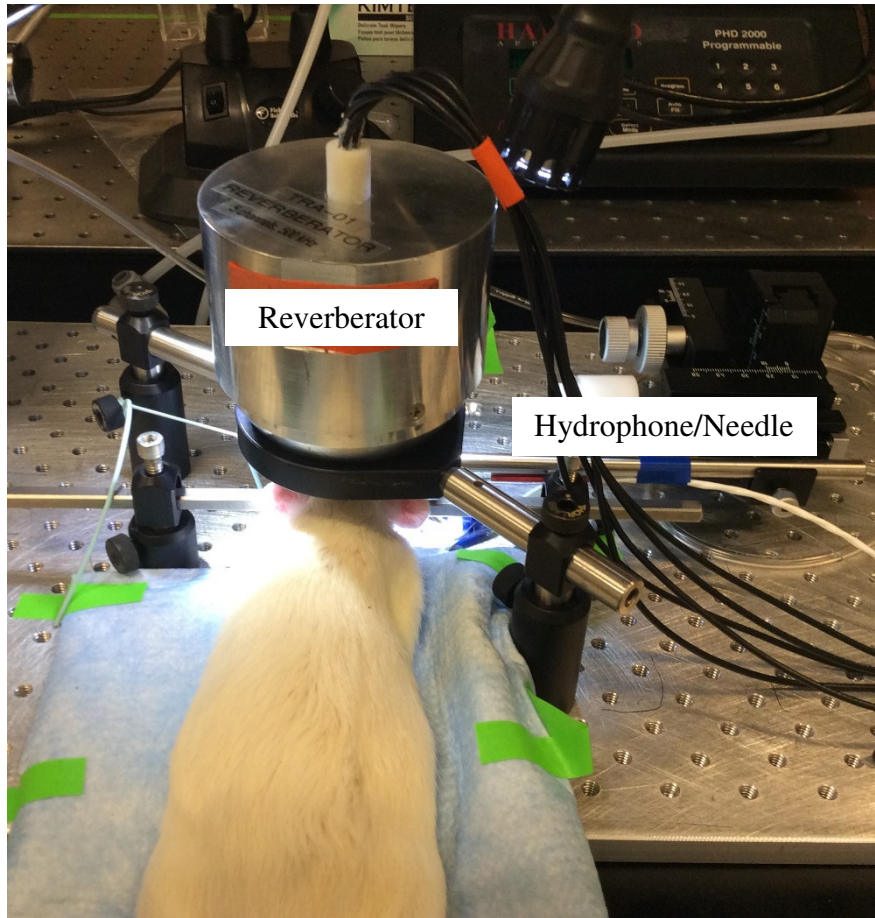


Figure 3.2: The experimental setup to study the effect of TRA-focused ultrasound on tracer distribution in vivo in rat brains.

3.2.5 Agarose Gel Experiments with Ultrasound Focused Adjacent to Site of Infusion

To study the effects of focused ultrasound on tracer distribution in agarose gels, 5% wt/vol Evans blue-labeled bovine serum albumin (EBA) (MW \approx 66 kDa) was infused via CED into 50-mL volumes of 0.2% wt/vol agarose gels stored in T-25 cell culture flasks as shown in Figure 3.3.

To create a focal region adjacent to the site of infusion, the needle hydrophone was paired with an infusion needle that was set at a fixed distance of 2.8 mm away. This distance was selected so that the Half Width at Half Maximum based on the acoustic pressure profiles fell in between the infusion needle and the needle hydrophone, allowing for the comparison of the distribution volume inside and outside the ultrasound focal region. A digital thermometer with a k-probe was included to measure the temperature of the agarose gel during cooling as well as during the experiment. The infusion needle was first primed with EBA, after which the needle hydrophone, infusion needle, and k-probe thermometer were placed in a T-25 cell culture flask filled with hot liquid 0.2% wt/vol agarose. The agarose was allowed to cool and solidify around the hydrophone, infusion needle, and thermometer, ensuring there would be no cracks in the gel that would bias the distribution of the infused tracer. Once the agarose gel had solidified and cooled to room temperature, the infusion pump was switched on at a flowrate of 0.2 μ L/min for 30 mins. For the ultrasound treatment group, TRA-focused 0.5 MHz ultrasound waves were focused at the tip of the needle hydrophone throughout the infusion duration.

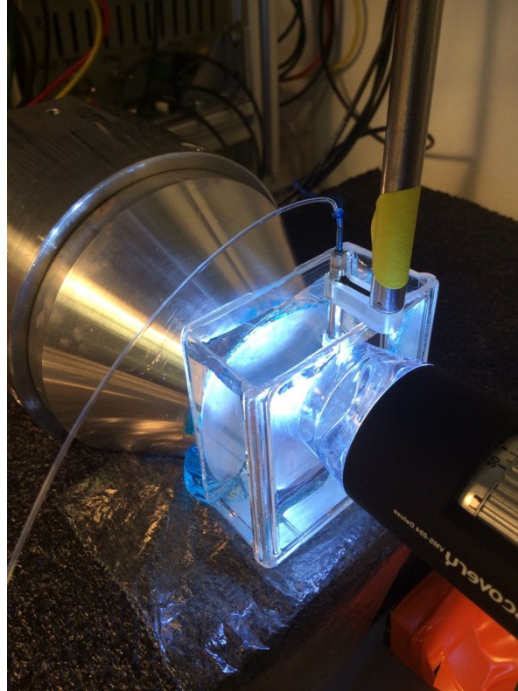


Figure 3.3: The experimental setup to study the effect of focused ultrasound on tracer distribution in 0.2% wt/vol agarose gels.

3.2.6 Imaging and Image Analysis of Agarose Gel Experiments

Images of the infusion were recorded using a microscope camera (Veho #VMS-004) and the time-lapse video recording software VideoVelocity (CandyLabs) at five-second intervals throughout the duration of the experiment. The images that corresponded with the 0, 10, and 20-minute time points were processed and analyzed using the image processing package Fiji⁷¹.

The images were first converted from RGB to Binary using a common threshold. To remove the needle track, the image at the 0-min time point was subtracted from the images of the 10 and 20-minute time points. Using the middle of the needle track as the midline, the left and right radii as well as the left and right areas of the infusion cloud were measured. These values were then used to determine the radii and area ratios of dye that traveled towards the ultrasound focal region (rightward) and dye that traveled away from the ultrasound focal region (leftward).

The images at the 30-minute time point were not used because the dye had traveled past the needle hydrophone, and the presence of the latter prevented the accurate determination of the radius and area of distribution of the dye.

3.2.7 In Vivo Rat Experiments with Ultrasound Focused Adjacent to or at Site of Infusion

Male albino Sprague Dawley rats weighing between 267 and 397 g were used in these experiments. The experimental setup is similar to that described in Section 3.2.4. Briefly, each rat was anesthetized using 2% isoflurane gas mixed with oxygen, and a heating pad was used to

maintain the body temperature of the rat during the experiment. A burr hole was created on the right side of the rat skull, and the dura mater removed. After the brain was exposed, the reverberator was placed on top of the rodent skull (Figure 3.2). The infusion needle was then primed with either dye alone or a 1:1 mixture of dye and microbubbles. The microbubbles were always re-suspended by hand agitation just prior to use to ensure that the microbubbles were intact and well-distributed for the experiment.

For the experiments in which ultrasound is focused adjacent to the site of infusion, the dye and microbubbles used are 5% EBA and Targestar P microbubbles (Targeson TS-108), respectively. Because the needle hydrophone needed to be placed at the reference point in the rodent brain in order to generate a region of focused ultrasound adjacent to the site of infusion, the needle hydrophone was again paired with an infusion needle, and set either 1 or 2 mm apart. Two distances were selected as the distribution of the dye could not be observed in real time, but rather only after the experiment. Both the infusion needle and needle hydrophone were inserted simultaneously into the rat brain, with the needle hydrophone being either 1 or 2 mm rostral to the infusion needle.

For experiments conducted with maximum peak-to-peak acoustic pressures of approximately 8 MPa and an infusion needle–needle hydrophone distance of 1 mm, the final location of the infusion needle was set to 0.7 mm anterior, 5.4 mm inferior, and 2.9 mm lateral to bregma, which coincides with the center of the caudate putamen⁷⁰. This brain region in rats is typically selected for being a relatively homogenous volume of gray matter. For the experiments conducted with maximum peak-to-peak acoustic pressures of approximately 8 MPa and an

infusion needle–needle hydrophone distance of 2 mm, the final location of the infusion needle was set to 5.4 mm inferior and 2.9 mm lateral to bregma with no anterior adjustment, since the anterior movement would put the needle hydrophone outside the circumference of the burr hole. For the experiments conducted with maximum peak-to-peak acoustic pressures of approximately 2 MPa and an infusion needle–needle hydrophone distance of 1 mm, the final location of the infusion needle was also set to 5.4 mm inferior and 2.9 mm lateral to bregma with no anterior adjustment. In these latter two cases, the site of infusion is still within the caudate putamen⁷⁰. These parameters are summarized in Table 3.1.

For the experiments in which ultrasound is focused at the site of infusion, the dye and microbubble pairings are either 5% EBA and Targestar P microbubbles, or 0.25% EB and Lumason microbubbles (Braco Diagnostics 709916). Only the needle hydrophones that allow CED as well are used in these experiments. These parameters are summarized in Table 3.2.

Both Targestar P and Lumason microbubbles have gas cores that are encapsulated by phospholipid shells coated with polyethylene glycol (PEG). While Targestar P microbubbles contain a perfluorocarbon gas (C_4F_{10}), Lumason microbubbles contain sulfur hexafluoride (SF_6). Both gases have very poor solubility in water⁷². The stock solution of Targestar P contains approximately 1×10^9 microbubbles/mL with a mean bubble diameter of 2.2 μm , whereas the stock solution of Lumason contains approximately 5×10^8 microbubbles/mL with a mean bubble diameter of 2.5 μm ³⁷. While the reported mean bubble sizes were similar between the two brands, the concentration of microbubbles differed by a factor of two. The characteristics of the Targestar P and Lumason microbubbles are summarized in Table 3.3.

After the infusion needle and/or needle hydrophone were inserted, the TRA-CED system was set up to focus either 0.5 or 1 MHz ultrasound at the tip of the needle hydrophone. For Ultrasound experiments, the focused ultrasound and the infusion pump, which was set at a flowrate of 0.2 $\mu\text{L}/\text{min}$, were turned on simultaneously. For the no-ultrasound Control experiments, only the infusion pump was turned on at the start of the experiment. After 2.5 minutes, the infusion pump was turned off, resulting in a total infusion volume of 0.5 μL . The experiment was allowed to continue for another 27.5 minutes, for a total experiment duration of 30 minutes.

At the end of the experiments, the rats were euthanized with a lethal dose of pentobarbital. The rats were then perfused transcardially with at least three times the blood volume of 1X PBS, followed by 4% paraformaldehyde. The rodent brains were then extracted and soaked in 4% paraformaldehyde overnight. This surgical procedure was performed in accordance with Cornell University's Institutional Animal Care and Use Committee regulations.

Table 3.1: Summary of in vivo rat brain experiments with ultrasound focused adjacent to the infusion site. There are ten groups in total.

Pk-to-Pk Acoustic Pressure (MPa)	Infusion Needle– Needle Hydrophone distance (mm)	Anterior Position of Infusion Needle with respect to Bregma (mm)	Microbubbles	Ultrasound	Sample Size
2	1	0	Microbubbles	Ultrasound	2
				Control	2
8	1	0.7	Microbubbles	Ultrasound	2
				Control	3
			Dye Only	Ultrasound	3
				Control	3
	2	0	Microbubbles	Ultrasound	4
				Control	4
			Dye Only	Ultrasound	2
				Control	2

Table 3.2: Summary of in vivo rat brain experiments with ultrasound focused at the infusion site.

There are five groups in total.

Frequency (MHz)	Mean Pk-Pk Acoustic Pressure (MPa)	Treatment	Dye + Microbubble in 1:1 ratio	Sample Size
0.5	0.2	Ultrasound	5% EBA +	6
		No Ultrasound	Targestar P	4
1	0.3	Ultrasound	0.25% EBD +	3
		No Ultrasound	Lumason	3
		No Ultrasound	0.25% EBD only	2

Table 3.3: Characteristics of microbubbles used in in vivo rat brain experiments.

Microbubble Brand	Stock Concentration ($\times 10^9$ /mL)	Mean Diameter (μm)	Gas Core	Shell
Targestar P	1	2.2	C ₄ F ₁₀	Phospholipid + PEG
Lumason	0.5	2.5	SF ₆	Phospholipid + PEG

3.2.8 Imaging and Image Analysis of In Vivo Rodent Experiments

Prior to cryosectioning, the rat brains were immersed through a series of 30% and 60% sucrose solutions for cryoprotection. The rat brains were then embedded in Optimal Cutting Temperature (OCT) media and frozen. The region of the rat brains containing dye were then serially sectioned in 50- μm intervals using a cryotome. Reflectance images of these coronal sections—beginning with the section in which the blue dye is first visible and ending with the section that no longer contains any blue dye—were taken using a microscope camera (Veho #VMS-004) and the recording software VideoVelocity (CandyLabs). Images of a ruler were obtained to determine the scale of the images.

These reflectance images were then processed and analyzed using Fiji⁷¹ and Matlab. The images from each rat brain was converted into a single stack. The RGB image stack was deconvolved⁷³ to extract only the blue color of the Evans blue dye, resulting in an 8-bit image stack. The slice containing the infusion needle tip was selected, and the hemisphere of the brain contralateral to the infusion site was used to determine the mean pixel value of the background and the standard deviation. The 8-bit image stack was then converted to a binary image stack using a minimum threshold that was set at 8 standard deviations above the mean pixel value of the background—any pixel with a value above the threshold was considered to represent a dyed region.

Matlab was then used to calculate the total number of dye pixels for each slice as well as for each image stack. The scale for each stack and the slice interval of 50 μm were then used to convert the pixel data into the dyed area of each brain slice and the total dye distribution volume (V_d) of

each image stack. The V_d was used to calculate the distribution volume to infusion volume (V_i) ratio, V_d/V_i . Using the slice containing the infusion needle tip as a reference, the total volume of dye rostral to the infusion needle tip (towards ultrasound focal region) was divided by the total volume of dye caudal to the infusion needle tip (away from ultrasound focal region) to determine the rostral V_d to caudal V_d ratio.

Infusions that showed evidence of backflow were excluded from the analysis. Based on the remaining infusions that did not experience any backflow, the mean distribution volume and rostral V_d to caudal V_d ratio for each group of parameters were compared between Ultrasound and no-ultrasound Control experiments. The mean dyed areas of the brain slices for each experimental group were also plotted with respect to the Caudal-Rostral distance from the infusion site.

3.2.9 Statistical Analysis

Two-tailed t-tests assuming unequal variances and a significance level of 0.05 were performed on the two null hypotheses—comparing Ultrasound and Control experiments of each group of parameters, the difference in the mean distribution volumes is zero and the difference in the ratios of rostral to caudal dye distribution volumes is zero.

3.3 Results

3.3.1 Characterization of the Region of Ultrasound Focus in Water and Agarose Gel

One-dimensional line profiles of the peak-to-peak acoustic pressure of focal regions generated by the TRA-CED system from the same single reference point in water at 25 °C using 0.5 MHz ultrasound and amplifier input voltages of $\pm 1.5\text{V}$ and $\pm 45\text{V}$ are shown in Figure 3.4 and Figure 3.5, respectively. The observed oscillations in the acoustic pressures were due to constructive and destructive interference of the ultrasound waves. The oscillations were most pronounced along the z axis, i.e., the axis of the reverberator, likely because the emitted ultrasound waves first travel along or at an acute angle to the z axis, resulting in significant interference along this axis before they can reflect and scatter within the vessel. When using the same reference point to generate the focused ultrasound, increasing the amplifier input voltage by 30 times increased the peak acoustic pressure by a factor of 24.3, but did not significantly alter the Full Widths at Half Maximum (FWHM) along the three axes. This suggests that the shape of the focal region is independent of the amplifier input voltage and the corresponding acoustic pressures generated when all other conditions are kept constant.

One-dimensional line profiles of the peak-to-peak acoustic pressure of a focal region generated by the TRA-CED system from a single reference point in water at 25 °C using 1 MHz ultrasound and an amplifier input voltage of $\pm 3.0\text{V}$ are shown in Figure 3.6. As with the 0.5 MHz ultrasound, the oscillations were most pronounced along the z axis. The FWHM along the three

axes were approximately half of that observed for the 0.5 MHz ultrasound. This is likely due to the wavelength of the 1 MHz ultrasound being half that of the 0.5 MHz ultrasound.

A two-dimensional plane profile of the peak-to-peak acoustic pressure of a focal region generated by the TRA-CED system from the same single reference point in water at 25 °C using 0.5 MHz ultrasound and an amplifier input voltage of ± 1.0 is shown in Figure 3.7. The FWHM along the x and y axes were slightly larger than those obtained in the one-dimensional line profiles, but these differences were likely due to having used a different reference point as well as a lower amplifier input voltage such that the maximum peak-to-peak acoustic pressure was only a quarter of that of the one-dimensional profiles.

A two-dimensional plane profile of the peak-to-peak acoustic pressure of a complex-shape focal region generated by the TRA-CED system from six different reference points spaced 2 mm apart in water at 25 °C using 0.5 MHz ultrasound is shown in Figure 3.8. The shapes of focal regions generated using TRA-focused ultrasound are dependent on the reference points selected.

The acoustic pressure profiles conducted in 0.2% wt/vol agarose gel were indistinguishable from those conducted in water.

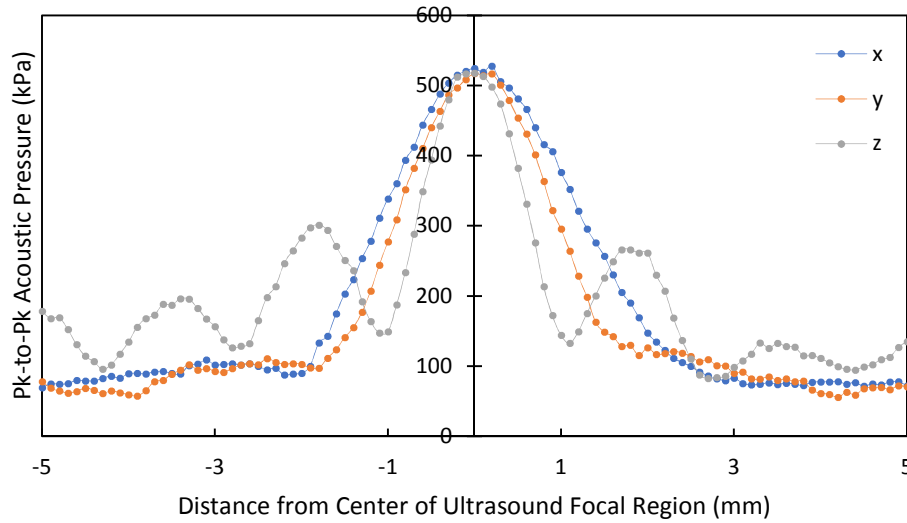


Figure 3.4: The peak-to-peak acoustic pressure profile of the region of focused 0.5 MHz ultrasound generated using a single reference point with the amplifier input voltage set at $\pm 1.5V$. This was performed in a T-25 cell culture flask filled with 50 mL of RODI water. The maximum peak-to-peak acoustic pressure was 0.538 MPa. The FWHM were approximately 2.8, 2.2, and 1.4 mm along the X, Y, and Z-axes, respectively.

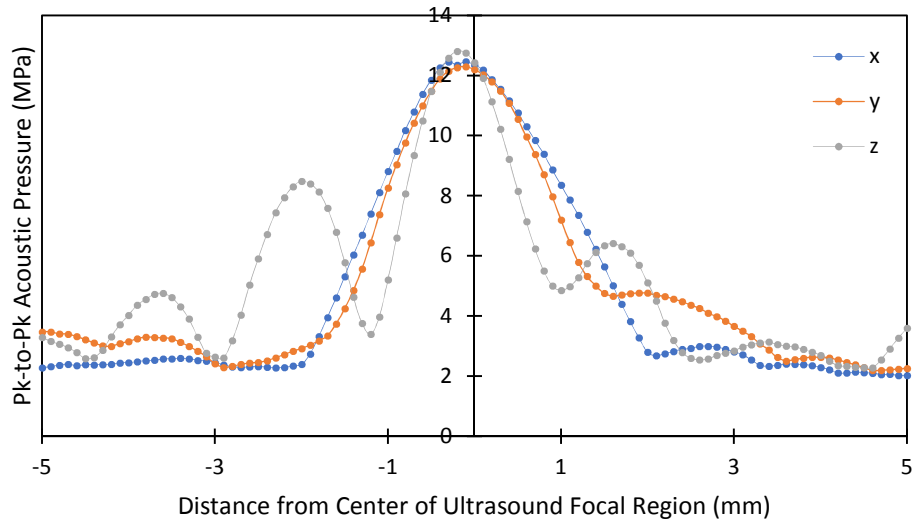


Figure 3.5: The peak-to-peak acoustic pressure profile of the region of focused 0.5 MHz ultrasound generated using a single reference point with the amplifier input voltage set at $\pm 45V$. This was performed in a T-25 cell culture flask filled with 50 mL of RODI water. The maximum peak-to-peak acoustic pressure was 12.8 MPa. The FWHM were approximately 2.8, 2.3, and 1.6 mm along the X, Y, and Z-axes, respectively.

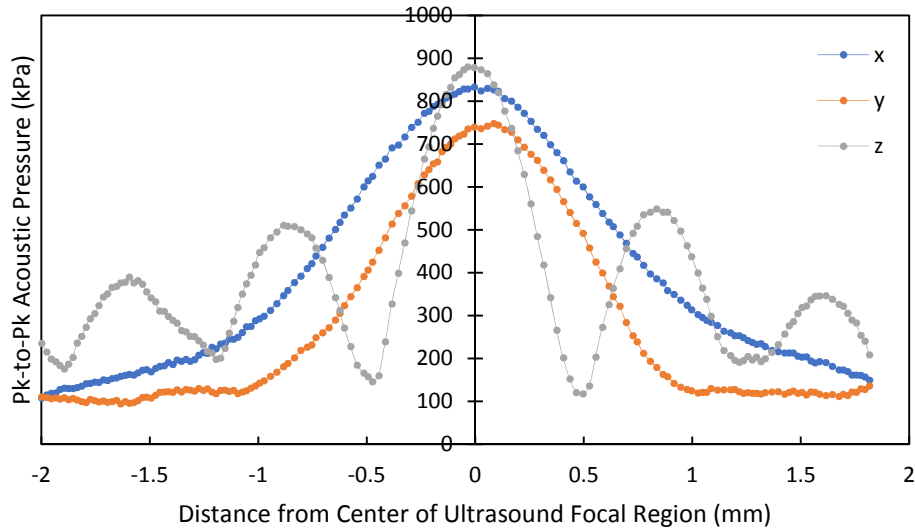


Figure 3.6: The peak-to-peak acoustic pressure profile of the region of focused 1 MHz ultrasound generated using a single reference point with the amplifier input voltage set at $\pm 3.0V$. This was performed in a clear plastic flask filled with 200 mL of RODI water. The maximum peak-to-peak acoustic pressure was 0.880 MPa. The FWHM were approximately 1.5, 1.2, and 0.6 mm along the X, Y, and Z-axes, respectively.

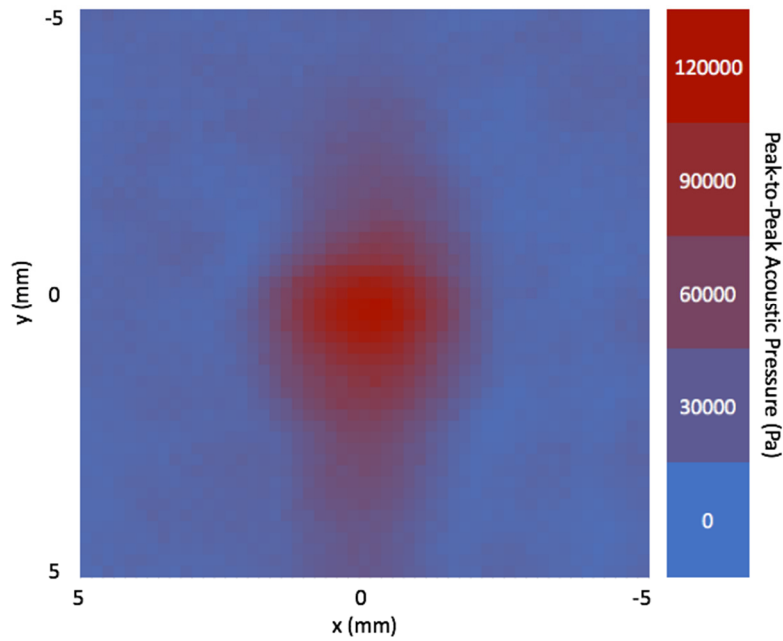


Figure 3.7: The peak-to-peak acoustic pressure profile along the central XY-plane of the region of focused 0.5 MHz ultrasound generated using a different single reference point with the amplifier input voltage set at $\pm 1V$. This was performed in a T-25 cell culture flask filled with 50 mL of RODI water. The maximum peak-to-peak acoustic pressure was 0.125 MPa. The FWHM were approximately 3.2 and 4.0 mm along the X and Y-axes, respectively.

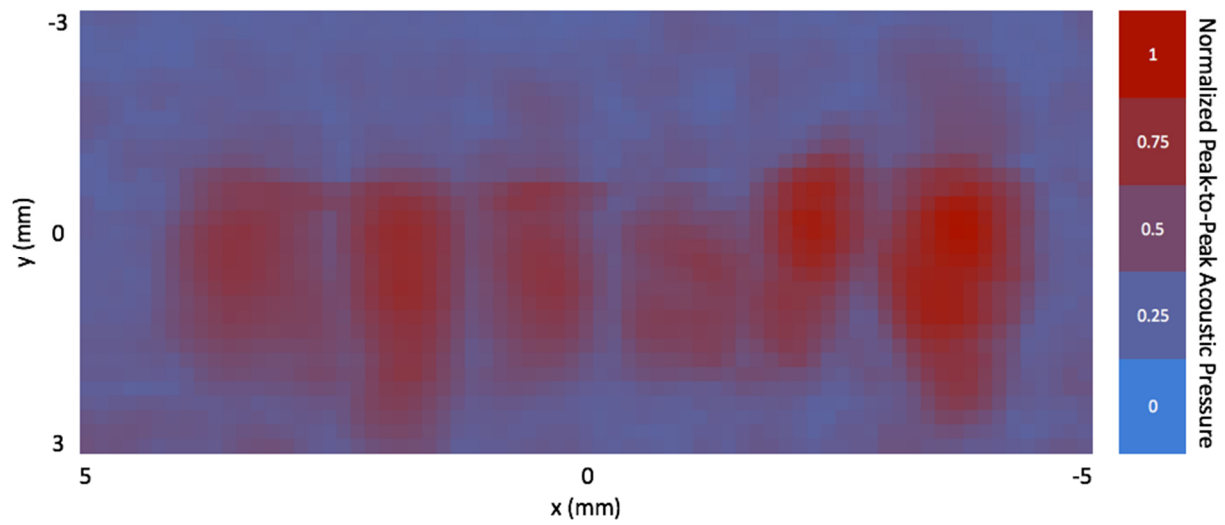


Figure 3.8: An example of the complex-shape focal region of 0.5 MHz ultrasonic waves generated by the TRA-CED system based on 6 reference points separated by 2-mm intervals. The 2D profile was normalized by dividing each value by the maximum peak-to-peak acoustic pressure. This was performed in a 250 mL PYREX beaker filled with RODI water.

3.3.2 Characterization of the Region of Ultrasound Focus in the Rat Brain In Vivo

One-dimensional line profiles of the peak-to-peak acoustic pressure of focal regions generated by the TRA-CED system from the same single reference point in rat brain in vivo at ~ 37 °C using 0.5 MHz ultrasound and an amplifier input voltage of ± 1.8 are shown in Figure 3.9. Unlike with the focal regions measured in water, there do not appear to be multiple lobes that occur along the z axis in the rat brain, which may explain the much larger full width at half maximum along this axis.

Two-dimensional plane profiles of the peak-to-peak acoustic pressure of focal regions generated by the TRA-CED system from the same single reference point in rat brain in vivo at ~ 37 °C using 0.5 MHz ultrasound and an amplifier input voltage of ± 1.8 are shown in Figure 3.10 and Figure 3.11. Because the translation interval used to obtain the acoustic pressure profiles along the y and z axes was the relatively large 0.5 mm, the resolution was insufficient to determine the FWHM for these axes.

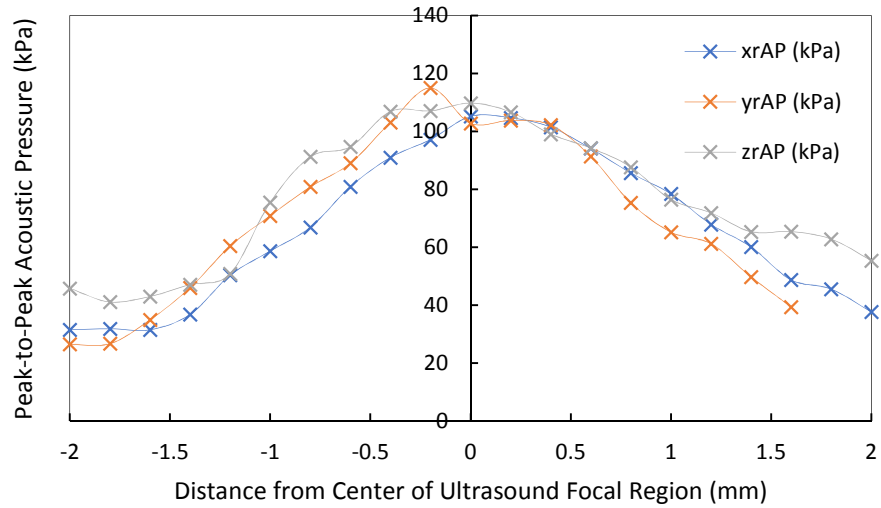


Figure 3.9: The peak-to-peak acoustic pressure profile of the region of focused 0.5 MHz ultrasound generated using a single reference point with the amplifier input voltage set at $\pm 1.8V$. This was performed in vivo in a rat brain. The maximum peak-to-peak acoustic pressure was 0.115 MPa. The FWHM were approximately 2.8, 2.4, and 3.2 mm along the X, Y, and Z-axes, respectively. Unlike with the focal region measured in water, there does not appear to be multiple lobes that occur along the Z-axis, which explains the much larger FWHM.

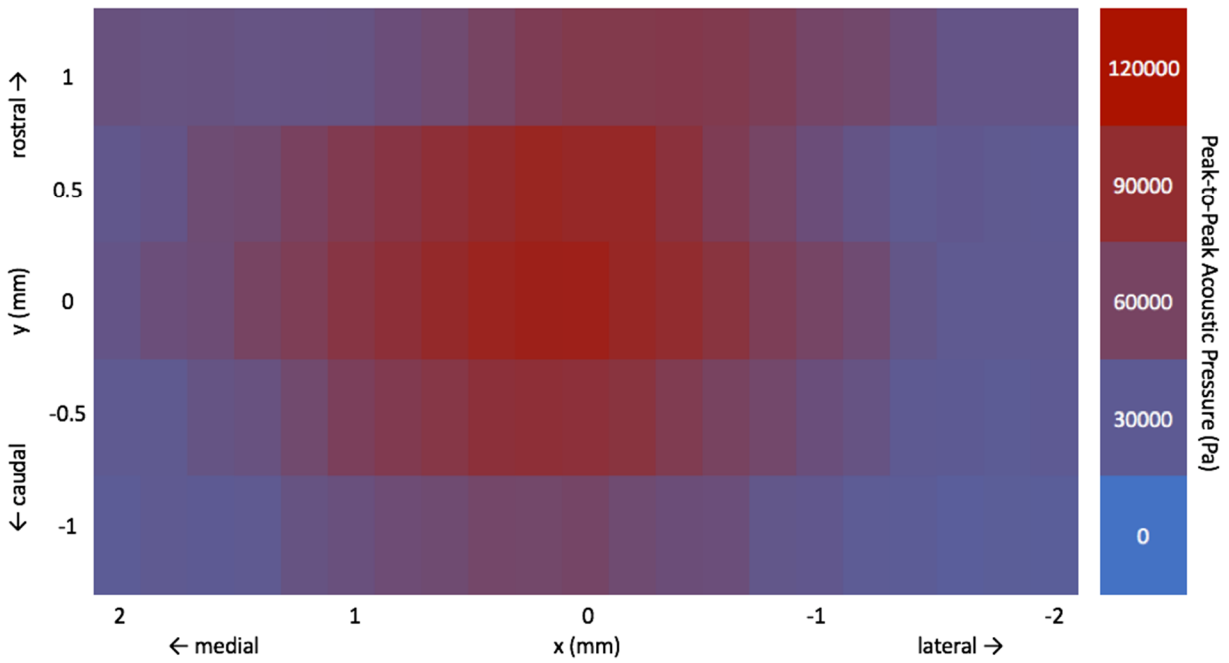


Figure 3.10: A color map displaying the peak-to-peak acoustic pressures of the central XY-plane, which is parallel to the face of the reverberator, of the region of focused ultrasound in vivo in a rat brain. The amplifier input voltage was set at $\pm 1.8\text{V}$. The origin is the location of the ultrasound probe when the reference point was obtained. The maximum peak-to-peak acoustic pressure was 0.115 MPa. The FWHM along the X-axis was 2.8 mm. The resolution of the Y-axis was insufficient to determine the FWHM along the Y-axis.

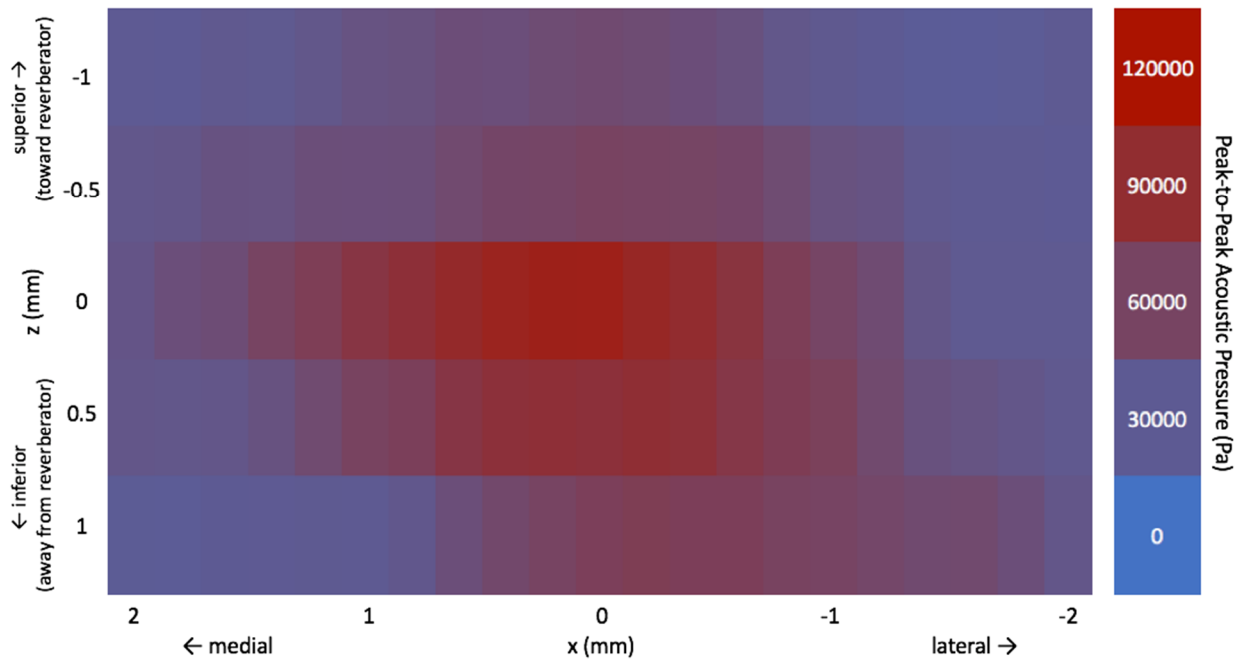


Figure 3.11: A color map displaying the peak-to-peak acoustic pressures of the central XZ-plane, which is perpendicular to the face of the reverberator, of the region of focused ultrasound in vivo in a rat brain. The amplifier input voltage was set at $\pm 1.8V$. The origin is the location of the ultrasound probe when the reference point was obtained. The maximum peak-to-peak acoustic pressure was 0.115 MPa. The FWHM along the X-axis was 2.8 mm. The resolution of the Z-axis was insufficient to determine the FWHM along the Z-axis.

3.3.3 Agarose Gel Experiments with Ultrasound Focused Adjacent to Site of Infusion

Representative images of the ultrasound and control agarose gel experiments taken at the 20-minute time point are shown in Figure 3.12. Comparing the radii and area ratios of dye that traveled towards the ultrasound focal region (rightward) and dye that traveled away from the ultrasound focal region (leftward) at the 10 and 20-minute time points, there was no significant difference detected between ultrasound and control experiments for both parameters (Figure 3.13). These results suggest that TRA-focused 0.5 MHz ultrasound waves do not appear to bias the distribution volume of infused EBA towards or away from the focal region.

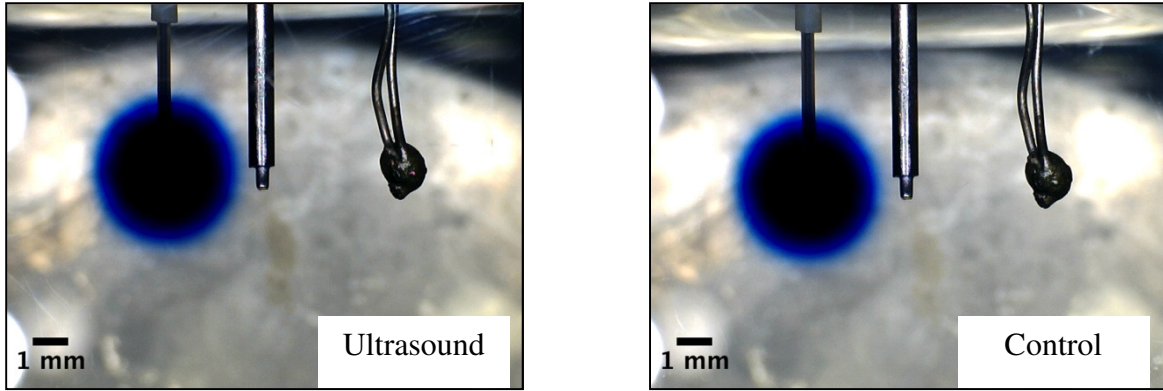


Figure 3.12: Representative images of the ultrasound and no-ultrasound control experiments taken at the 20-minute time point. The infusion needle was placed 2.8 mm to the left of the needle hydrophone, while the k-probe thermometer was placed to the right to monitor changes in gel temperature. Using the middle of the needle track as the midline, the left and right radii as well as the left and right areas of the infusion cloud were used to calculate the radii and area ratios of dye that traveled towards the ultrasound focal region (rightward) and dye that traveled away from the ultrasound focal region (leftward).

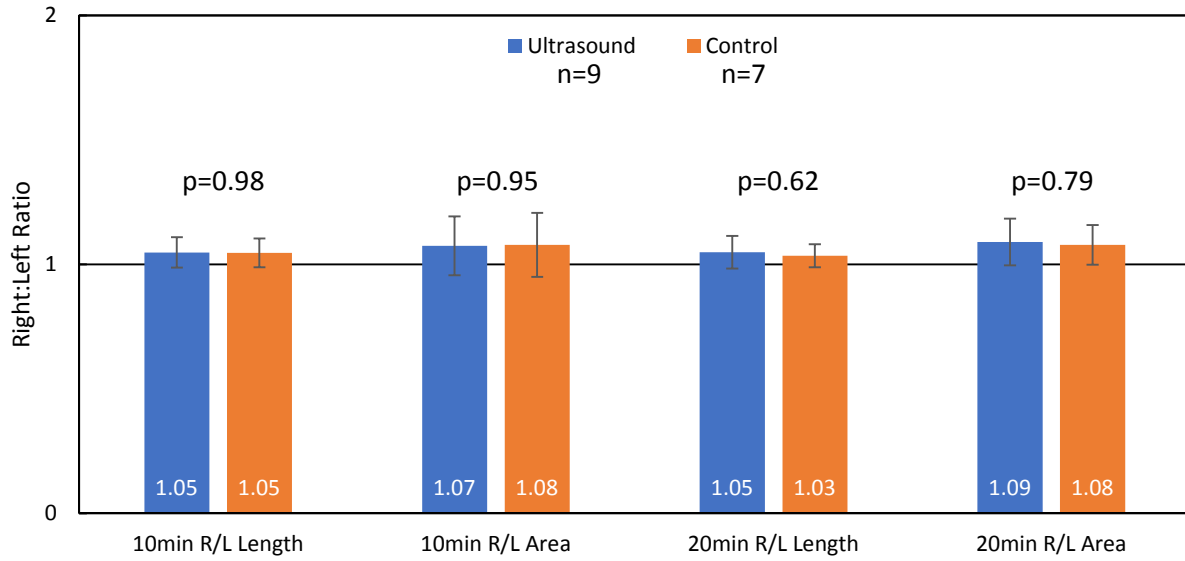


Figure 3.13: The radii and area ratios of dye that traveled towards the ultrasound focal region (rightward) and dye that traveled away from the ultrasound focal region (leftward). At $\alpha = 0.05$, there was no significant difference detected between ultrasound and no-ultrasound control experiments for both parameters after 10 and 20 minutes of infusion.

3.3.4 In Vivo Rat Experiments with 0.5 MHz Ultrasound Focused Adjacent to Site of Infusion

For in vivo rat experiments in which 0.5 MHz ultrasound was focused either 1 or 2 mm rostral to the site of infusion, no significant differences were found between ultrasound and no-ultrasound control experiments in terms of mean EBA distribution volume (Figure 3.14) and the mean rostral V_d to caudal V_d ratio (Figure 3.15) regardless of whether the dye was co-infused with Targestar P microbubbles, or treated at peak-to-peak acoustic pressures of 2 MPa or 8 MPa.

To assess whether co-infusing EBA with Targestar P microbubbles increased the EBA distribution volume in the absence of ultrasound, the EBA distribution volumes for the no-ultrasound control experiments were categorized according to whether the dye was co-infused with microbubbles. Assuming that the location of the needle hydrophone (i.e., 1 mm or 2 mm rostral to the infusion needle) and the location of the infusion needle (i.e., 0 mm or 0.7 mm rostral to bregma) do not affect the distribution volume of the infusion, at $\alpha = 0.05$, there was no significant difference in the distribution volumes of the no-ultrasound control experiments regardless of whether microbubbles were present (Figure 3.16).

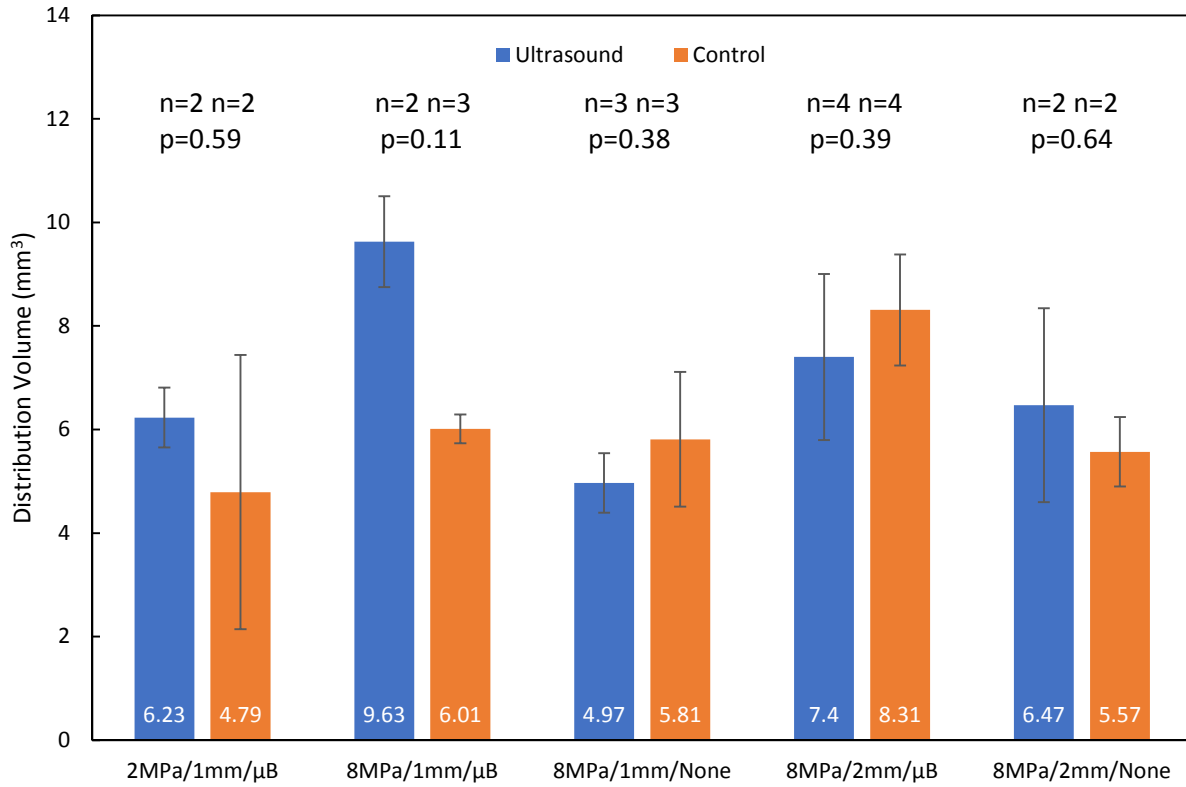


Figure 3.14: The means and standard deviations of the distribution volumes of the ultrasound and no-ultrasound control experiments from each experimental group are plotted. At $\alpha = 0.05$, there was no significant difference in the distribution volumes of the ultrasound and no-ultrasound control experiments in any of the experimental groups.

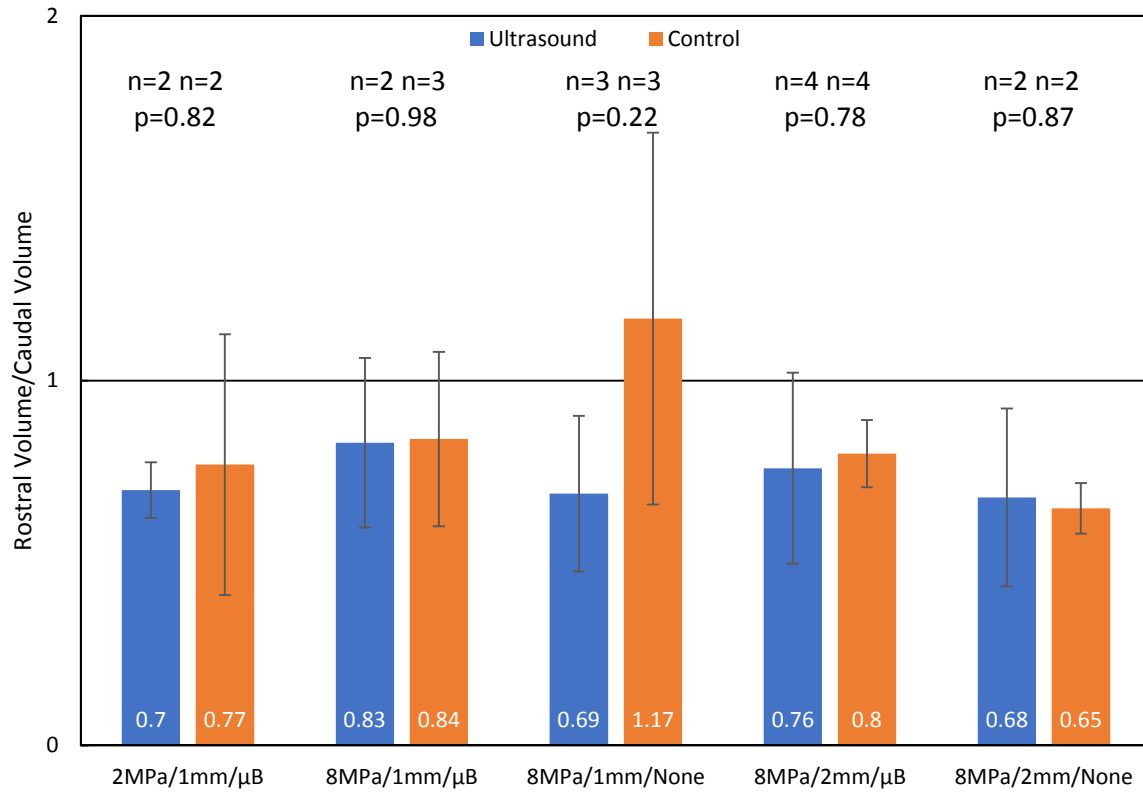


Figure 3.15: The means and standard deviations of the rostral V_d to caudal V_d ratios of the ultrasound and no-ultrasound control experiments from each experimental group are plotted. At $\alpha = 0.05$, there was no significant difference in the rostral V_d to caudal V_d ratios of the ultrasound and no-ultrasound control experiments in any of the experimental groups.

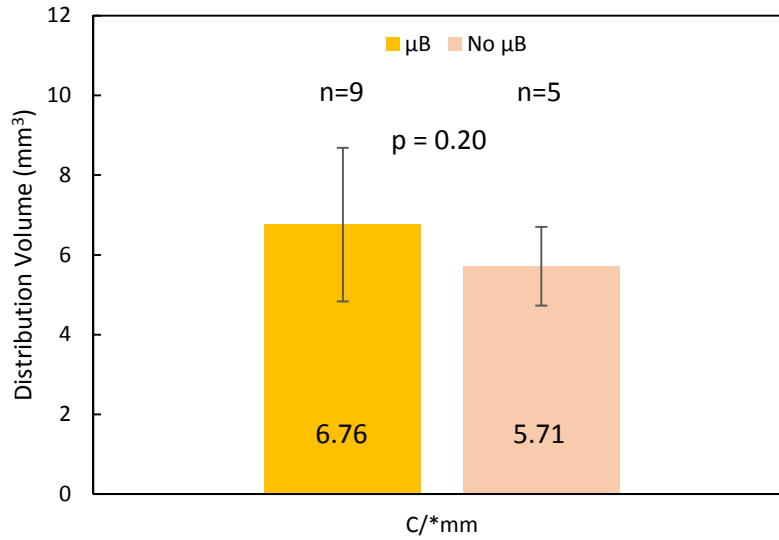


Figure 3.16: The means and standard deviations of the distribution volumes of Evans blue–labeled albumin for only the no-ultrasound control experiments, with and without microbubbles, are plotted. This plot assumes that the location of the needle hydrophone (i.e., 1 mm or 2 mm rostral to the infusion needle) and the location of the infusion needle (i.e., 0 mm or 0.7 mm rostral to bregma) do not affect the distribution volume of the infusion. At $\alpha = 0.05$, there was no significant difference in the distribution volumes of the no-ultrasound control experiments regardless of whether microbubbles were present.

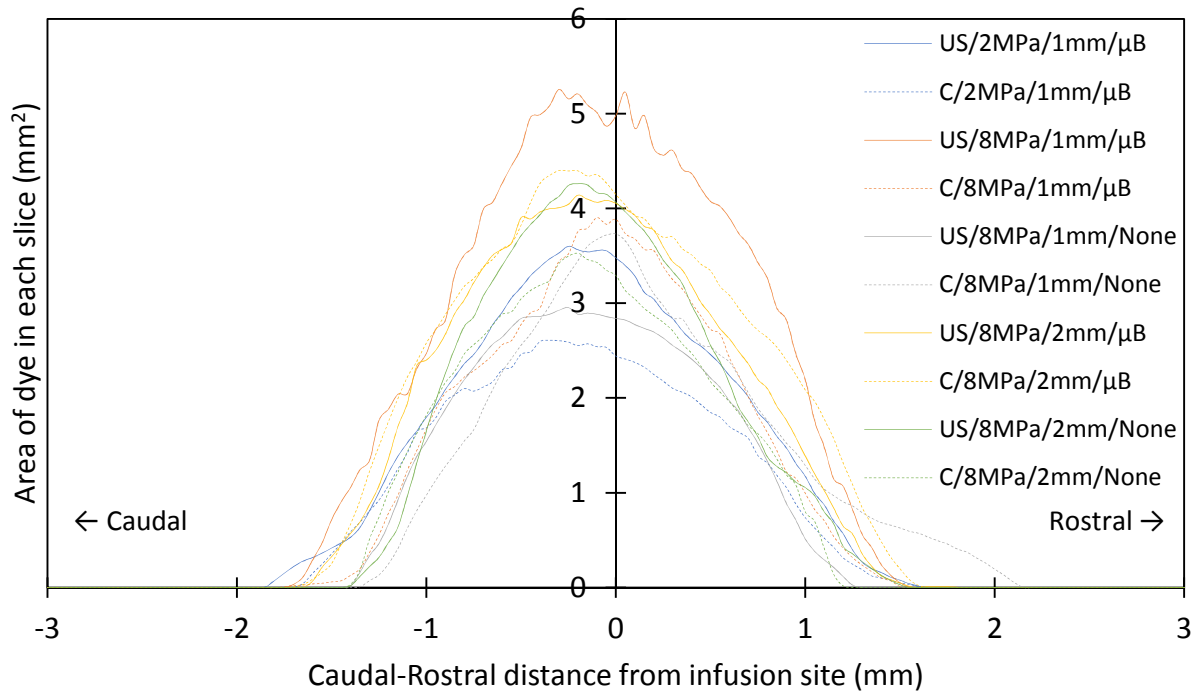


Figure 3.17: The mean dyed areas of the brain slices for each experimental group were plotted with respect to the Caudal-Rostral distance from the infusion site. The distribution volumes appeared to be slightly shifted towards the caudal direction, which corresponds to the rostral V_d to caudal V_d ratios having values less than 1 for all the experimental groups except C/8MPa/1mm/None.

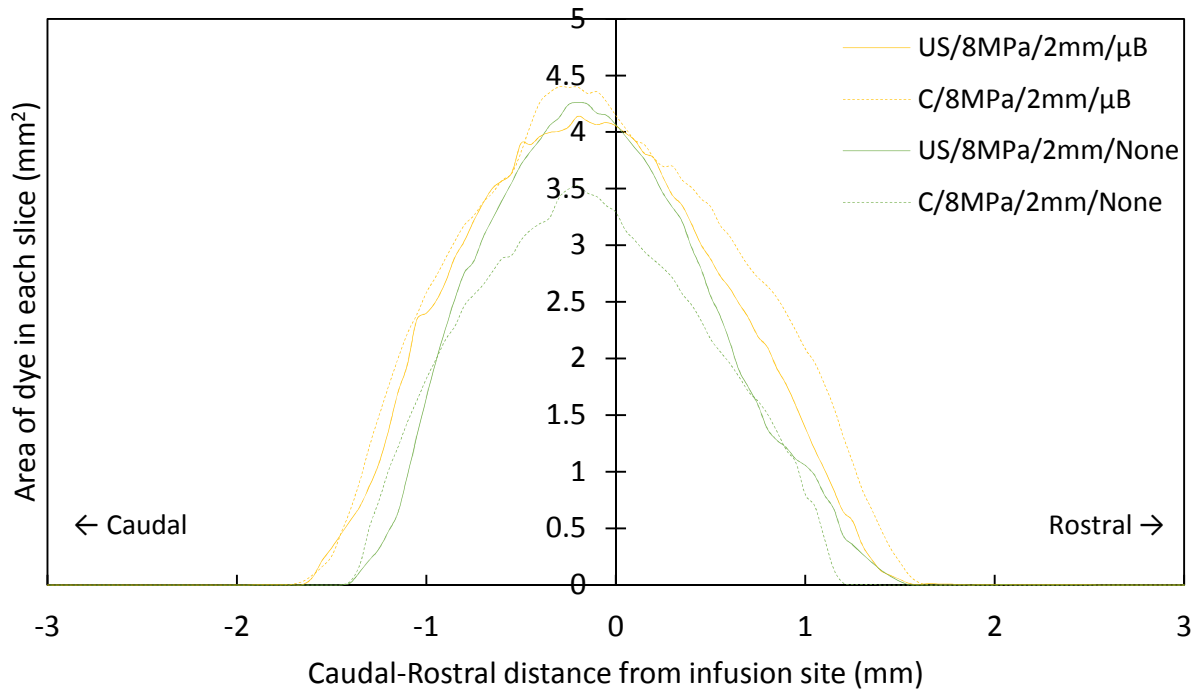


Figure 3.18: The mean dyed areas of the brain slices for the experiments conducted with maximum peak-to-peak acoustic pressures of approximately 8 MPa and an infusion needle–needle hydrophone distance of 2 mm with and without microbubbles were plotted with respect to the Caudal-Rostral distance from the infusion site. In addition to the distribution volumes having a slight bias towards the caudal direction, the slices with the largest mean dyed area are also caudal to the infusion site.

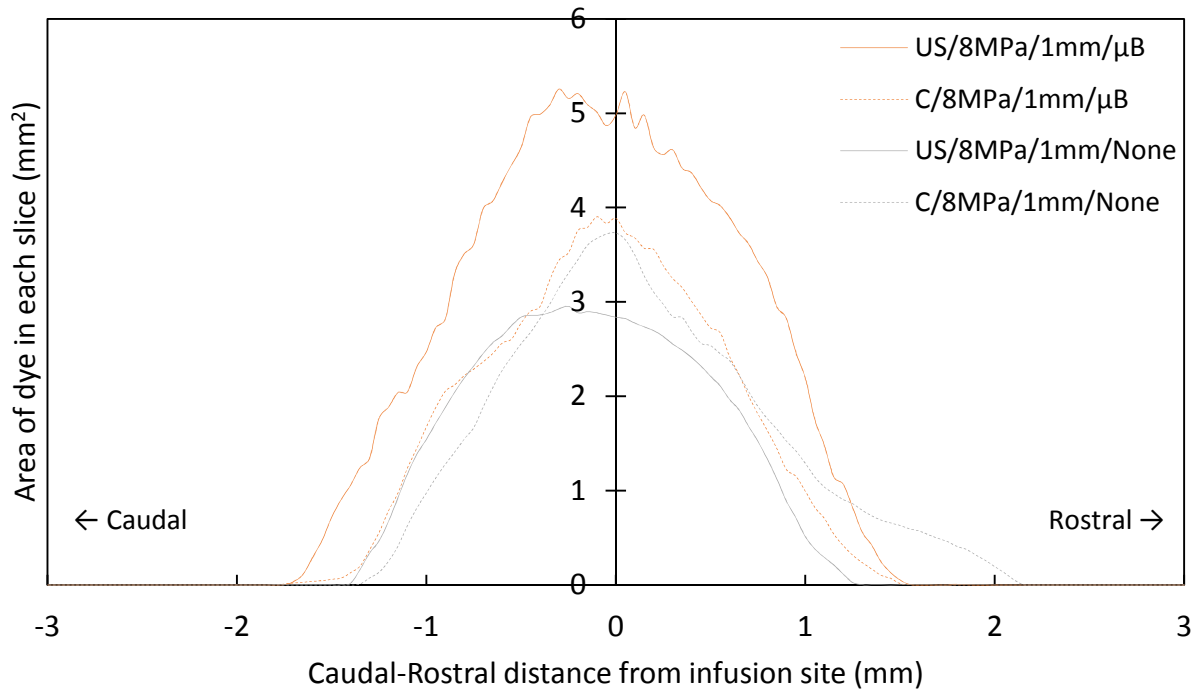


Figure 3.19: The mean dyed areas of the brain slices for the experiments conducted with maximum peak-to-peak acoustic pressures of approximately 8 MPa and an infusion needle–needle hydrophone distance of 1 mm with and without microbubbles were plotted with respect to the Caudal-Rostral distance from the infusion site. The distribution volumes of the experimental groups have a slight bias towards the caudal direction with the exception of C/8MPa/1mm/None, which has a slight bias towards the rostral direction as evidenced by the longer tail in the rostral direction. The slices with the largest mean dyed area for the ultrasound experiments are slightly caudal to the infusion site, whereas those of the control experiments are at or close to the

infusion site. Despite the larger area under the curve for US/8MPa/1mm/ μ B as compared to C/8MPa/1mm/ μ B, the distribution volume difference between the two groups is not significant.

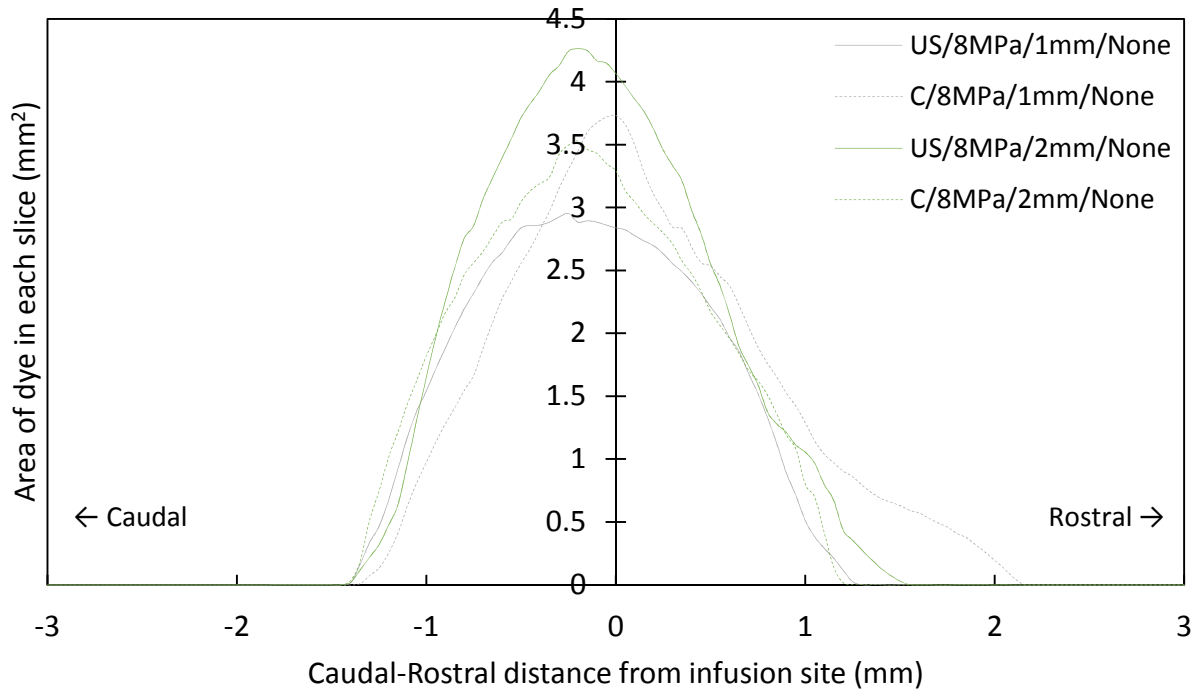


Figure 3.20: The mean dyed areas of the brain slices for the experiments conducted with maximum peak-to-peak acoustic pressures of approximately 8 MPa with no microbubbles and an infusion needle–needle hydrophone distance of either 1 or 2 mm were plotted with respect to the Caudal-Rostral distance from the infusion site. The distribution volumes of the experimental groups have a slight bias towards the caudal direction with the exception of C/8MPa/1mm/None, which has a slight bias towards the rostral direction. The slices with the largest mean dyed area for the experimental groups are slightly caudal to the infusion site, but again with the exception of C/8MPa/1mm/None, which has the slice with the largest mean dyed area at the infusion site.

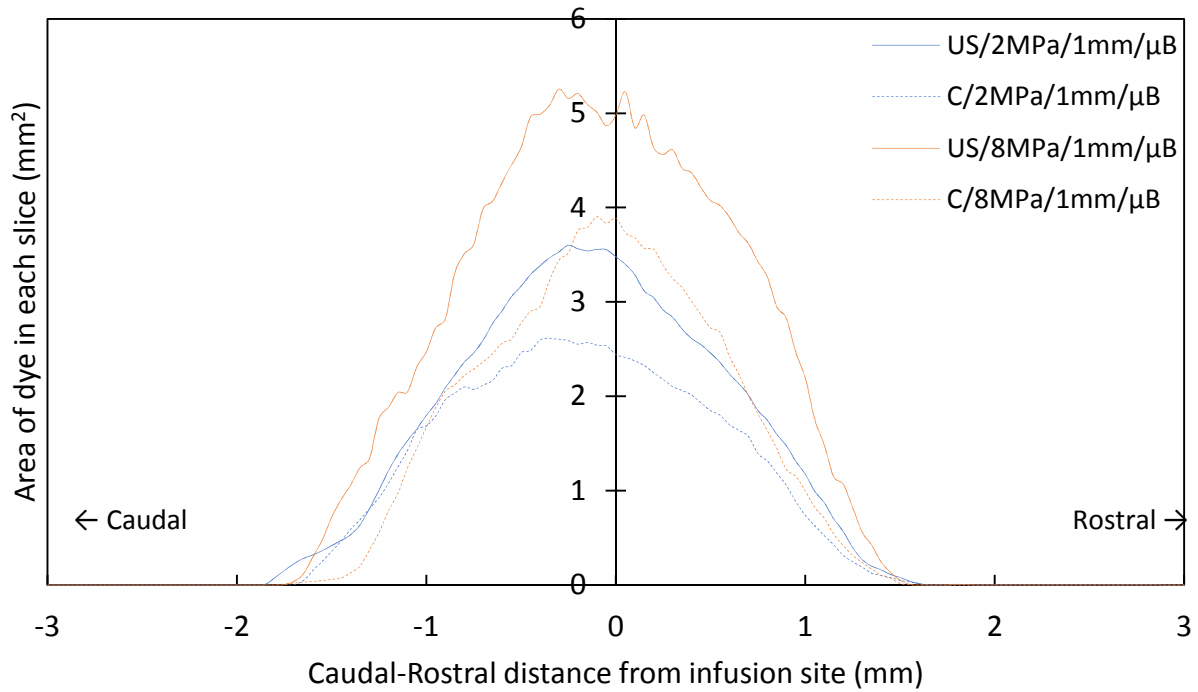


Figure 3.21: The mean dyed areas of the brain slices for the experiments conducted with maximum peak-to-peak acoustic pressures of approximately 2 or 8 MPa and an infusion needle–needle hydrophone distance of 1 mm with microbubbles were plotted with respect to the Caudal–Rostral distance from the infusion site. The distribution volumes of the experimental groups have a slight bias towards the caudal direction. The slices with the largest mean dyed area for the experiments are slightly caudal to the infusion site, except for that of C/8MPa/1mm/μB, which is almost at the infusion site. As mentioned previously, despite the larger area under the curve for US/8MPa/1mm/μB as compared to C/8MPa/1mm/μB, the distribution volume difference between the two groups is not significant.

The mean dyed areas of the brain slices for each experimental group were plotted with respect to the Caudal-Rostral distance from the infusion site. The distribution volumes in general appeared to be slightly shifted towards the caudal direction, which corresponds to the rostral V_d to caudal V_d ratios having values less than 1 for all the experimental groups except C/8MPa/1mm/None (Figure 3.17).

Considering only the experiments conducted with maximum peak-to-peak acoustic pressures of approximately 8 MPa and an infusion needle–needle hydrophone distance of 2 mm, the absence or presence of microbubbles does not appear to affect the slight caudal bias of the distribution volumes (Figure 3.18). All the slices with the largest mean dyed area are also caudal to the infusion site.

Considering only the experiments conducted with maximum peak-to-peak acoustic pressures of approximately 8 MPa and an infusion needle–needle hydrophone distance of 1 mm, the absence or presence of microbubbles does not appear to affect the slight caudal bias of the distribution volumes with the exception of the no-ultrasound, no-microbubble controls, which has a slight bias towards the rostral direction (Figure 3.19). The slices with the largest mean dyed area for the ultrasound experiments are slightly caudal to the infusion site, whereas those of the control experiments are at or close to the infusion site. Despite the larger area under the curve for the ultrasound experiments as compared to that of the control experiments, both in the presence of microbubbles, the distribution volume difference between the two groups is not significant as indicated in Figure 3.14.

Considering only the experiments conducted with maximum peak-to-peak acoustic pressures of approximately 8 MPa with no microbubbles, the infusion needle–needle hydrophone distance of either 1 or 2 mm does not appear to affect the slight caudal bias of the distribution volumes with the exception of the control experiments with the 1 mm distance, which has a slight bias towards the rostral direction (Figure 3.20). The slices with the largest mean dyed area for the experimental groups are slightly caudal to the infusion site, but again with the exception of control experiments with the 1 mm distance, which has the slice with the largest mean dyed area at the infusion site.

And finally, considering only the experiments conducted with an infusion needle–needle hydrophone distance of 1 mm with microbubbles, having maximum peak-to-peak acoustic pressures of approximately 2 or 8 MPa did not appear to affect the slight bias of the distribution volumes towards the caudal direction (Figure 3.21). The slices with the largest mean dyed area for the experiments are slightly caudal to the infusion site, except for that of control experiments for the 8 MPa group, which is almost at the infusion site. As mentioned previously, despite the larger area under the curve for ultrasound experiments as compared to that of the control experiments, both for the 8 MPa group, the distribution volume difference between the two groups is not significant.

3.3.5 In Vivo Rat Experiments with 0.5 or 1 MHz Ultrasound Focused at the Site of Infusion

For the in vivo rat experiments involving the infusion of EBA with or without Targestar P microbubbles and with 0.5 MHz ultrasound focused at the site of infusion, the mean peak-to-

peak acoustic pressure used was 0.2 MPa. For the in vivo rat experiments involving the infusion of EB with or without Lumason microbubbles and with 1 MHz ultrasound focused at the site of infusion, the mean peak-to-peak acoustic pressure used was 0.3 MPa. Using TRA-focused ultrasound in both of these groups did not appear to increase the mean distribution volume of their respective dyes as compared to no-ultrasound controls (Figure 3.22). In addition, in the absence of ultrasound, the mean distribution volumes of infused EB with or without Lumason microbubbles were not significantly different. However, the mean EBA distribution volume was significantly larger than the mean EB distribution volume by a factor of two (Figure 3.23).

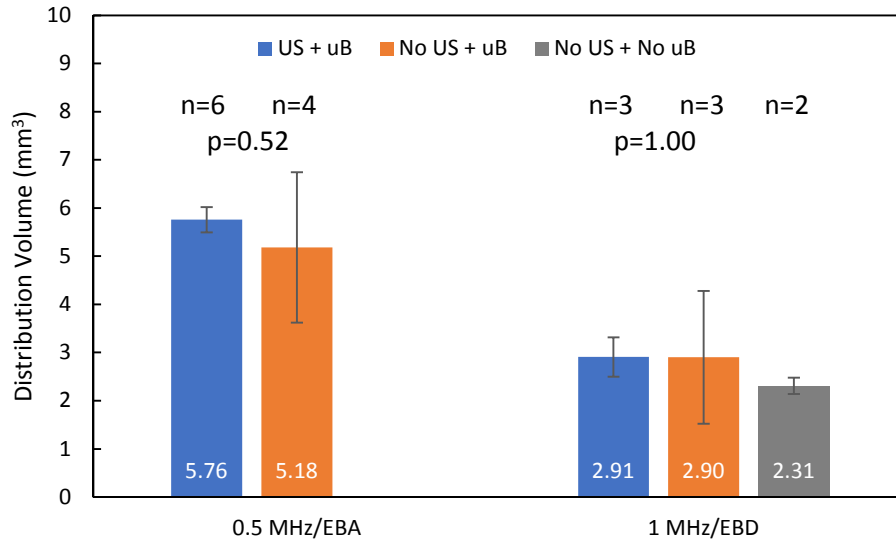


Figure 3.22: The means and standard deviations of the distribution volumes of EBA for the 0.5 MHz ultrasound + microbubbles and no-ultrasound + microbubbles groups as well as of EB for the 1 MHz ultrasound + microbubbles, no-ultrasound + microbubbles, and no-ultrasound + no-microbubbles groups are plotted. At $\alpha = 0.05$, there is no significant difference in the mean volumes of distribution among any of the groups within the 0.5 MHz/EBA and 1 MHz/EB categories.

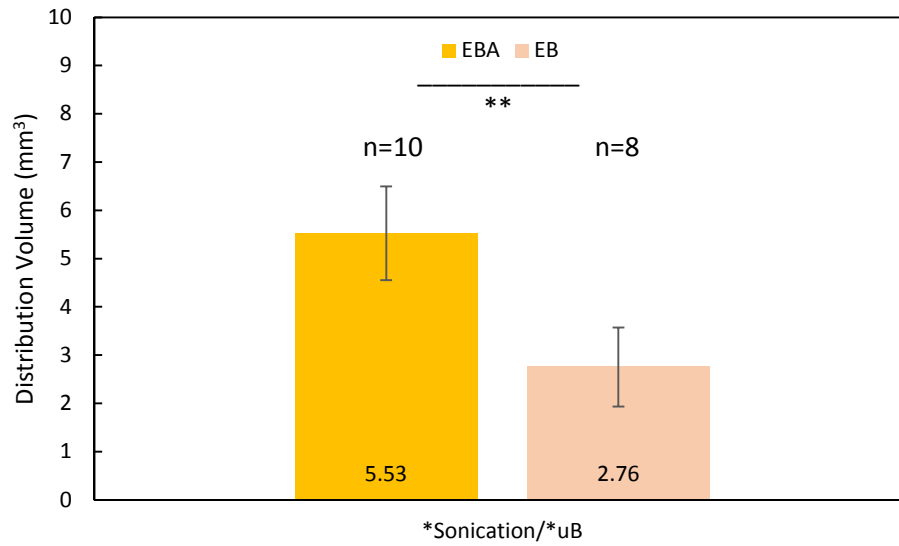


Figure 3.23: The data from Figure 3.22 re-represented as the means and standard deviations of the combined EBA and EB distribution volumes regardless of sonication or microbubbles parameters. The mean EBA distribution volume is significantly larger than the mean EB distribution volume. The ** indicates that $p < 0.01$.

3.4 Discussion

Although CED is a promising drug delivery modality for the administration of chemotherapeutic agents into the brain for the treatment of malignant brain tumors, the inability to control the spatial distribution of the drug post-infusion limits its efficacy. TRA-focused ultrasound has previously been shown to increase the distribution volume of infused tracers when it is focused at the site of infusion, especially in the presence of microbubbles, raising the possibility that it may be used to steer the drug to target locations post-infusion²³.

Our agarose gel experiment results suggest that 0.5 MHz ultrasound focused adjacent to the site of infusion using TRA does not appear to bias the distribution volume of infused EBA towards or away from the focal region. Mano et al. found that even though ultrasound emitted via the infusion needle increased the distribution volume of EB administered via CED into rodent brains, they did not observe the same effect in brain phantom gels⁶⁷. They suggested that the increase in distribution volume in rat brains may have been due to the enlargement of extracellular spaces, which are not present in gel phantoms. In our case, however, the results of our in vivo rodent experiments appear similar to those of our agarose gel experiments.

Our in vivo rodent experiment results suggest that TRA-focused 0.5 or 1 MHz ultrasound focused at the needle tip does not significantly increase the distribution volume of Evans blue or Evans blue-labeled bovine serum albumin when the dye is co-infused with Targestar P or Lumason microbubbles, respectively. Additionally, focusing ultrasound 1–2 mm adjacent to the

site of infusion did not bias the distribution of EBA towards or away from the region of focused ultrasound.

This is surprising as our results do not match our expectation that TRA-focused ultrasound would have observable effects on the distribution volumes of the infused dyes. This is especially the case for experiments in which the ultrasound was focused at the site of infusion, as our expectations were based on the results of very similar experiments conducted by Olbricht et al²³. The discrepancy may be due to differences in the needle hydrophone, TRA setup, and type of microbubbles or dye used.

3.4.1 Possible implications due to differences in the needle hydrophone

The needle hydrophone used by Olbricht et al. was sized 30G (outer diameter 0.31 mm, inner diameter 0.16 mm) and contained a piezoelectric transducer with a center resonance frequency of 1 MHz²⁴. Our custom-built needle hydrophone was 22G (outer diameter 0.72 mm, inner diameter 0.41 mm) and contained a piezoelectric transducer with a center resonance frequency of 10 MHz. 10 MHz was chosen so that the sensitivity of the hydrophone would have a flat response to the 0.5 MHz ultrasound waves emitted by our reverberator.

Because the Olbricht et al. study used 1 MHz ultrasound waves, the response of the 1 MHz hydrophone could have been large. While the acoustic pressure at the needle tip can be accounted for through careful calibration, what is less certain is how the piezoelectric transducer itself is behaving. The piezoelectric effect may have caused the 1 MHz piezoelectric transducer

to oscillate significantly at its resonance frequency and/or heat up, possibly increasing mixing or diffusivity at the needle tip. We note that Olbricht et al. did observe small hemorrhages and edema around the needle track typical of CED experiments, but that these were slightly more prevalent when microbubbles were present regardless of whether ultrasound was used.

The larger diameter of our needle may also have played a role, as a larger-diameter needle produces a smaller distribution volume than a smaller-diameter needle would, given the same flowrate⁴⁵. This may be because with a larger diameter needle, the force exerted by the infusion is distributed over a wider area, resulting in a smaller pressure gradient between the needle tip and the surrounding medium that can be used to drive the flow. Additionally, a larger-diameter infusion needle is associated with an increased risk of backflow of the tracer along the needle track^{46,74}. However, we accounted for this by not including any experiment that clearly demonstrated backflow.

3.4.2 Possible implications due to differences in the TRA setup

One other difference is the position of the infusion needle and the reverberator. Because the reverberator of our setup has a much larger interface, the reverberator had to be placed on top of the rat skull, as opposed to the side contralateral to the infusion needle, in order for it to have sufficient contact with the rat skull. This then necessitated that the infusion needle be inserted from the side of the skull as opposed to the top of the skull. While we still targeted the caudate putamen of the rat, the orientation of the infusion needle may have affected the distribution of the infused tracer.

The duty cycle used in our experiments is approximately 1%. Estimates based on peak-to-peak acoustic pressures of 0.2, 2, and 8 MPa give acoustic intensities of 0.003, 0.33, and 5.33 W/cm², respectively. This range covers the 0.01–0.04 W/cm² used in the Olbricht et al. study. The use of TRA-focused 0.5 MHz ultrasound at peak-to-peak acoustic pressures up to 2.6 MPa and a 4% duty cycle in agarose and agarose-milk gels did not result in an increase in the distribution volume of infused tracers or an increase in temperature within the ultrasound focal region, although the temperature of the reverberator did rise by about 3.5 °C over the course of an hour (data not shown).

3.4.3 Possible implications due to differences in the type of microbubbles or dye used

Based on our results, 0.5 MHz ultrasound waves focused at the tip of the infusion needle using TRA did not lead to a significant increase in the mean distribution volume of EBA co-infused with Targestar P microbubbles when compared to no-ultrasound controls. This is surprising as a very similar experiment by Olbricht et al. involving 1 MHz ultrasound waves yielded a significant increase.

However, we acknowledge that the behavior of microbubbles subjected to ultrasound is highly sensitive to the ultrasound frequency, as microbubbles may not be affected by ultrasound frequencies that are below its resonance frequency³⁸. As such, the 0.5 MHz ultrasound waves used in our study may have had little to no impact on the Targestar P microbubbles that responded so well to the 1 MHz ultrasound waves used by Olbricht et al. This in turn might explain our observed absence of a significant increase in the mean distribution volume in

sonicated rat brains that had been co-infused with EBA and microbubbles as compared to non-sonicated controls.

To determine if ultrasound frequency may be the confounding factor, we attempted to replicate this part of our study using 1 MHz ultrasound waves. Unfortunately, by the time the 1 MHz reverberator was constructed, Targeson, the manufacturer of the Targestar P microbubbles, had ceased its operations. Because the remaining experiments involved the use of the 1 MHz reverberator, we selected to use Lumason microbubbles, which have been shown to be echogenic, i.e., oscillate and backscatter, at 1 MHz^{37,38}. For added precaution, a fresh batch of Lumason microbubbles was reconstituted each day and used within three hours of reconstitution. We also chose to use 0.25% wt/vol Evans blue instead of EBA, as Olbricht et al. observed larger gains in mean distribution volumes over non-sonicated controls when EB rather than EBA was co-infused with microbubbles and sonicated.

Despite pairing the Lumason microbubbles with our 1 MHz reverberator, our results showed no significant difference in the mean EB distribution volumes between the sonicated and non-sonicated groups. In addition, in the absence of ultrasound, the addition of Lumason microbubbles did not result in any significant difference in the mean EB distribution volume as compared to when no microbubbles were added. This again is surprising as Olbricht et al. had found that the addition of microbubbles alone was sufficient to increase the distribution volume of infused tracers by a factor of about 3. Indeed, when we look at our data from non-sonicated experiments, the addition of Targestar P microbubbles to EBA did not significantly increase the mean distribution volume of EBA compared to when no Targestar P microbubbles were added

(Figure 3.16). However, the mean EBA distribution volume was significantly larger than the mean EB distribution volume by a factor of two. Because the hydrodynamic radii of EB and EBA are approximately 1.3 nm and 5.0 nm, respectively, this goes against the prediction that smaller tracers can penetrate deeper into the tissues due to less hindrance from the interstitium^{23,75}.

Systemically-administered Evans blue has commonly been used as a marker of blood-brain barrier integrity, as it binds strongly and rapidly to serum albumin, which is too large to cross the blood-brain barrier. However, it is unclear if Evans blue itself can pass the blood-brain barrier⁷⁶. As such, one possible explanation may be that the smaller EB dye molecules are cleared more quickly from the brain than the larger EBA molecules, thus resulting in smaller EB distribution volumes. In addition, even in the presence of albumin, EB has been shown to bind strongly to tissue⁷⁶. Therefore, another possible explanation could be that EB is binding strongly to the brain tissue near the infusion site, thus preventing it from penetrating further into the brain.

The results from our two sets of in vivo rodent brain experiments suggest that co-infusing tracers with microbubbles does not significantly increase the distribution volumes of the infused tracers, regardless of the presence or absence of TRA-focused ultrasound. This is actually in line with the findings of Lewis et al., where they did not observe an increase in dye distribution volume based solely on the addition of Targestar P microbubbles²⁵. In fact, they found that the addition of Targestar P microbubbles greatly diminished the enhancement of the dye distribution volume that resulted from using non-focused ultrasound²⁵.

Recent upper estimates of the pore size of the brain extracellular space (ECS) based on the diffusion of quantum dots or heavily PEGylated nanoparticles range from 38–64 nm to over 100 nm, respectively^{39,40}. Because the mean diameters of the Targestar P and Lumason microbubbles are 2.2 and 2.5 μm , respectively, we suspect that most of the microbubbles would aggregate around the needle tip as opposed to infiltrating the ECS of the brain. Heavily PEGylated nanoparticles with diameters up to 114 nm were able to easily penetrate the brain ECS⁴⁰, but these microbubbles have diameters that are an order of magnitude larger^{37,77}, and the level of PEGylation is uncertain. While these microbubbles may be able to change shape in order to move through the brain ECS, it is unlikely that they can shrink their diameters by an order of magnitude while remaining intact. Lewis et al. suggested that the aggregation of microbubbles around the tip of the infusion needle may interfere with and limit the effects of the ultrasound. Wang et al. circumvented this issue through the systemic administration of microbubbles and applying focused ultrasound prior to the infusion.

In the next chapter, we see that TRA-focused ultrasound focused at the site of infusion can increase the distribution volume of infused tracers in the absence of microbubbles.

3.5 Conclusion

TRA-focused ultrasound sonicated at or adjacent to the site of CED infusion in agarose gels and in vivo in rodent brains did not appear to expand or shape the distribution volumes of the infused tracers. In particular, when the tracers were co-infused with phospholipid-encapsulated microbubbles into rodent brains in vivo, neither the addition of the microbubbles alone nor the

use of TRA-focused ultrasound to sonicate the site of infusion appeared to increase the distribution volumes of the infused tracers. However, the EBA distribution volumes were significantly larger than the EB distribution volumes, suggesting that the infused EB may be prevented from penetrating more deeply into the brain tissue.

CHAPTER 4

THE EFFECT OF TIME-REVERSAL ACOUSTICS FOCUSED ULTRASOUND ON THE DISTRIBUTION OF CONVECTION-ENHANCED DELIVERED DYE AND POLYSTYRENE NANOPARTICLES IN RAT BRAINS

4.1 Introduction

Glioblastoma multiforme is a devastating malignant brain tumor with poor treatment options despite the increasing number of chemotherapeutic agents that have been developed¹⁻⁴. One complicating factor is the presence of the blood-brain barrier, which comprises endothelial cells with tight junctions that only allow very small (< 400 Da) lipophilic drugs to passively diffuse from the bloodstream into brain tissue⁴². Even for drugs that are able to cross the blood-brain barrier, they still have to be systemically delivered in high doses for sufficiently long durations in order for the drugs to enter the brain tissue at therapeutic concentrations, resulting in toxic side effects.

One promising drug delivery modality that would widen the array of possible drugs that can be used to treat brain diseases is convection-enhanced delivery (CED)^{10,11}. This method infuses the drugs directly into the diseased brain tissue through a needle or cannula, thereby eliminating the restrictions posed by the blood-brain barrier as well as limiting the side effects associated with the systemic delivery of drugs. In addition, the pressure gradient generated by the infusion

pushes the drugs farther into the tissue at larger concentrations and for longer durations as compared to pure diffusion alone¹⁰.

However, advanced clinical trials have had disappointing results^{13–15}. A retrospective analysis of the Phase III PRECISE trial found insufficient distribution of cintredekin besudotox, a cytotoxin that specifically targets gliomas, even within the 2 cm penumbra of the tumor site¹³. While the authors suggested that better catheter placement may improve the efficacy of CED, other strategies have emerged that can further enhance CED.

One possible strategy is to enhance the distribution volume of the infused tracers through the pre-infusion or concurrent use of either non-focused or focused ultrasound^{22,23,25,41}. In particular, Olbricht et al. have demonstrated that using time-reversal acoustics (TRA) to focus ultrasound at the site of infusion during CED can significantly increase the distribution volume of infused tracers compared to CED alone²³.

Another possible strategy is to slow down the rate of clearance of the infused drug by packaging it into nanoparticles^{78–80}. Once the drug has been infused into the brain tissue, it is subjected to clearance mechanisms such as degradation or phagocytosis¹¹. By packaging the drug into nanoparticles, the rate at which the drug is cleared from the brain tissue can be significantly reduced. Chemotherapeutic drugs such as cisplatin⁸¹, camptothecin⁸², and irinotecan⁸⁰ have already been loaded into nanoparticles for in vivo studies in animal models. In addition, nanoparticles carrying one drug can be co-infused with a different drug to enhance the overall therapeutic effect of the treatment. For example, nanoparticles attached to both O^6 -

benzylguanine and the tumor-targeting peptide chlorotoxin have been co-infused with temozolomide to reduce the resistance of glioblastoma multiforme to the latter, thereby maintaining the chemotherapeutic effect of temozolomide for longer durations⁸³.

Based on the promising results of using focused ultrasound to enhance CED and loading nanoparticles with drugs for controlled drug delivery, we were interested in the potential for combining them together, i.e., whether focused ultrasound can increase the distribution of nanoparticles and/or a lower molecular weight dye when they are co-infused. For this study, our objective is to determine whether TRA-focused ultrasound can be used to increase the distribution of 20-nm and 40-nm polystyrene nanoparticles that have been co-infused with Evans blue-labeled bovine serum albumin (EBA).

4.2 Materials and Methods

4.2.1 Preparation of Tracers

5% wt/vol Evans blue-labeled bovine serum albumin (EBA) was prepared by adding 1X PBS (Sigma #P3813) to a mixture of 0.25 g of bovine serum albumin (BSA) (Sigma #B4287-5G) and 0.022g of Evans blue to a total volume of 5 mL. The dyes were then filtered using a syringe filter with a 0.2 µm nylon membrane (PALL #4433). The 5% wt/vol EBA was divided into 100 µL aliquots and frozen at -20 °C for storage, and thawed and vortexed just prior to use.

Stock solutions of 20 and 40-nm carboxylate-modified red fluorescent polystyrene particles (Life Technologies #F8786 and #F8793, respectively) were first sonicated for 15 minutes, and then diluted to 0.1% wt/vol solids in a solution of 1% wt/vol BSA in 1X PBS to reduce the surface charge of the particles. These nanoparticle solutions were next shielded from light and immersed in a cold-water bath on a laboratory rocker for 4 hours, and then stored in a refrigerator at 4 °C.

The size of the EBA, and the sizes and ζ -potentials of the BSA-coated 20-nm and 40-nm polystyrene particles were determined using the ZetaSizer Nano (Malvern Instruments) and shown in Table 4.1.

Table 4.1: The mean diameters and ζ -potentials of the EBA and the BSA-coated nanoparticles.

Particle	Mean Diameter (nm)	SD (nm)	Mean Polydispersity Index	Mean ζ -potential (mV)	SD (mV)
20-nm + BSA	47.0	1.9	0.174	-12.1	0.61
40-nm + BSA ⁸⁴	75.4	0.5	0.121	-11.0	0.35
EBA	10.1	1.1	0.434	-	-

4.2.2 Animal Surgery and Experiment

Male albino Sprague Dawley rats weighing between 254 and 374 g were anesthetized using 2–2.5% isoflurane. A heating pad was used to maintain the body temperature of the rat during the experiment. A burr hole was drilled into the right side of the rodent skull to allow an infusion needle with the hydrophone embedded at the tip to be inserted laterally into the brain at a position 0.7 mm anterior, 2.9 mm lateral, and 5.4 mm inferior to bregma; this position coincides with the middle of the caudate putamen⁷⁰. Ultrasound transmission gel was applied on the front face of the reverberator, which was then positioned on top of the rodent skull. Just prior to inserting the needle into the rodent brain, the needle was primed with a freshly mixed solution of 5% wt/vol EBA and either the 0.1% wt/vol 20-nm or 40-nm polystyrene particle solution in a 1:1 ratio. After needle insertion, the TRA-CED system was set up to focus 0.5 MHz ultrasound at the tip of the infusion needle. For Ultrasound experiments, the focused ultrasound and the infusion pump were turned on simultaneously. For the no-ultrasound Control experiments, only the infusion pump was turned on at the start of the experiment. These experimental parameters are summarized in Table 4.2.

While the total duration of each experiment was 30 minutes, the dye mixture was infused at a flowrate of 0.2 $\mu\text{L}/\text{min}$ for only 2.5 minutes for a total infusion volume of 0.5 μL . This means that each experiment was convection-dominated for the first 2.5 minutes and diffusion-dominated for the last 27.5 minutes.

At the end of the experiments, the rats were euthanized with a lethal dose of pentobarbital. The rats were then perfused transcardially with at least three times the blood volume of 1X PBS, followed by 4% paraformaldehyde. The rodent brains were then extracted and soaked in 4% paraformaldehyde overnight. This surgical procedure was performed in accordance with Cornell University's Institutional Animal Care and Use Committee regulations.

4.2.3 Imaging and Image Analysis

After overnight fixation of the rat brains in 4% paraformaldehyde at 4°C, the rat brains were then immersed through a series of 30% and 60% sucrose solutions before being embedded in OCT and frozen. The regions of the rat brains containing EBA were then sliced in 50- μ m-thick coronal sections using a cryotome. Reflectance images of the 50- μ m-thick coronal sections were taken using a microscope camera (Veho #VMS-004) and the recording software VideoVelocity (CandyLabs). Images of a ruler were obtained to determine the scale of the images. In addition, every fifth brain slice was saved and mounted onto slides for imaging using fluorescence microscopy.

4.2.4 Assessing the distribution of EBA using the Reflectance Images

The reflectance images were processed and analyzed using Fiji⁷¹ and Matlab. The images from each rat brain was converted into a single stack. The RGB image stack was deconvolved⁷³ to extract only the blue color of the Evans blue dye, resulting in an 8-bit image stack. The slice containing the infusion needle tip was selected, and the hemisphere of the brain contralateral to

the infusion site was used to determine the mean grey value and the standard deviation of the background. The 8-bit image stack was then converted to a binary image stack using a minimum threshold that was set at 8 standard deviations above the mean grey value of the background—any pixel with a value above the threshold was considered to represent a dyed region.

Matlab was then used to calculate the total number of dye pixels for each slice as well as for each image stack. The scale for each stack and the slice interval of 50 μm were then used to convert the pixel data into the dyed area of each brain slice and the total dye distribution volume (V_d) of each image stack.

Experiments that showed evidence of backflow were excluded from the analysis. In addition, one experiment that had a V_d/V_i ratio less than 1 was also excluded from the analysis. The mean distribution volume for each experimental group was then determined.

Table 4.2: Summary of TRA-focused ultrasound and no-ultrasound CED experimental parameters conducted in vivo in rodent brains. There are four different groups in total.

Mean Pk-Pk Acoustic Pressure (MPa)	Diameter of nanoparticles in 1% BSA co-infused with 5% EBA in a 1:1 ratio	Treatment	Sample Size
0.1 – 0.2	20-nm	Ultrasound	6
		No Ultrasound	4
	40-nm	Ultrasound	3
		No Ultrasound	3

4.2.5 Assessing the concentration profiles of EBA using the Reflectance Images

In CED, the distribution of the tracer in the rat brain are due to diffusion (mass transport due to Brownian motion down a concentration gradient) and convection (mass transport due to bulk flow of fluid down a pressure gradient).

To assess whether TRA-focused ultrasound is enhancing diffusion or convection when the EBA+20-nm polystyrene particles were co-infused via CED into the rat brain, we obtained intensity line profiles from the reflectance images by selecting vertical rectangular regions 4000 μm long and 100 μm wide across the center of the EBA distribution area in coronal slices of the rat brains (Figure 4.1 A), and then taking the median values along the width. The images analyzed for each rat were of the brain slice containing the needle tip as well as five slices before and after it, corresponding to -250 μm to +250 μm from the needle tip. In each of those images, vertical line profiles were obtained in 50 μm increments ranging from -250 μm to +250 μm about the center of infusion in each image. In addition, the background intensity for each image was determined as the median intensity of a 1550 μm -by-1160 μm rectangular region (corresponding to 1% of total image area) in the brain hemisphere contralateral to the dye-infused region.

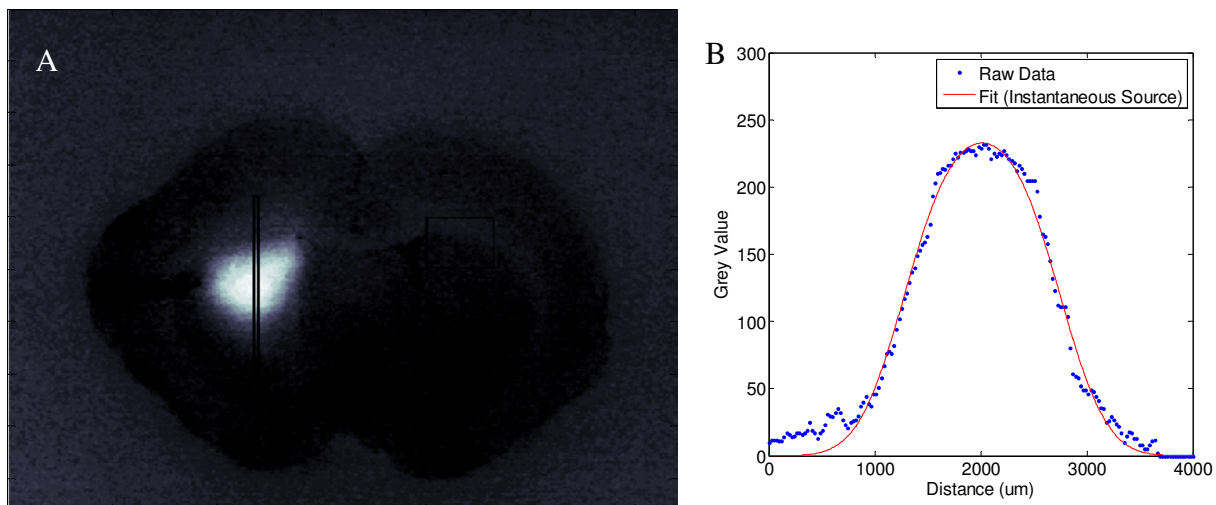


Figure 4.1: A) A 4000 μm -by-100 μm vertical rectangle was drawn across the EBA distribution area in one coronal slice of a rat brain. B) The median pixel values were obtained across the 100 μm width, and the intensity line profile is plotted. The data was then fitted to a model of diffusion from an instantaneous spherical source of constant concentration.

After the median background intensity was subtracted from each line profile, the line profiles were then fitted to the following model of diffusion from an instantaneous spherical source of constant concentration⁶⁰ (Figure 4.1 B):

$$c = \frac{1}{2} c_0 \left(\operatorname{erf} \frac{a + \sqrt{x^2 + y^2 + z^2}}{2\sqrt{D^*t}} + \operatorname{erf} \frac{a - \sqrt{x^2 + y^2 + z^2}}{2\sqrt{D^*t}} \right) - \frac{c_0}{\sqrt{x^2 + y^2 + z^2}} \sqrt{\frac{D^*t}{\pi}} \left[e^{-\left(\frac{a - \sqrt{x^2 + y^2 + z^2}}{2\sqrt{D^*t}}\right)^2} - e^{-\left(\frac{a + \sqrt{x^2 + y^2 + z^2}}{2\sqrt{D^*t}}\right)^2} \right]$$

Equation 4.1: Diffusion from an instantaneous spherical source of constant concentration, where c_0 is the initial dye concentration, a is the radius of the central sphere of constant concentration, D^* is the apparent diffusivity of the dye in the rat caudate putamen, and t is the duration of the diffusion phase of the experiment.

In this model, a and D^* would provide insight into the convective and diffusive components of the experiment, respectively. The lower limits, starting values, and upper limits for the parameters used in fitting the line profile data obtained from the reflectance images to the diffusion model are listed in Table 4.3. We estimated the starting point for a by considering an infusion of dye at a flowrate of 0.2 $\mu\text{L}/\text{min}$ for 2.5 minutes into a medium with porosity of 0.2, which is typical of brain tissue⁵³, and a resulting distribution volume that is spherical and of constant concentration. This spherical distribution volume would thus have a radius of 842 μm , which we use as our starting point for a . We set the lower limit of t as 1650 seconds, i.e., 27.5 minutes, since that is the duration of the experiment during which there is no infusion. We

assumed that after the rat was euthanized and the rat brain was perfused with and fixed in 4% paraformaldehyde, any subsequent diffusion of EBA was negligible.

The parameters that provided the optimal fits were recorded, and the mean a and D^* values were then calculated for each rat and for each experimental group.

Table 4.3: The lower limits, starting values, and upper limits for the parameters used in fitting the line profile data obtained from the reflectance images to the diffusion model.

Parameter	Lower Limit	Start Point	Upper Limit
D^* ($\mu\text{m}^2/\text{s}$)	1	30	500
a (μm)	500	842	1000
c_0 (grey value)	200	250	255
t (s)	1650 (i.e., 27.5 min)	1650	3600

4.2.6 Assessing the distribution of EBA and 20-nm and 40-nm polystyrene particles using Fluorescence Microscopy

Because Evans blue and the 20-nm and 40-nm polystyrene particles are fluorescent, we were able to use fluorescence microscopy to determine their distribution.

Since the rat brains were sliced into 50- μm sections and every fifth slice was saved and mounted on slides, we had brain slices that were 250 μm apart. The brain slices were viewed using a one-photon Zeiss Axio Examiner D1 microscope with a 2.5X objective. An inverted 0.5X lens was placed before a QICAM FAST Cooled Mono 12-bit camera (QICAM #32-0090B-334) to increase its field of view, so that the entire fluorescent region in each slice could be imaged in one frame. The images were taken using three filter settings—Bright Field, TxR and TRITC. Under the TRITC filter, only the 20-nm or 40-nm red polystyrene particles were visible (Figure 4.5 B and D). Under the TxR filter, both the red nanoparticles and EBA were visible (Figure 4.5 A and C). The exposure times for the TxR and TRITC channels were set to maximize the intensity ranges of the image based on a sampling of central brain slices. These settings were then applied uniformly across all brain sections.

Because the EBA had a larger distribution volume compared to the nanoparticles, we were able to obtain another measure of EBA distribution volume by thresholding the TxR images. Using a threshold of 2.5% of global maximum intensity among all the TxR images, the area of EBA distribution of each slice was obtained. This area was then multiplied by the 250- μm interval between slices to obtain a volume. These volumes were then summed to obtain the distribution

volume of EBA for each rat. To obtain the distribution volumes of the nanoparticles, the same protocol was applied to the TRITC images, but using a threshold of 10% of global maximum intensity.

4.2.7 Statistical Analysis

Two-tailed t-tests assuming unequal variances and a significance level of 0.05 were performed on the null hypotheses that there are no significant differences in the mean distribution volumes of EBA and the 20-nm or 40-nm polystyrene particles between the Ultrasound and no-ultrasound Control experiments for both the EBA+20-nm and EBA+40-nm groups. In addition, these t-tests were also performed on the D^* and α parameters derived from fitting the EBA concentration line profiles to the diffusion model with the null hypotheses being that there are no significant differences in the means values between the Ultrasound and no-ultrasound Control experiments for both the EBA+20-nm and EBA+40-nm groups.

4.3 Results

4.3.1 Assessing the mean distribution volumes and V_d/V_i ratios of EBA from the Reflectance Images

The mean peak-to-peak acoustic pressures used in the ultrasound experiments for the 20-nm and 40-nm groups were 0.189 and 0.102 MPa, respectively. Focusing 0.5 MHz ultrasound at the tip

of the infusion needle led to an increase in the EBA distribution volume (Figure 4.2 B) and the V_d/V_i ratio (Figure 4.2 C) only when EBA was co-infused with 20-nm particles.

The mean dyed areas of the brain slices for each experimental group were plotted with respect to the Caudal-Rostral distance from the infusion site (Figure 4.3). The spread of the mean distribution volumes of each experimental group has a slight bias towards the caudal direction. This bias was also seen in Chapter 3 when EBA was co-infused with microbubbles. The slices with the largest mean dyed area for the experimental groups are slightly caudal to the infusion site, although that of Control-40-nm is very close to the infusion site. For the 20-nm experiments, the larger area under the curve for the Ultrasound experiments as compared to that of the Control experiments corresponds to the significantly larger distribution volume for the former as compared to the latter.

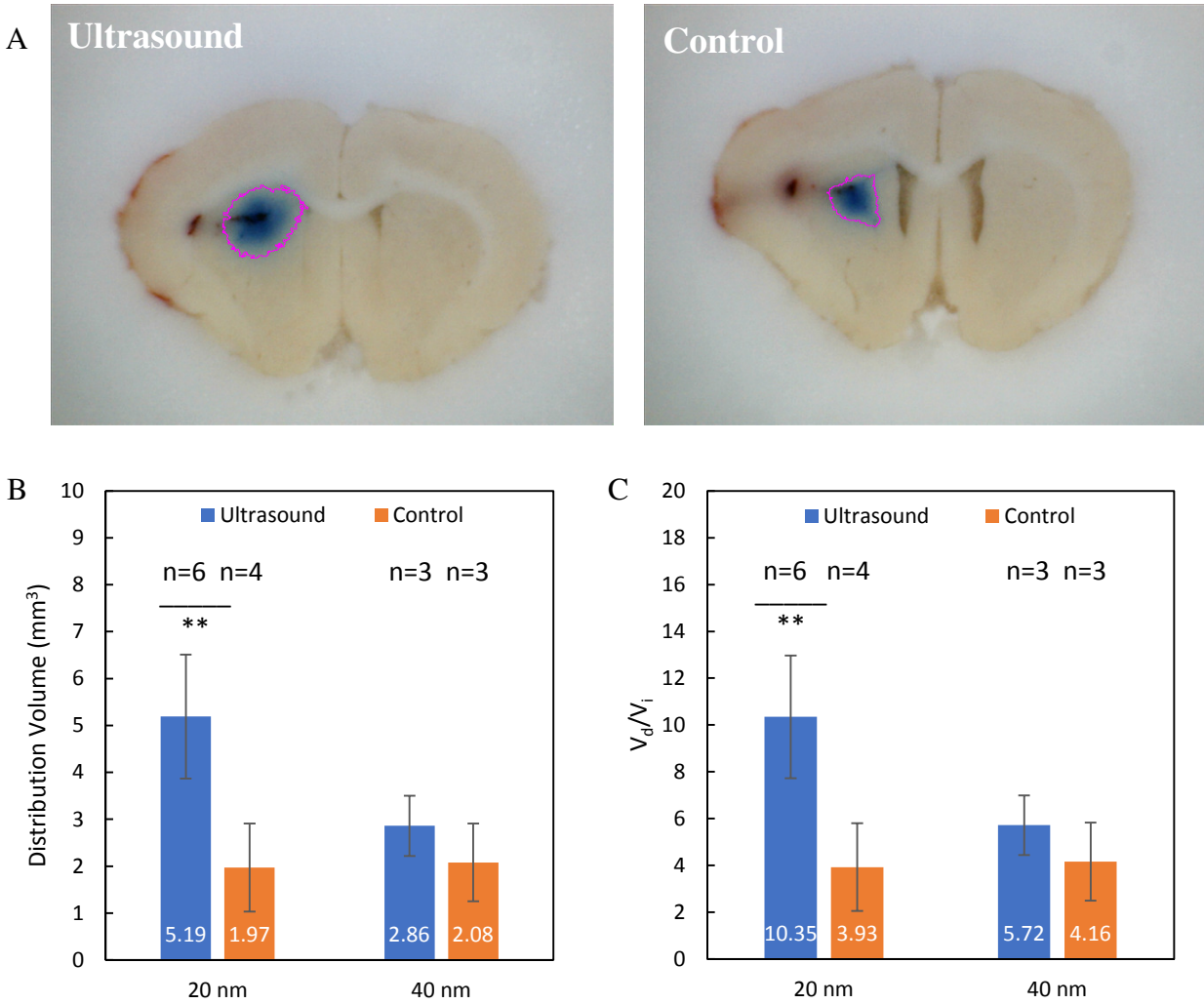


Figure 4.2: A shows the EBA-dyed areas in representative brain sections containing the tip of the infusion needle/hydrophone for the Ultrasound and no-ultrasound Control experiments for the EBA+20-nm group. The magenta lines indicate the borders of the dyed areas as determined by the threshold. B and C show the means and standard deviations of the distribution volumes of EBA and the V_d/V_i ratios, respectively, for Ultrasound and no-ultrasound Control experiments for both the EBA+20-nm and EBA+40-nm groups. At $\alpha = 0.05$, the mean EBA distribution volume of the Ultrasound experiments was larger than that of Control experiments only for the EBA+20-nm group. The ** indicates that $p < 0.01$.

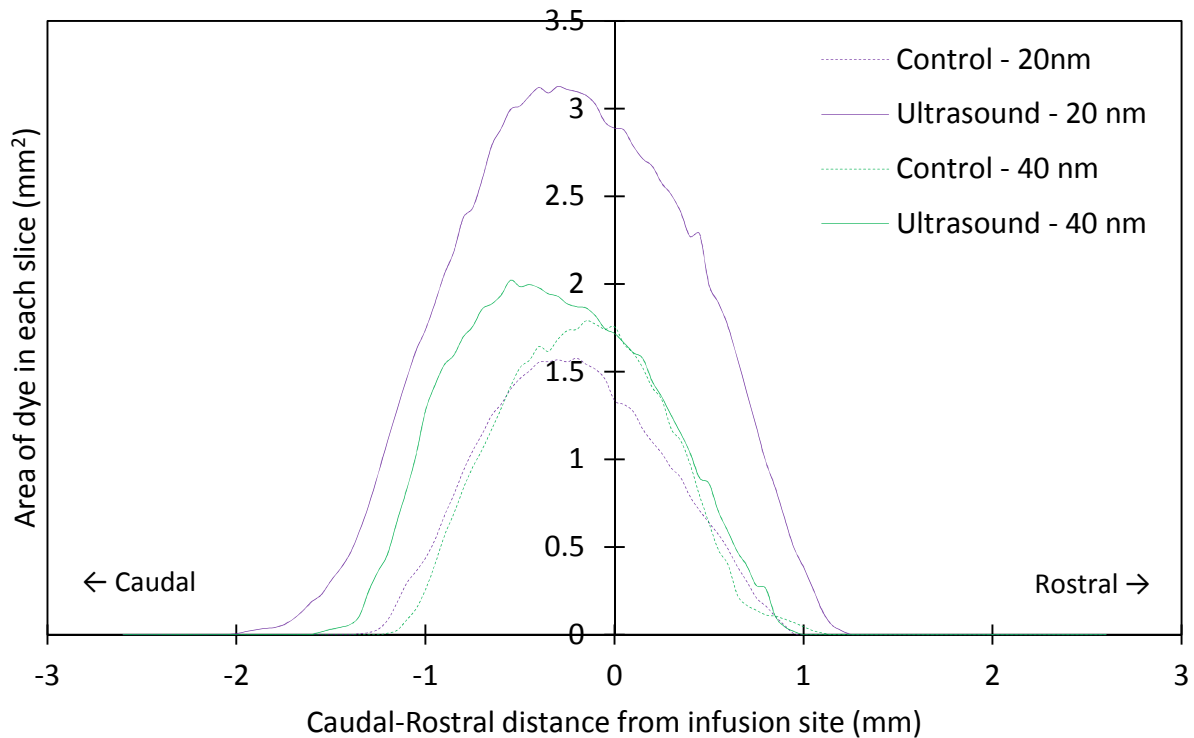


Figure 4.3: The mean EBA-dyed areas of the brain slices for each experimental group were plotted with respect to the Caudal-Rostral distance from the infusion site. The distribution volumes of all the experimental groups have a slight bias towards the caudal direction. The slices with the largest mean dyed area for the experimental groups are slightly caudal to the infusion site, although that of Control-40-nm is very close to the infusion site. For the 20-nm experiments, the larger area under the curve for the Ultrasound experiments as compared to the Control experiments corresponds to the significantly larger distribution volume for the former as compared to the latter.

4.3.2 Assessing the concentration profiles of EBA from the Reflectance Images

The mean D^* value (Figure 4.4A) for each experimental group obtained by fitting the line concentration profiles of EBA from the reflectance images to the diffusion model was close to the $17.5 \mu\text{m}^2/\text{s}$ reported in the literature for bovine serum albumin at 37°C in the rat brain⁸⁵.

There was no significant difference in mean D^* values between ultrasound and no-ultrasound experiments for both EBA+20-nm and EBA+40-nm. The mean α values (Figure 4.4B) obtained from the fitting were 7.5–34.0 % lower than the estimated starting point of $842 \mu\text{m}$ (Table 4.3). Interestingly, the mean value of α for the EBA+20-nm ultrasound group was significantly larger than that of the EBA+20-nm control group. This result suggests that ultrasound improved the distribution volume of EBA for the EBA+20-nm experiments by enhancing convection rather than diffusion. The mean t value across all experimental groups was $1665 \pm 12 \text{ s}$. This mean value is 15 seconds longer than the 25.7-minute diffusion duration of the experiments.

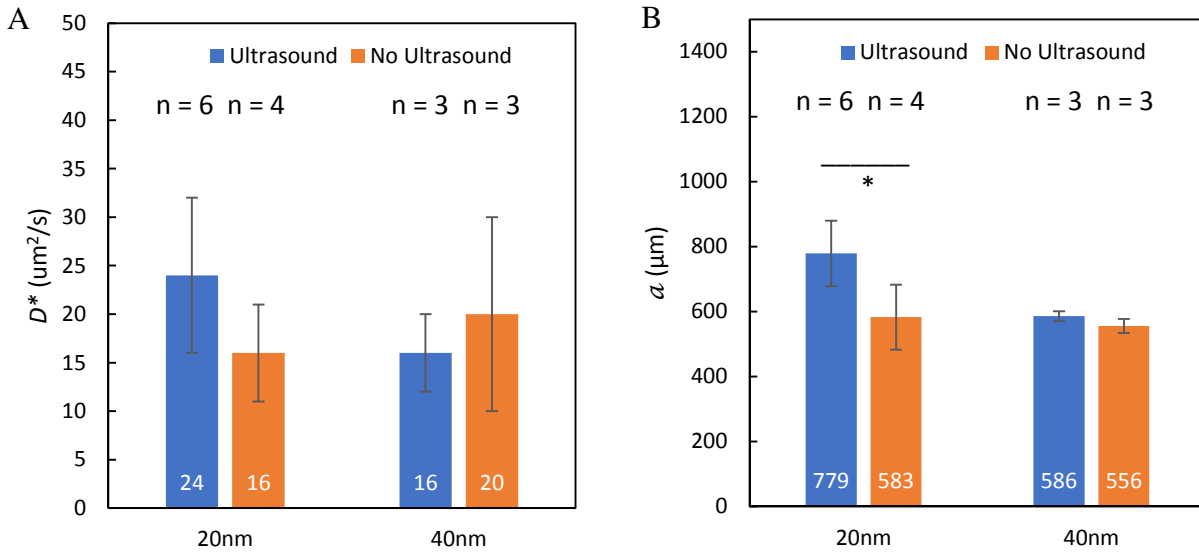


Figure 4.4: A and B show the means and standard deviations of D^* and a , respectively, for Ultrasound and no-ultrasound Control experiments involving co-infusions of EBA with either 20 or 40-nm polystyrene particles. At $\alpha = 0.05$, there was no significant difference in mean D^* values between ultrasound and no-ultrasound experiments for both EBA+20-nm and EBA+40-nm, whereas the mean value of a for the ultrasound group was significantly larger than that of the control group only for EBA+20-nm. The * indicates that $p < 0.05$.

4.3.3 Assessing the mean distribution volumes of EBA and the 20-nm and 40-nm polystyrene particles using Fluorescence Microscopy

We observed in the fluorescent images circular or oval regions of lower fluorescence intensity that we suspect are due to axon bundles (Figure 4.5). Another interesting observation is that the 40-nm polystyrene particles appear to aggregate around the axon bundles as opposed to distributing more evenly throughout the surrounding gray matter (Figure 4.5 C, D). These will be explored further in Chapter 5.

The fluorescent data show a significant increase in the mean EBA distribution volume when ultrasound is applied to the EBA+20-nm co-infusion as compared to when not using ultrasound (Figure 4.6). Even though the fluorescent data is based on brain slices 250 μm apart as compared to 50 μm apart for the reflectance data, the fluorescent data validates the results from the reflectance data (corresponding data from Figure 4.2 replicated as striped bars in Figure 4.6).

Despite the significant difference in mean EBA distribution volumes between the ultrasound and no-ultrasound groups for the EBA+20nm co-infusion experiments, there is no significant difference between the mean distribution volumes of the 20-nm polystyrene particles themselves (Figure 4.7). This analysis may benefit from having smaller intervals between the brain slices, since the mean distribution volumes of these nanoparticles are much smaller than those of EBA.

We also observed that the mean distribution volumes of the 40-nm polystyrene particles are significantly less than those of the 20-nm polystyrene particles.

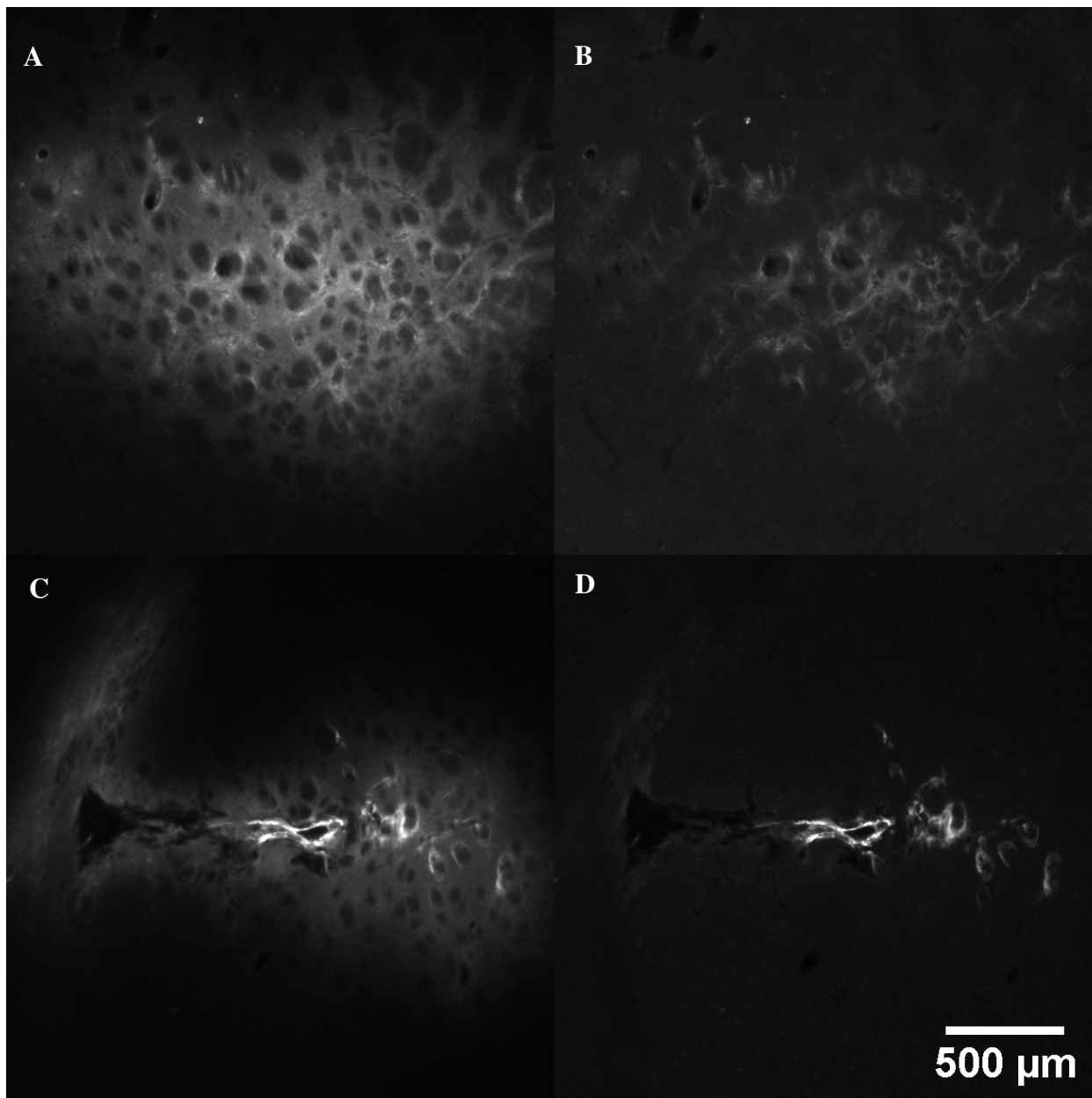


Figure 4.5: A and C are example fluorescent images taken in the TxR channel, displaying the fluorescence from the 20-nm and 40-nm polystyrene particles, respectively, in addition to the EBA. B and D are example fluorescent images taken in the TRITC channel, displaying the fluorescence from the 20-nm and 40-nm polystyrene particles, respectively.

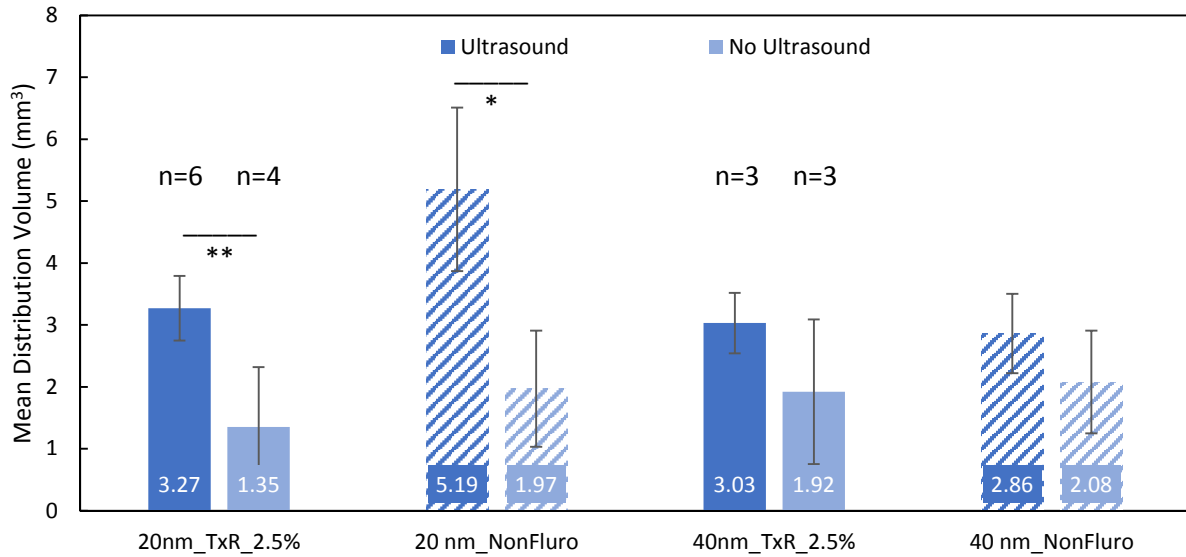


Figure 4.6: The means and standard deviations of the EBA distribution volumes of the Ultrasound and no-ultrasound Control experiments involving co-infusions of EBA with either 20 or 40-nm polystyrene particles. The solid and striped bars represent distribution volumes calculated from the fluorescent and reflectance images, respectively. The fluorescent data validates the results from the reflectance data, showing a significant increase in the mean EBA distribution volume when ultrasound is applied to the EBA+20-nm co-infusion as compared to no ultrasound. The * and ** indicate that $p < 0.01$ and <0.05 , respectively.

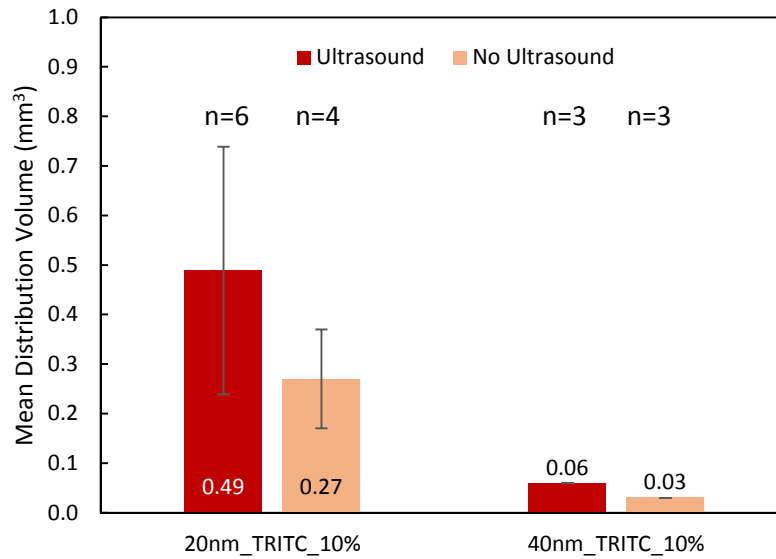


Figure 4.7: The means and standard deviations of nanoparticle distribution volumes of the Ultrasound and no-ultrasound Control experiments involving co-infusions of EBA with either 20 or 40-nm polystyrene particles. At $\alpha = 0.05$, there are no significant differences between the mean distribution volumes of Ultrasound and no-ultrasound Control experiments in both the 20 and 40-nm groups.

4.4 Discussion

Although CED is a promising modality to deliver chemotherapeutic drugs directly to the brain for the treatment of malignant brain tumors like glioblastoma multiforme, poor drug distribution remains a problem as evidenced by poor outcomes of advanced clinical trials¹³⁻¹⁵. Pairing TRA-focused ultrasound with CED to increase the distribution volume of the infused drug and using nanoparticles as drug carriers to reduce the rate of clearance of the drug from the brain has the potential to improve the efficacy of CED.

Our results suggest that using TRA to focus 0.5 MHz ultrasound at the site of infusion significantly increased the distribution volume of EBA when it was co-infused with 20-nm, but not 40-nm, polystyrene particles. While the former result is in line with the findings of Olbricht et al.²³, the latter result suggests that the presence of the 40-nm polystyrene particles impeded the enhancing effect of ultrasound on the distribution of EBA.

In addition, while TRA-focused 0.5 MHz ultrasound did not significantly increase the distribution volumes of both the 20-nm and 40-nm polystyrene particles, the mean distribution volume of the 20-nm polystyrene particles of the ultrasound experiments was still almost double that of the no-ultrasound experiments. We also observed that the mean distribution volumes of the 40-nm polystyrene particles are significantly less than those of the 20-nm polystyrene particles.

When comparing the two EBA-nanoparticle mixtures, the only difference between them was the size of the nanoparticles used, i.e., the difference was about a factor of two. As such, it is interesting that TRA-focused ultrasound would lead to a significant increase in EBA distribution when the dye is co-infused with nanoparticles of one size but not the other.

One possible factor is that the hydrodynamic diameter of the BSA-coated 40-nm polystyrene particles is close to or larger than the estimated pore size of the brain extracellular space (ECS). Recent upper estimates of the pore size of the brain ECS range from 38–64 nm to over 100 nm, based on the diffusion of quantum dots or heavily PEGylated nanoparticles, respectively^{39,40}. With its size being so close to the upper limit of the ECS pore size as well as the lack of heavy PEGylation, it is possible that the 40-nm polystyrene particles (actual diameter of 75.4 ± 0.5 nm) are much more hindered within the ECS as compared to the 20-nm polystyrene particles (actual diameter of 47.0 ± 1.9 nm) (Table 4.1). Moreover, the 40-nm polystyrene particles would have greater potential to either partially or fully clog some of the pores in the ECS, thereby possibly limiting any ultrasound enhancement in the distribution of EBA as well.

The results derived from fitting EBA concentration line profiles to the model of diffusion from an instantaneous spherical source may provide some insight into how TRA-focused ultrasound enhanced the distribution volume of EBA when it was co-infused with 20-nm polystyrene particles. The mean value of a , but not D^* , for the EBA+20-nm ultrasound group was significantly larger than that of the EBA+20-nm control group. Because a represents the radius of the instantaneous spherical source resulting from 2.5 minutes of convection while D^* represents the apparent diffusivity of EBA in the caudate putamen of the rodent brain, these

results suggest that TRA-focused ultrasound improved the distribution volume of EBA for the EBA+20-nm experiments by enhancing convection rather than diffusion.

This result, however, does not rule out enhancement of diffusion by focused ultrasound. Wang et al.⁴¹ sonicated the caudate putamen of mice using a combination of focused ultrasound (center frequency = 1.5 MHz, peak-rarefactional pressure = 0.72 MPa) and systemically-administered microbubbles to “permeabilize” the brain region prior to infusing 0.8 μ L of gadolinium-labeled albumin at a flowrate of 0.18 μ L/min. Post-infusion, the mean distribution volume of the gadolinium-labeled albumin in the sonicated mice became significantly larger than that of the non-sonicated mice only after 120 minutes, but not after 30 minutes. In our study, we used TRA-focused ultrasound (center frequency = 0.5 MHz, peak-rarefactional pressure = 0.051 – 0.0945 MPa) with no systemically-administered microbubbles. The much lower peak-rarefactional pressure used and the absence of microbubbles in our experiments make it possible that the sonication did not increase intercellular permeability or disrupt the blood-brain barrier, mechanisms which Wang et al. postulated led to the enhancement of diffusion in their study⁴¹. Alternatively, the post-infusion duration of 27.5 minutes in our experiments may have not been long enough for any increase in the distribution volume of EBA from the enhancement of diffusion to be significant.

On the other hand, Liu et al. sonicated the left corona radiata of a cynomolgus monkey using non-focused ultrasound (center frequency = 1 MHz, acoustic pressure = 1.24 MPa) after infusions of 30–50 μ L of gadoteridol-containing nanoliposomes at a maximum flowrate of 3 μ L/min into both hemispheres²². Interestingly, they did not observe a significant effect of

ultrasound when the left corona radiata was sonicated with the flowrate maintained at 3 $\mu\text{L}/\text{min}$, but did so when the flowrate of 0.1 $\mu\text{L}/\text{min}$ was used simply to maintain positive pressure. While the authors suggested that the increase in tracer distribution volume resulting from sonication was due to increased permeability of the brain tissue, we cannot rule out the possibility that ultrasound can enhance convection when lower flowrates are used.

4.4.1 Limitations of the model of diffusion from an instantaneous spherical source of constant concentration

We note that the mean a values (Figure 4.4B) obtained from fitting EBA concentration line profiles to the model of diffusion from an instantaneous spherical source of constant concentration were 7.5–34.0% lower than the estimated starting point of 842 μm (Table 4.3). While this may be partially due to the caudate putamen of these rats having a porosity value higher than the general estimated brain porosity of 0.2, a larger porosity alone cannot fully account for these differences as the porosity value required to account for the largest difference would be close to 1.

As such, we must examine several assumptions that were made in the model when interpreting the results from the fitting. First, the model assumes that the brain tissue is a homogenous medium. Although the brain region targeted in these experiments, i.e., the caudate putamen, is relatively homogeneous and isotropic grey matter, it does contain white matter fibers and blood vessels that can hinder the path of the infused tracers. Second, the model assumes that the distribution volume of EBA administered via CED for 2.5 minutes is a perfect sphere, which is

unlikely the case in the rodent caudate putamen. As such, taking line profiles in a single dimension may underestimate the value of a if the distribution volume was spread wider in other dimensions. We attempted to account for this by taking vertical line profiles not just at the site of infusion but also in 50- μm increments between and including -250 μm to +250 μm horizontally from the needle tip across the middle 11 brain slices, which are also spaced 50 μm apart. Third, the model does not account for clearance mechanisms, especially during the 27.5-minute diffusive phase of the experiment. In future work, we would need to use a more complex model to take all this into account, such as through tortuosity and clearance factors. Despite this, we believe that since this model was applied uniformly across all rats, the trends in the results should hold.

4.5 Conclusion

We used TRA-focused 0.5 MHz ultrasound to sonicate the site of infusion to determine whether doing so increases the distribution volume of CED-administered 5% wt/vol EBA mixed with either 0.1% wt/vol 20 or 40-nm polystyrene particles in 1% wt/vol BSA. Our results show that TRA-focused ultrasound increased the distribution volume of EBA that was co-infused with 20-nm, but not 40-nm, polystyrene particles. In addition, results from fitting EBA concentration line profiles to a model of diffusion from an instantaneous spherical source of constant concentration suggest that this significant increase in EBA distribution volume is due to TRA-focused ultrasound enhancing convection rather than diffusion.

CHAPTER 5

ASSESSING THE DISTRIBUTION OF EVANS BLUE-LABELED BOVINE SERUM ALBUMIN INFUSED VIA CONVECTION-ENHANCED DELIVERY INTO THE RAT CAUDATE PUTAMEN

5.1 Introduction

As described in earlier chapters, convection-enhanced delivery (CED) is a promising method of delivering therapeutic drugs into the brain with sufficient distribution volumes and at therapeutic concentrations^{10,86}. However, advanced clinical trials involving CED to treat patients with brain cancers have produced disappointing results, with insufficient distribution of the chemotherapeutic drug within 2 cm of the resection cavity as a possible factor^{13,15,16}.

One parameter that researchers often use to determine the efficacy of CED is the volume of distribution (V_d). Regardless of the imaging modality, e.g., magnetic resonance imaging (MRI), fluorescence microscopy, or autoradiography, the volume of distribution is usually determined by using an intensity threshold that is either a percentage of the maximum measured intensity or several standard deviations above the mean or median intensity of the background noise^{10,23,86-89}.

However, in our CED rodent experiments that use fluorescence microscopy, we have observed that the distribution of infused substances is highly variable across the caudate putamen, a region

that is often used as the site of infusion because it appears to be a homogeneous region of gray matter⁸⁶. This non-uniform distribution presents as circular or oval regions of lower intensity, with diameters ranging approximately from 20 to 100 μm , widely spread throughout the distribution volume of the tracer. This non-uniform distribution has also been observed in other CED rodent studies using fluorescence microscopy, but disappear as a result of thresholding or is ignored^{87,88,90}.

Because the recurrence of malignant brain tumors often occurs within two centimeters of the original tumor site despite aggressive treatment¹⁶, it is important to understand how drug concentration can vary even within seemingly homogeneous gray matter. Neeves et al. suggested that these lower intensity regions observed may be striosomes, which are neurochemically distinct regions within the striatum⁸⁷. However, the circular or oval shapes of these lower intensity regions do not appear similar to the more arbitrarily shaped striosomal regions documented in the literature⁹¹⁻⁹³. Another possibility is that these regions are axon fascicles or bundles⁹⁴⁻⁹⁶, as white matter tracts have been shown to have reduced apparent diffusivity transverse to the myelinated axon tracts as compared to along the myelinated axon tracts or within isotropic gray matter⁹⁷.

The aim of this study is to identify the brain structures that result in non-uniform distribution of substances administered via CED in the rodent caudate putamen.

5.2 Materials and Methods

5.2.1 Animal Surgery and Infusion

Three male Sprague-Dawley rats, each weighing between 400 and 450 g, were anesthetized using 2–2.5% isoflurane. A heating pad was used to maintain the body temperature of the rat during the experiment. A burr hole was drilled into the right side of the rodent skull to allow an infusion needle to be inserted laterally into the brain at a position 0.7 mm anterior, 2.9 mm lateral, and 5.4 mm inferior to bregma, which coincides with the middle of the caudate putamen. 5% Evans blue–labeled bovine serum albumin (EBA) (MW = ~66 kDa) was then infused at a flowrate of 0.2 $\mu\text{L}/\text{min}$ for about 2.5 minutes. The rats were then euthanized through the administration of a lethal dose of pentobarbital. The rats were then perfused transcardially with at least three times the blood volume of 1X PBS, followed by 4% paraformaldehyde. The brains were then extracted and soaked in 4% paraformaldehyde overnight. This surgical procedure was performed in accordance with Cornell University's Institutional Animal Care and Use Committee regulations.

5.2.2 Histochemical Staining

After overnight fixation of the rat brains in 4% paraformaldehyde at 4°C, the rat brains were then immersed through a series of 30% and 60% sucrose solutions before being embedded in OCT and frozen. The regions of the rat brains containing EBA were then sliced in 50- μm -thick coronal sections using a cryotome and mounted onto slides.

From each rat, fifteen sequential brain slices at or near the site of infusion were selected. These brain slices were stained with a 1:300 dilution of Hoechst 33342 (Invitrogen H3570) and 1X Fluoromyelin Green Fluorescent Myelin Stain (Invitrogen F34651) to visualize cell nuclei and myelin, respectively. Additionally, five sequential brain slices from one rat was stained with Hoechst 33342 but not with Fluoromyelin to serve as a Fluoromyelin-negative control.

All the stained slides were then mounted with glass cover slips and ProLong Diamond Antifade Mountant (Life Technologies P36961).

5.2.3 Imaging and Image Analysis

The stained brain slices were imaged using a fluorescent microscope (Zeiss 710 AxioObserver) with a 10x objective and a 12-bit camera using the following settings: Red Channel: Evans blue (Laser: 561 nm / Detection Range: 566–689 nm), Green Channel: Fluoromyelin (488 nm / 491–627 nm), and Blue Channel: Hoechst 33342 (405 nm / 410–495 nm). Each brain slice thus had three 12-bit images, one for each channel. Each 12-bit image was 1024px-by-1024px or 1.42mm-by-1.42mm (scale 1.38 $\mu\text{m}/\text{px}$). The rigid image registration technique of the Register Virtual Stack Slices plugin in Fiji⁷¹ was used to align the images of the brain slices from each rat.

To analyze both the Evans blue and Fluoromyelin images, a 3px-by-3px median filter was applied to each image to remove outlier intensity values. Five 100px-by-100px regions from each image were selected such that they contained at least one circular or oval region with Evans blue fluorescence intensity lower than its surroundings. The Evans blue and Fluoromyelin

fluorescence intensities inside and outside each circular or oval region were measured, and in/out intensity ratios for both Evans blue and Fluoromyelin were calculated for each rat. This same analysis was performed on the Fluoromyelin-negative control brain slices.

5.2.4 Statistical Analysis

The Evans blue and Fluoromyelin in/out intensity ratios for each rat are reported as the means and standard deviations of 75 data points across 15 brain slices. For the Fluoromyelin-negative control brain slices, the Evans blue and Fluoromyelin in/out intensity ratios are reported as the means and standard deviations of 25 data points across 5 brain slices. A one-way analysis of variance (ANOVA) was used to determine significant differences among in/out ratios for both Evans blue and Fluoromyelin for the three rats. Two-tailed t-tests assuming unequal variances were used to determine whether there were significant differences between the in/out ratios for both Evans blue and Fluoromyelin for the rat with Fluoromyelin-positive and negative brain slices.

5.3 Results

5.3.1 Co-localization of low Evans blue intensity circular and oval regions with high Fluoromyelin intensity regions

Overlaying the Evans blue, Fluoromyelin, and Hoechst images for rat brain slices stained with Fluoromyelin and Hoechst (Figure 5.1), it becomes apparent that the circular and oval regions of

low Evans blue fluorescence intensity were also regions of high Fluoromyelin fluorescence intensity. Additionally, these circular and oval regions qualitatively appear to be much less densely populated with nuclei as compared to outside the regions.

For the rat brain slices stained with Hoechst but not with Fluoromyelin (Figure 5.2), the green channel shows some background and brain autofluorescence^{98,99}. Interestingly, the circular and oval regions now are lower in fluorescence intensity than the surrounding tissue, similar to the pattern of Evans blue fluorescence intensity in the red channel.

We also noticed that in the green channel of Fluoromyelin-positive brain slices, the intensity on average decreased as one moves towards the middle of the image (Figure 5.1B), but this was not evident in the green channel of the Fluoromyelin-negative brain slices (Figure 5.2B).

In addition to the circular or oval regions of lower Evans blue fluorescence intensity corresponding to regions positive for myelin, we were able to track certain regions across the different brain slices (Figure 5.3), which were taken in 50- μ m intervals, further suggesting that these regions are myelinated axon fascicles or bundles traveling through the rat caudate putamen.

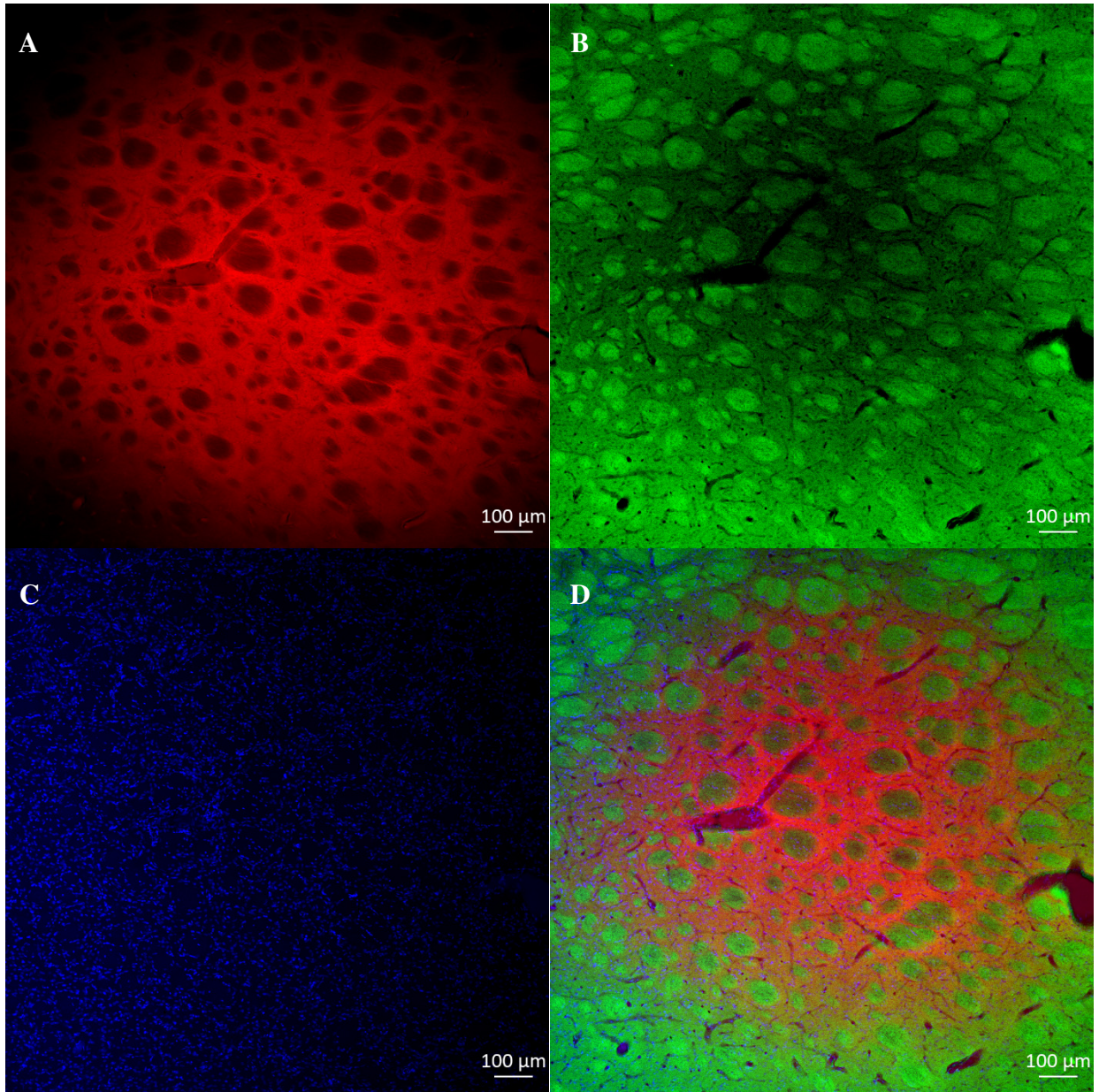


Figure 5.1: Fluorescent images of the rat caudate putamen showing (A) Evans blue, (B) Fluoromyelin, (C) Hoechst, and (D) composite of all three channels. The regions of low Evans blue fluorescence correspond with regions of high Fluoromyelin fluorescence.

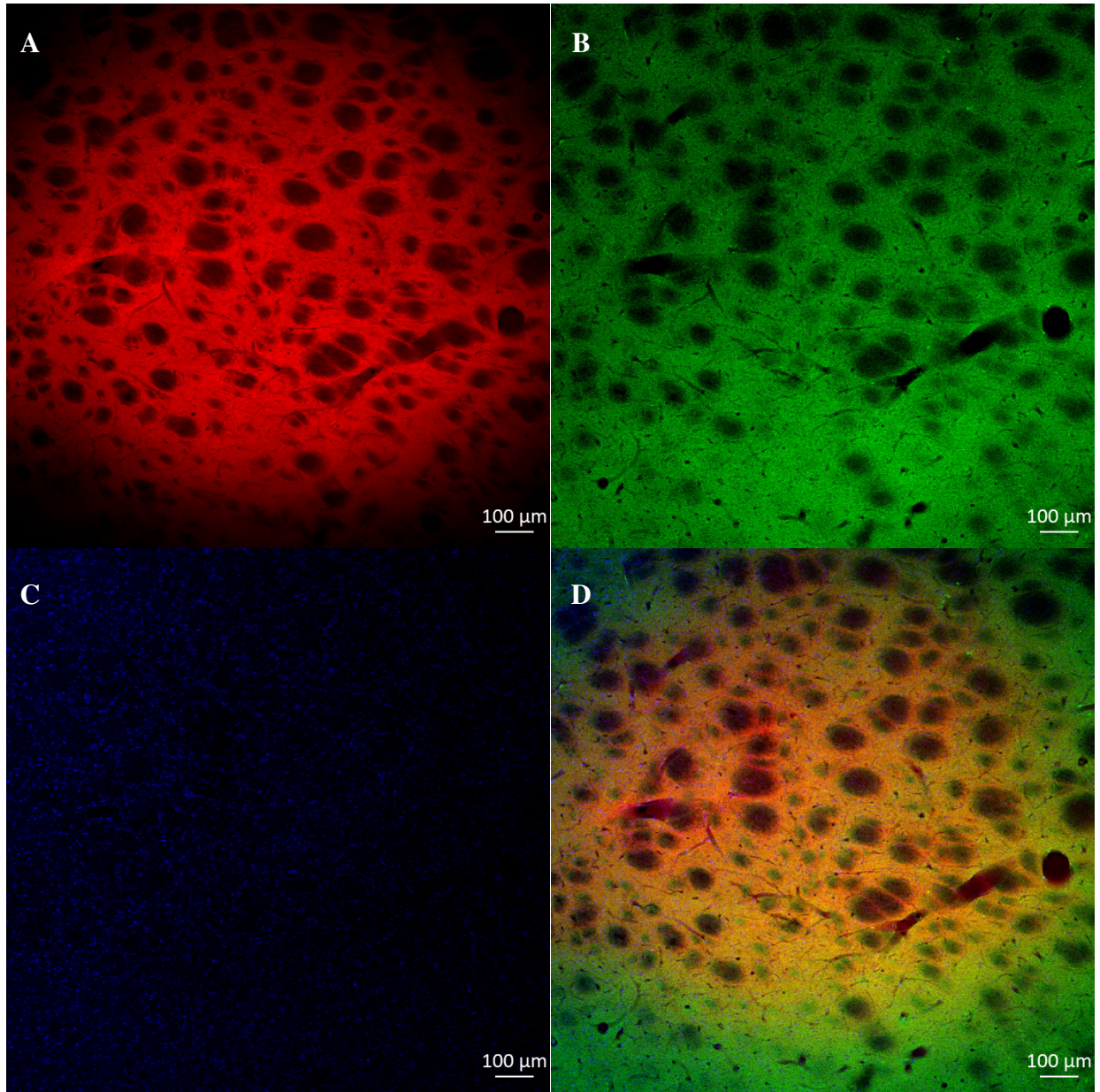


Figure 5.2: Fluorescent images of a Fluoromyelin-negative control rat caudate putamen showing (A) Evans blue, (B) Fluoromyelin, (C) Hoechst, and (D) composite of all three channels. In the absence of Fluoromyelin, the green channel displays autofluorescence from the brain tissue, with the circular or oval regions of lower Evans blue fluorescence intensity in the red channel

corresponding to regions of lower green autofluorescence compared to the surrounding gray matter in the green channel.

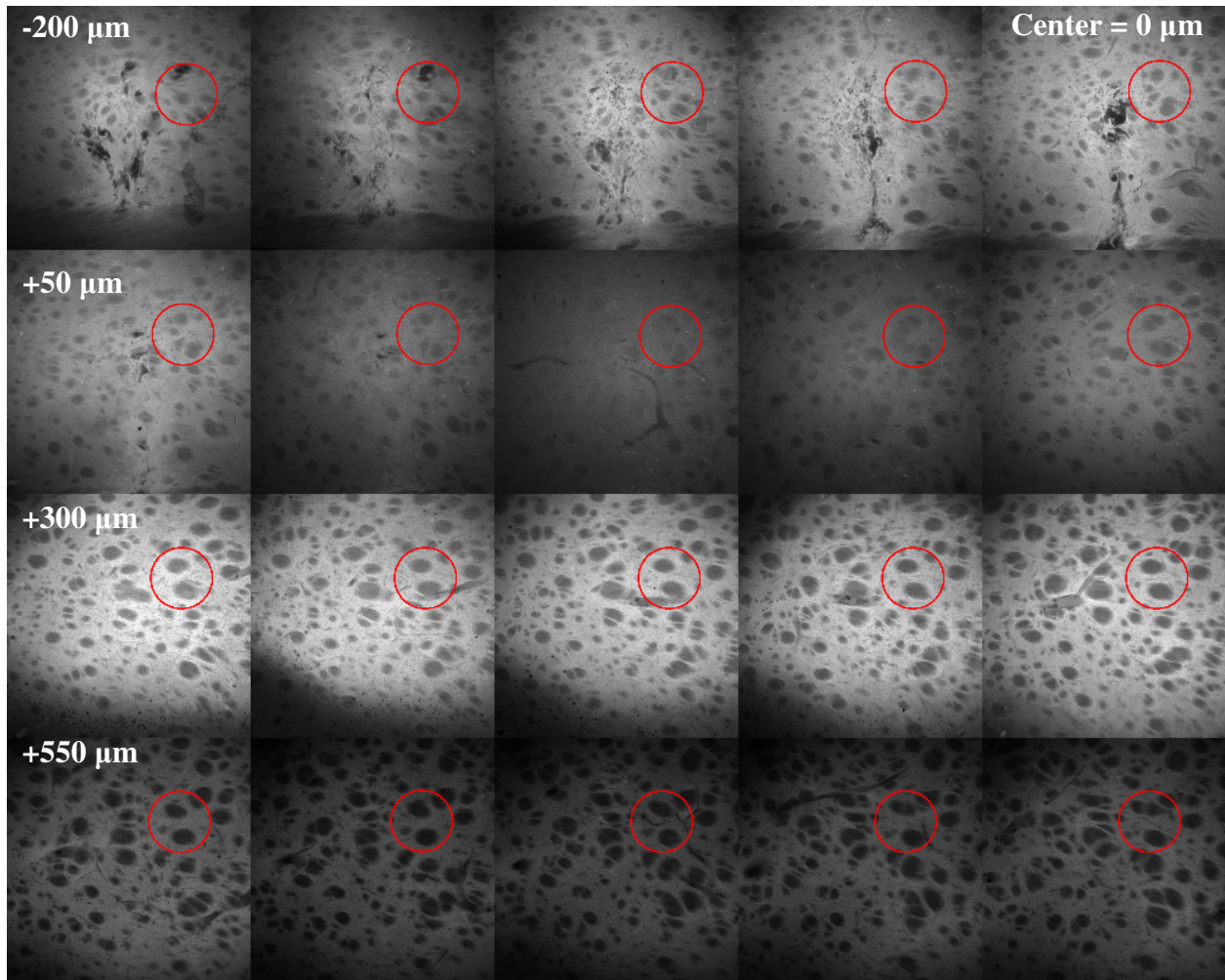


Figure 5.3: The aligned images from the Evans blue channel of a single rat. Red circle: A group of axon bundles can be tracked across all the slices (1 mm total).

5.3.2 Comparison of Evans blue fluorescence intensity within and outside the axon bundle

The overall means and standard deviations (excluding the Fluoromyelin-negative brain slices) of the Evans blue and Fluoromyelin In/Out fluorescence intensity ratios are 0.67 ± 0.087 and 1.24 ± 0.063 , respectively. At a significance level of 5%, all Evans blue ratios are significantly different from each other, while all Fluoromyelin ratios except between Rat 2 and Rat 3 are significantly different from each other. It is interesting that the Evans blue ratios differ across the rats observed (Figure 5.4A) despite adhering to the same imaging protocol. Slight duration differences in euthanasia, immersion in PFA and sucrose solutions, and exposure to light during cryosectioning, staining, and imaging may aggregate sufficiently to result in this observation.

However, it is clear that the presence of Fluoromyelin increases the mean Evans blue In/Out intensity ratio (Figure 5.4A: Rat 3 vs Rat 3–no FM). This is because there is a slight overlap in the excitation and emission spectra of Fluoromyelin with the imaging settings used to capture the Evans blue fluorescence. As such, a small amount of fluorescence from the Fluoromyelin stain may be bleeding through into the Evans blue channel, raising the detected fluorescence intensity within the axon bundle. In the absence of Fluoromyelin, we would expect the Evans blue In/Out fluorescence intensity ratios measured to be lower than 0.67.

Because fluorescence intensity is approximately linearly proportional to the concentration of the tracer¹⁰⁰, our results suggest that the concentration of EBA within the axon bundles is on average at least about 67% of the concentration outside them.

Additionally, the Fluoromyelin In/Out fluorescence intensity ratios for Fluoromyelin-positive rat brain slices are greater than 1, while that of Fluoromyelin-negative rat brain slices are less than 1 (Figure 5.4B).

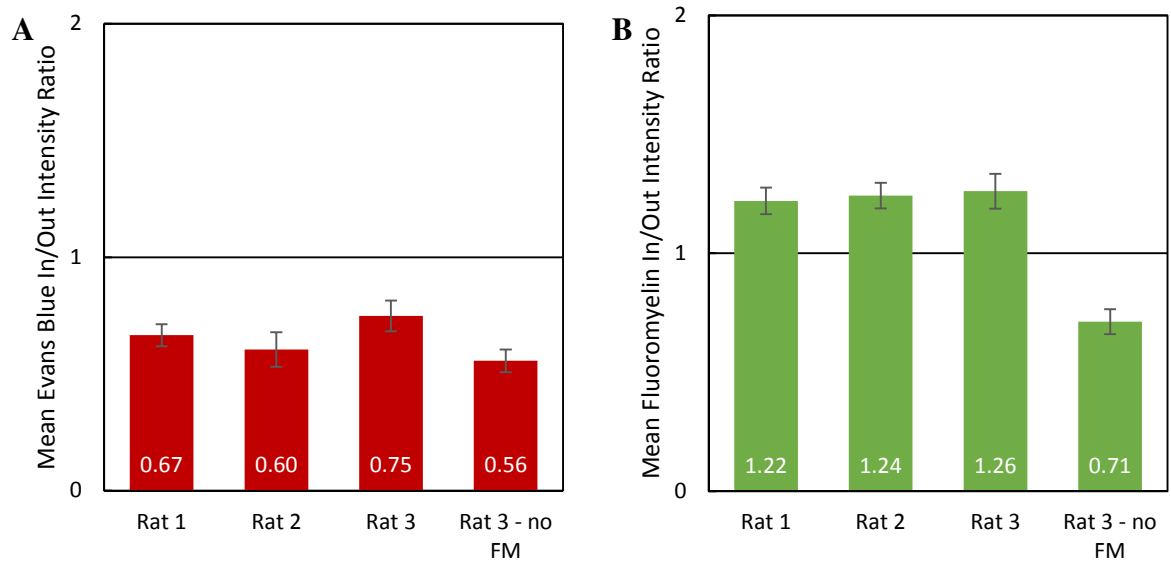


Figure 5.4: The means and standard deviations of the Evans blue (A) and Fluoromyelin (B) In/Out fluorescence intensity ratios for each rat (75 samples per rat) as well as the Fluoromyelin-negative brain slices (25 samples). The lower the ratio, the greater the difference in fluorescence intensity inside and outside of the axon bundle. At a significance level of 5%, all Evans blue ratios are significantly different from each other ($p < 0.01$), while all Fluoromyelin ratios, except between Rat 2 and Rat 3 ($p = 0.08$), are significantly different from each other ($p < 0.01$).

5.4 Discussion

While CED is a promising means of drug delivery for the treatment of brain diseases, advanced clinical trials of CED have had disappointing results so far^{13–15}. One possible reason is the insufficient distribution of chemotherapeutic agents within the volume of distribution, which could be due to improper catheter placement, reflux of infusate along the needle track, and rapid clearance or leakage of infusate^{8,13}

Our results suggest that even within seemingly homogenous tissue like the caudate putamen of rats, the distribution of substances administered via CED may not be uniform. Here, we demonstrate that infusions of Evans blue–labeled bovine serum albumin into the caudate putamen of rat brains do not result in uniform distribution of the tracer due to the presence of axon fascicles. Because fluorescence intensity is approximately linearly proportional to the concentration of the tracer¹⁰⁰, our results suggest that the concentration of Evans blue–labeled albumin within an axon fascicle is on average 67% of the concentration outside it.

We note that the non-uniform distribution of tracers administered via CED appears to be obvious when imaging is performed using fluorescence microscopy, but not with PET or MRI imaging^{81,101–103}. The likely reason is that the resolution of these techniques when used in CED studies is insufficient to detect the difference in tracer concentration inside and outside these small axon bundles.

The presence of axon fascicles within the rat caudate putamen or in the striatum of primates is clearly not a novel finding^{96,104}. There have been several studies that have infused substances within specific brain nuclei in order to achieve anterograde or retrograde transport. For example, Lieberman et al. were able to infuse wheat germ agglutinin labeled with horse radish peroxidase into the rat striatum to access the substantia nigra pars compacta via the oculomotor nerve using retrograde transport⁸⁶. Ciesielska et al. infused adeno-associated virus (AAV) vectors expressing glial cell line-derived neurotrophic factors (GDNF) into the rat striatum and accessed the nigro-striatum using only anterograde transport¹⁰⁵. In non-human primates, Yazdan-Shahmorad et al. infused AAV vectors co-expressing channelrhodopsin-2 (ChR2) and yellow fluorescent protein (YFP) into the thalamus to access the cerebral cortex using thalamo-cortico-thalamic circuits¹⁰⁶.

However, less attention has been paid to the possibility that these axons bundles are being missed in CED studies, either through reduced access or rapid clearance via white matter transport, despite being within the volume of distribution. For example, Ksendzovsky et al. did not detect any axonal transport when infusing non-spherical, 900-nm-long M13 bacteriophage into the thalamus of non-human primates¹⁰⁷.

In our previous chapter, we noted that the 20-nm and especially the 40-nm polystyrene particles were also at least partially excluded from the axon fascicles to the extent that they aggregated in higher concentrations around these axon fascicles in the rat caudate putamen. This behavior appears to occur even when brain-penetrating nanoparticles, e.g., nanoparticles that have been heavily PEGylated, are used⁹⁰.

We also observed that in coronal brain slices distal to the site of infusion, the 20-nm and especially the 40-nm polystyrene particles appear to aggregate around these axon fascicles but are otherwise almost absent in the surrounding gray matter. Possible explanations for this behavior are that the nanoparticles either are being pushed along the axon fascicles or are traveling in between the gray and white matter interface due to the increased tortuosity in directions transverse to the axon fascicles as compared to the axial direction⁹⁷. Another possibility may be that the bovine serum albumin coating on the nanoparticles are causing them to bind to the lipid-rich white matter tracts, since bovine serum albumin can bind to lipids both specifically and non-specifically¹⁰⁸⁻¹¹⁰.

Because gliomas have been shown to invade the brain parenchyma preferentially through myelinated axon tracts^{3,111,112}, it is important to account for the non-uniform distribution of chemotherapeutic drugs administered via CED. Doing so would ensure that the drug concentration throughout the volume of distribution remains at therapeutic levels for sufficient durations, potentially improving the efficacy of CED.

5.5 Conclusion

CED is a promising means of bypassing the blood-brain barrier to deliver therapeutic drugs to the brain, but advanced CED clinical trials have had disappointing results so far¹³⁻¹⁵. We show that, within the volume of distribution, the concentration of Evans blue-labeled bovine serum albumin administered via CED into the rodent caudate putamen is not uniform, with the concentration inside axon fascicles being on average 67% of the concentration in the surrounding

gray matter. This result suggests that it would be useful to account for the non-uniform distribution of chemotherapeutic drugs administered via CED to ensure that therapeutic concentrations are achieved and maintained during treatment.

CHAPTER 6

EVALUATION OF RADIALY-EMITTED ULTRASOUND ON THE DISTRIBUTION OF EVANS BLUE DYE ADMINISTERED VIA CONVECTION-ENHANCED DELIVERY IN A MILK-AGAROSE BRAIN PHANTOM

6.1 Introduction

As discussed earlier in Chapters 1 and 2, ultrasound has been used to increase the transport of infused tracers in tissues^{22,57}. Low % wt/vol agarose gels are used extensively in convection-enhanced delivery (CED) experiments as a substitute for brain tissue. In addition, ultrasound has been shown to increase the penetration of molecules into agarose gels⁵⁷ and the internal diffusivity of agarose gels¹¹³. Other studies have shown that ultrasound increases the release of molecules embedded within a variety of hydrogels¹¹⁴.

When developing tissue phantoms for ultrasound, parameters such as the speed of sound, acoustic impedance, and attenuation need to be considered. The attenuation coefficient for brain tissue is approximately 0.6 dB/cm MHz, whereas that of low % wt/vol agarose gels is very close to that of water, i.e., 0.0022 dB/cm MHz. Evaporated milk has been used to increase the attenuation coefficient of tissue phantoms¹¹⁵, including those made from agarose¹¹⁶.

The ultrasound experiments described in this dissertation so far involve the use of time-reversal acoustic (TRA) principles to focus ultrasound at the site of CED infusion. With TRA, the ultrasound source is externally applied²⁴, e.g., to the skull surrounding the brain or the container holding the agarose gel.

Here, we explore how ultrasound that is radially-emitted from the tip of the infusion catheter impacts the distribution of 1% wt/vol Evans blue (MW = 960) in a milk-agarose gel phantom. While radially-emitted ultrasound did not increase the distribution volume of the infused dye in agarose, we were interested to know if using a low % wt/vol agarose made with 50% evaporated milk and 50% water would result in greater distribution of the infused tracer.

The increased attenuation coefficient of ultrasound from adding evaporated milk should result in a steeper pressure gradient, as shown by the following equation¹¹⁷:

$$P_x = P_0 e^{-2\alpha x}$$

Equation 6.1: where P_x is the pressure at x , P_0 is the initial pressure, and α is the attenuation coefficient.

This is not unlike the flow of a fluid due to a pressure gradient that is the basis of CED.

6.2 Materials and Methods

6.2.1 Ultrasonic catheter

The ultrasonic catheter used was an Ekos MicroSonic SV Endovascular catheter (EKOS #300-30160), which is an FDA approved catheter that allows for the combination of ultrasound and infused thrombolytic drugs to break up blood clots in the vasculature.

The outer diameter of the catheter tip was 1.00 mm, and the piezoelectric element had an internal diameter of 0.43 mm. The stated power was 0.45 W. We measured the central frequency, duty cycle, and acoustic pressure using a calibrated hydrophone (Onda HNC-0200).

The ultrasonic catheter has a safety setting that does not allow the ultrasound to be switched on when the temperature of the catheter tip is less than 32°C. This is to prevent the catheter from being switched on when it is outside the vasculature. It also automatically turns off the ultrasound when the temperature at the tip is more than 43°C so as not to cause thermal damage to the patient. These settings present some challenges that we will address later.

6.2.2 Infusions into milk-agarose gel

Evaporated milk (Nestle Carnation) was used to increase the attenuation coefficient of agarose gels. We made 0.2% wt/vol agarose gels using 50% milk and 50% reverse osmosis deionized (RODI) water, making sure not to boil the mixture to prevent the milk from curdling. Because of hysteresis, the milk-agarose phantom solidified at temperatures slightly above 32°C, but only melted at temperatures closer to the boiling point of water.

The milk-gel was poured into a 22mm*22mm*20mm disposable embedding mold (Polyscience #18646A), and the mold was placed in a water bath with a mini hotplate/stirrer (VWR #33918-603) beneath it.

The catheter was first primed with 1% wt/vol Evans blue dye in dH₂O, and the infusion pump was set to a flowrate of 4 μL/min. To reduce the chance of backflow, the catheter tip was inserted into the milk-agarose gel before it solidified (Figure 6.1).

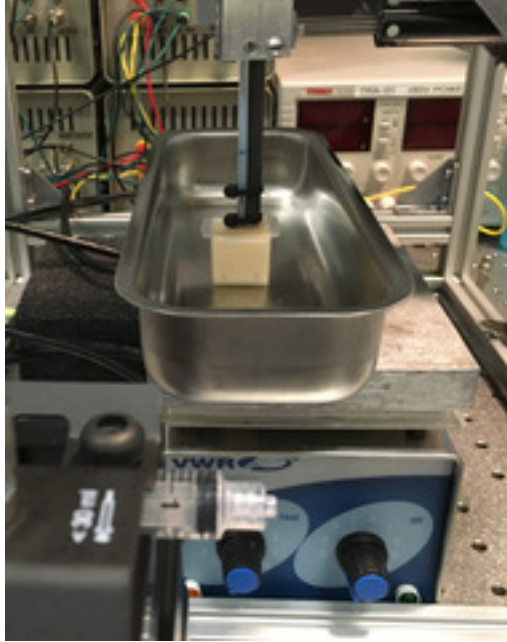


Figure 6.1: Experimental setup showing the milk-agarose gel solidified around the ultrasonic catheter.

Once the milk-agarose gel had cooled to 32°C, i.e., solidified, the experiment was ready to begin. Because the ultrasonic catheter generated heat when it was in operation and shut off at 43°C, the temperature at the ultrasonic tip fluctuated between 37°C and 43°C. To account for this heating, we had three experimental groups: ultrasound, no-ultrasound + heat, and no-ultrasound + no heat.

For the ultrasound experiments, the ultrasonic catheter was activated at the same time the infusion pump was turned on. For the no-ultrasound + no heat experiments, only the infusion pump was turned on. For the no-ultrasound + heat experiments, the hotplate was turned on to raise and maintain the temperature of the water bath at 37°C. In this case, the infusion pump was turned on when the temperature of the milk-agarose gel first reached 37°C.

The infusion pump was run for 50 minutes at a flowrate of 4 $\mu\text{L}/\text{min}$. After 50 minutes, the infusion pump was switched off. The gel was allowed to relax for 2 minutes before the ultrasonic catheter was removed.

The milk-agarose gel was immediately placed in dry ice and allowed to freeze.

6.2.3 Imaging and Analysis

The frozen agarose gel was then sectioned in a cryotome in 50- μm increments. Each slice was imaged using a microscope camera (Veho #VMS-004) and the recording software VideoVelocity (CandyLabs).

All image processing was performed using Fiji⁷¹. The images obtained were first deconvolved⁷³ to visualize only the blue color of Evans blue in the images. These images were then subjected to a global threshold and the area in each image was measured. These areas were then multiplied by the section interval of 50 μm to obtain a distribution volume for each infusion.

6.3 Results

6.3.1 Characterization of ultrasonic catheter

The central frequency of the catheter was measured to be 1.71 MHz and the duty cycle to be 8.8%. The acoustic pressure profile of the catheter as measured in water is shown in Figure 6.2, and appeared to follow a power law with an exponent of -1.12.

When 1% wt/vol Evans blue dye was infused into water while the ultrasound was on, we observed lateral motion of the dye reaching between 2–3.5 mm (Figure 6.3). This lateral movement of the dye was due to acoustic radiation force, while it is unclear if the upward movement of the dye is due to heat from the piezoelectric element.

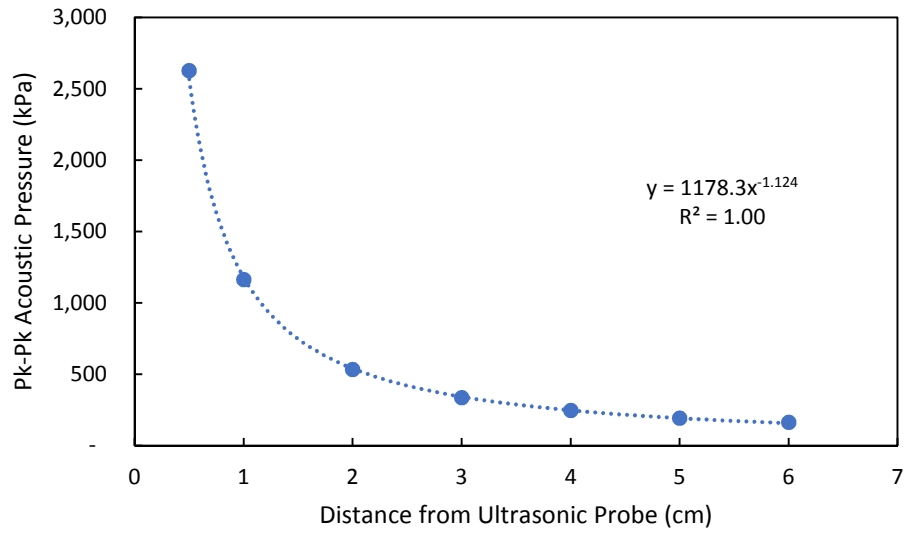


Figure 6.2: The peak-to-peak acoustic pressures are measured in water at regular intervals away from the tip of the catheter. The profile follows a power law.

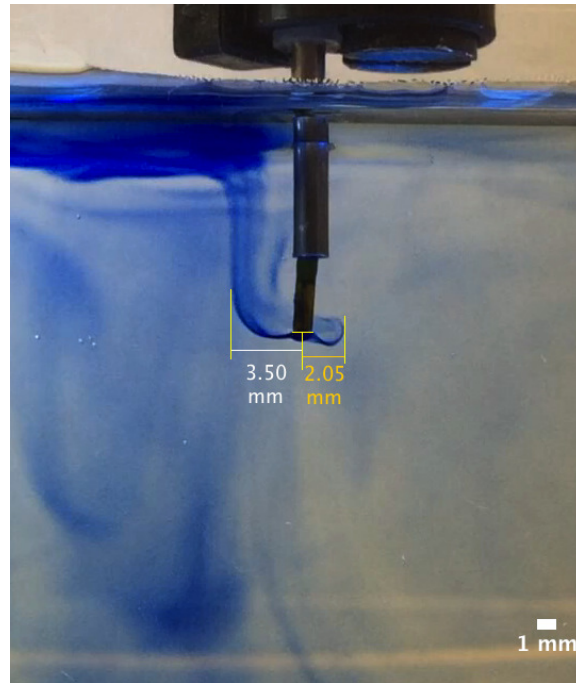


Figure 6.3: When 1% wt/vol Evans blue was infused into water, the radial ultrasound moved dye up to 3.5 mm away from the tip of the catheter.

6.3.2 Distribution volumes of 1% Evans blue dye in milk-agarose gels

There was no significant difference between the mean distribution volumes of 1% Evans blue dye for both the ultrasound and no-ultrasound + heat experiments as compared to the no-ultrasound + no heat experiments (Figure 6.4A).

Surprisingly, the measured V_d/V_i ratios are all less than 1.5 (Figure 6.4B), suggesting that the presence of evaporated milk greatly affected the distribution of 1% wt/vol Evans blue dye.

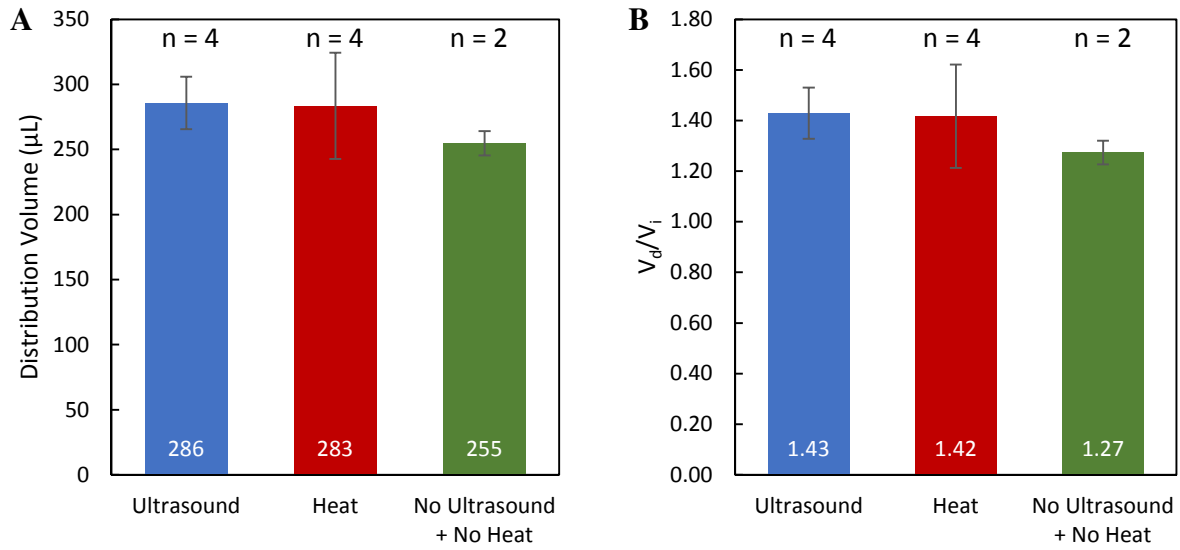


Figure 6.4: The mean distribution volumes of the ultrasound and heat experiments are 12% and 11% larger than the mean distribution volume of the no-ultrasound + no-heat experiments, respectively. The mean V_d/V_i for the ultrasound, heat, and no-ultrasound + no-heat experiments were 1.43, 1.42, and 1.16, respectively. At $\alpha = 0.05$, there is no significant difference between any of the groups.

6.4 Discussion

Radially emitted ultrasound did not appear to increase the distribution volume of 1% wt/vol Evans blue dye in 0.2% wt/vol agarose made in a 50:50 ratio with evaporated milk and water.

Assuming that the power law determined for the acoustic pressure profile of the catheter in water holds, the acoustic pressure just outside the catheter, i.e., 0.5 mm from the center, to 2 or 3 mm from the center would drop from 34.2 MPa_{app} to 7.2 or 4.6 MPa_{app}, respectively. The decrease described by this power law is mostly due to the spherical spread of the ultrasonic wave. It is likely that this power law is a good estimate of the acoustic pressure profile in 0.2% wt/vol agarose gel as well, but any movement of dye on the order of a few millimeters due to ultrasound is likely overshadowed by movement of dye due to the convective pressures from the infusion. In the case of the milk-agarose gel, the acoustic pressure gradient would be even steeper due to the increased ultrasound attenuation from the milk. While the acoustic pressure gradient may be steeper, the distance that this gradient covers is less than in water, suggesting that any enhancement in dye distribution from the ultrasound would be even more obscured by the dye distribution from CED alone.

A similar experiment, in which the infusion needle was the source of ultrasound, was performed by Mano et al. They report no enhancement in the distribution of Evans blue administered into agarose via CED when it was also paired with ultrasound as compared to without. This is despite seeing enhancement when they performed similar experiments in vivo in the brains of rodents and a non-human primate⁶⁷. Although they did not record the temperature of the infusion needle,

it is likely that there was heating, as their power inputs of ± 30 V and ± 60 V generated acoustic pressures less than 15 kPa, suggesting an inefficient acoustic setup.

One possibility is that the enhancement in distribution volume seen in vivo, either in the presence of ultrasound or heating, is due to biological responses that were triggered by the ultrasound or heating. For example, both hyperthermia and ultrasound can increase the permeability of the blood-brain barrier, which could allow the infused tracer to escape into the vasculature and reenter the brain downstream of the infusion site^{41,118}. The absence of these biological responses in agarose gel may account for the lack of distribution volume enhancement in these gel phantoms.

The measured V_d/V_i ratios are all less than 1.5 despite using only 0.2% wt/vol agarose. In Chapter 2, we found using MRI that an infusion of a gadolinium tracer (MW = 938) in 0.2% wt/vol agarose resulted in a V_d/V_i of 4.4. Evans blue (MW = 960) is similar in size, but the presence of milk appeared to hinder its transport.

For the heated experiments, despite heating the entire milk-agarose gel to 37°C, the distribution volume of Evans blue was not significantly different from when ultrasound was applied and the heating only occurred at the tip of the infusion catheter.

6.5 Conclusion

Radially emitted ultrasound did not appear to increase the distribution volume of 1% wt/vol Evans blue dye in 0.2% wt/vol milk-agarose gel made with a 50:50 ratio of evaporated milk and water. This may be due to the acoustic pressure gradients being generated over distances that are too close to the tip of the infusion catheter. As such, any enhancement in the distribution of the dye from the ultrasound may be overshadowed by the dye distribution from CED alone.

CHAPTER 7

STUDENT ADAPTATION TO THE MODULAR USE OF THE FLIPPED CLASSROOM IN AN INTRODUCTORY BIOMEDICAL ENGINEERING COURSE

7.1 Introduction

The Flipped Classroom is a pedagogical model that moves direct instruction outside of the classroom to allow more time in class for student-centered activities such as group work or peer-instruction. Bishop and Verleger define the Flipped Classroom as "an educational technique that consists of two parts: interactive group learning activities inside the classroom, and direct computer-based individual instruction outside the classroom"¹¹⁹.

The Flipped Classroom model began gaining popularity among K-12 education circles in the late 2000s when online lectures by two high school chemistry teachers, Bergmann and Sams, started spreading beyond their school¹²⁰. Since then, the Flipped Classroom model has been adopted by some educators in higher education as a possible means of improving student engagement and learning. In a recent scoping review, O'Flaherty and Phillips found that there is already a significant amount of evidence, albeit indirect, suggesting that the Flipped Classroom model does improve student academic performance in higher education¹²¹. In addition, a 2011 study by Deslauriers et al. found improved learning when students in an introductory undergraduate physics course were taught using "research-based instruction"¹²². While this "research-based

instruction” does not fit Bishop and Verleger’s definition of the Flipped Classroom—the direct individual instruction outside of class, namely, pre-class reading assignments, is not computer-based, and the authors never use the term Flipped Classroom—the format of the class is essentially a Flipped Classroom.

In spring 2015, we decided to use the Flipped Classroom model on the Biotransport Module of our Introductory Biomedical Engineering class, since the concepts and equations covered in this module are challenging for students to understand and apply. We believed that shifting the introduction of the concepts and the derivation of equations outside the class would allow us to better use class time by letting our students practice applying these concepts and equations, as well as addressing any student misconceptions.

However, given that a number of guides on flipping the classroom suggest spending a significant amount of time on the first day of class answering questions about the Flipped Classroom and convincing students of its merits^{120,123}, we became concerned about the feasibility of implementing it for only a small portion of the course. Considering that the Biotransport Module comprised only two 75-minute long class periods, spending even 15 minutes to sell the idea and address student concerns seemed like a huge time investment.

A literature search on the Flipped Classroom in higher education mostly turned up studies on courses that have been either partially or completely flipped for the entire semester, or partially flipped for a few classes¹²⁴⁻¹³⁰. All these studies show that students generally responded positively to the Flipped Classroom model, but only one (a complete flip for the entire semester)

explicitly mentioned an attempt to convince students of the merits of the Flipped Classroom—through the use of a “comprehensive syllabus”¹²⁴. The students in this study were also provided a guide that emphasized what student were responsible for in and out of class. In addition, two other studies, both also featuring courses that have been completely flipped for the entire semester, recommend providing students with “some structure and guidelines” and “well-structured guidance”^{125,126}. For the studies in which the instructor completely flipped only a small portion of the course, students still responded positively^{122,131,132}, although only Deslauriers et al. explicitly mentioned spending “several minutes” selling the idea to students¹²². Perhaps telling the students to watch the video lectures before class was all the instruction they needed prior to class?

The purpose of this study is to find out how easily students would adapt to the Flipped Classroom model if it was implemented without first convincing them of its benefits, as well as what students would have liked to have known prior to its implementation. This information would be useful to educators who want to completely flip only a small portion of their class, for reasons ranging from wanting to try the Flipped Classroom model, or deciding that only specific sections of the course would benefit from it. For this study, the Flipped Biotransport Module comprised video lectures and online quizzes outside class, and group-based problem solving inside class. This study was granted exemption status by Cornell’s Institutional Review Board.

7.2 Methods

All first-year students in the college of engineering are required to take an “Intro-to-Engineering” class, of which ENGRI 1310: Introduction to Biomedical Engineering is one of the nineteen options available. However, the class is also open to any student at Cornell University. The course was divided into 5 modules of varying lengths. Two modules were taught by guest instructors, one of which was the Biotransport Module that was taught by the first-author.

In this Introductory Biomedical Engineering course, the typical class period involved the instructor introducing and explaining new concepts to the students. The lessons typically include two to three multiple-choice “clicker” questions, either interspersed throughout the lecture, or saved for the very end of the lecture. To answer these “clicker” questions, students would use their personal response systems that have been preregistered with the class to submit their answers. The instructor would then display a histogram of how the class answered, before querying the students for explanations. Students were awarded points for participating, regardless of the veracity of their answers.

7.2.1 The Flipped Biotransport Module

The Flipped Biotransport Module comprised two class periods, each 75 mins long, during the 9th week of a 16-week semester. The first author was the instructor for the Biotransport Module.

Video lectures (Figure 7.1) were made using a Wacom Intuos Pro Tablet and the Ink2Go screencast software, and uploaded onto YouTube unlisted. This meant that only people with the link are able to view the video.

Student responsibilities before class were to view a series of video lectures, which come up to about 30 minutes per class. After watching the videos, students had to complete an online quiz, which comprises 3 questions, one of which is a “muddiest point” question.

During the class period, the instructor first clarified concepts and addressed misconceptions by reviewing with the class specific quiz responses that students had submitted. Students then spent the rest of class time working in groups to solve practice problems. The instructor facilitated this by posing a problem on the chalkboard, letting students discuss in their groups how to apply concepts from the video lectures to solve the problem, having several students explain their solutions, and providing feedback based on the student responses. This sequence was repeated until the end of the class period.

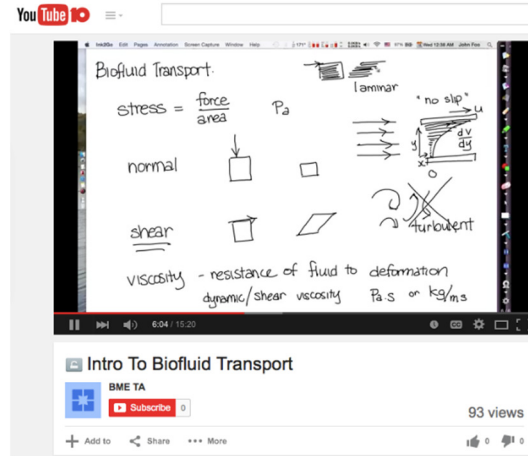


Figure 7.1: A screenshot of the Intro to Biofluid Transport video lecture.

7.2.2 Data collection

To answer the research question, the following qualitative and quantitative data were obtained and used.

7.2.3 YouTube Viewership Data

The number of unique views, total views, and mean view duration of each video were counted from the day the video was uploaded to the day of the corresponding class period, namely, three for the first class period and two for the second class period.

7.2.4 Online Survey

An online survey was administered one week after the second class period of the Flipped Biotransport Module. Students were given two weeks to complete the survey and were specifically told that the online survey was anonymous and voluntary. The survey began with Bishop and Verleger's definition of the Flipped Classroom to ensure that participants understood exactly what the term refers to in the survey.

For the Likert-like questions in the online survey, a neutral option was deliberately put in place to reduce agreeable bias.

To analyze the open-ended questions in the online survey, the responses were reviewed by the first author for general themes. The first author then went through all the responses again, and looked specifically for evidence of each theme in each response and labeled them accordingly. The number of times a theme was brought up was tabulated.

7.2.5 Classroom Observations

The instructor recorded his observations and reflections after each class period of the Flipped Biotransport Module. The instructor also invited a peer to observe the first of the two class periods.

7.3 Results

7.3.1 Results from YouTube Viewership Data

Viewership data obtained from YouTube (Table 7.1) suggest that most students viewed the video lectures, as the number of unique views for each video was close to the class enrollment of 44 students. Because the videos were posted on YouTube and were unlisted on search engines, only instructors and students with the links were able to watch the videos, but there was no way to track which individuals watched the videos, and how much of the videos they watched. While the instructional team comprised seven individuals—lead instructor, lab instructor, one post-doctoral guest lecturer, and four graduate teaching assistants (including the first author)—only the lead instructor and the first-author were responsible for the material covered in the

Biotransport Module. The unique views from the first two videos in the Biotransport Module (Intro to Biomass Transport and Fick's Law of Diffusion) that exceeded the class enrollment were likely due to some of the other instructors viewing the videos to provide constructive feedback to the first-author.

The mean view duration for each video is only about 60% of the video duration. Possible reasons for the low percentage include students re-watching specific sections of the video, as suggested by the total views outnumbering the unique views, or that students only watched portions of the video that they needed to answer the online quizzes.

Table 7.1: Although the number of unique views of each video is close to the total number of students, the mean view duration for each video is only about 60% of the video duration.

Lesson	Video	Unique Views	Total Views	Video Duration	Mean View Duration	% of Video Viewed
Biomass Transport	Intro to Biomass Transport	46	73	6:58	4:11	60%
	Fick's Law of Diffusion	48	66	12:36	7:11	57%
	Conservation of Mass	43	56	8:29	4:52	57%
Biofluid Transport	Intro to Biofluid Transport	41	57	15:21	8:38	56%
	Derivation of Poiseuille's Law	37	52	13:51	8:40	63%

7.3.2 Results from online survey

Of the 44 students in the class, 33 students participated in the survey, giving a response rate of 75%.

7.3.3 Demographic Information

Of the survey participants, all were freshmen save one, who was a sophomore. The gender breakdown was 73% female, and 27% male. In terms of college affiliation based on reported major, 88% of the participants belonged to the College of Engineering, 6% to the College of Arts and Sciences, while the remaining participants had not yet declared a major. As for the racial composition of the class, 59% identified as Caucasian, 19% as Black or African American, 19% as Hispanic, 15% as Asian, and 4% as Native American. Participants who declared multiple racial identities were counted in all the races they identified with. When participants were asked what grade they expected in the class, 45% expected an A, 45% expected a B, while 10% expected a C.

7.3.4 Prior Experience with the Flipped Classroom model

The majority of survey participants had experienced the Flipped Classroom model in some capacity prior to the Biotransport Module—33% first experienced it in high school and 37% first experienced it in college prior to the Biotransport Module. For 30% of the participants, the

Biotransport Module was their first experience with the Flipped Classroom model. None of the participants reported that they had experienced the Flipped Classroom model in middle school.

7.3.5 Student Perceptions about the use of the Flipped Classroom model for the Biotransport Module

The quantitative survey data on student perceptions are Likert-type data and have been presented in diverging stacked bar charts to highlight the spread of the positive and negative values, with the neutral point as the baseline¹³³.

The survey respondents generally perceived the use of the Flipped Classroom model for the Biotransport Module positively (Figure 7.2). The majority of the participants agreed or strongly agreed that the Flipped Classroom was engaging (70%), enjoyable (54%), and valuable (66%). Less than 10% of participants disagreed or strongly disagreed that the Flipped Classroom was engaging (9%), enjoyable (6%), and valuable (9%).

I found the use of the Flipped Classroom model for the Biotransport Module:

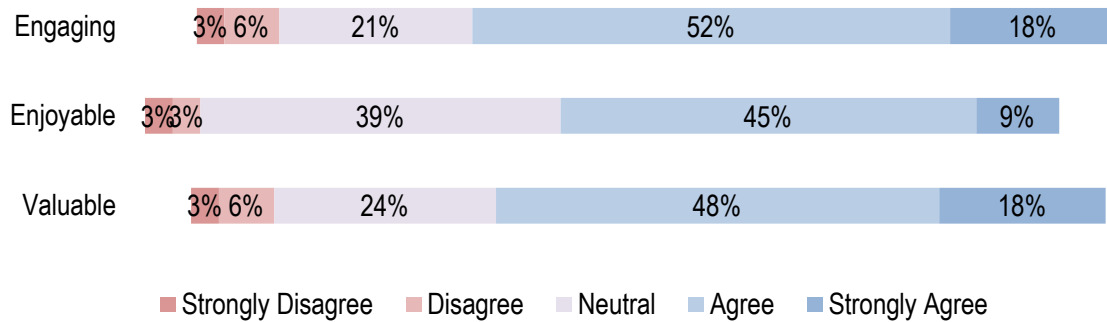


Figure 7.2: The survey respondents generally perceived the use of the Flipped Classroom model for the Biotransport Module positively.

The following aspects of the Biotransport Module helped me learn the material:

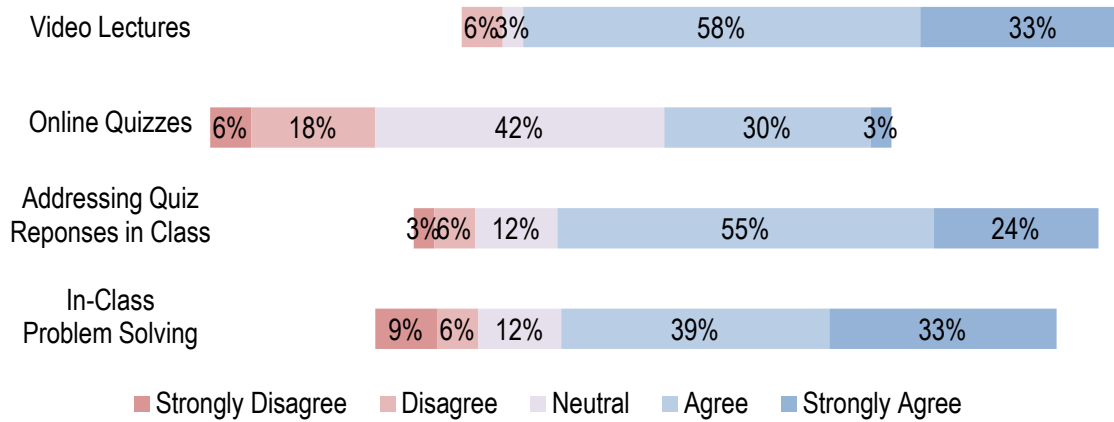
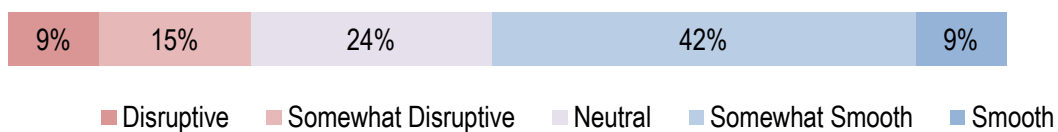


Figure 7.3: Video lectures and addressing quiz responses in class were the most helpful aspects of the Biotransport Module in helping students learn the material.

How was the mid-semester transition to using the Flipped Classroom model for the Biotransport Module?



How easily did you adapt to the use of the Flipped Classroom for the Biotransport Module?

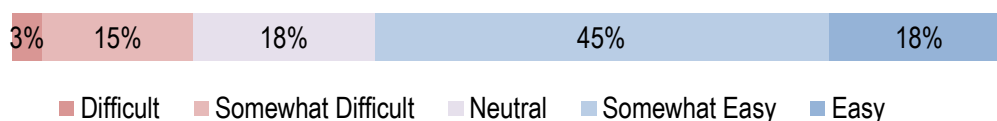


Figure 7.4: The majority of student respondents found the transition to the Flipped Classroom model smooth or somewhat smooth. An even larger majority adapted easily or somewhat easily to the use of the Flipped Classroom.

Regarding the transition to the Flipped Classroom model, 51% found the transition smooth or somewhat smooth, and 63% found adapting to the Flipped Classroom model easy or somewhat easy (Figure 7.4). A sizable minority of respondents found the transition to the Flipped Classroom model disruptive or somewhat disruptive (24%), and found adapting difficult or somewhat difficult (18%).

Of the four aspects of the Biotransport Module, the majority of survey respondents either agreed or strongly agreed that video lectures (91%) helped them learn the material, followed by the instructor addressing responses from the online quiz in class (79%), and solving problems in class (72%) (Figure 7.3). Only 33% of respondents agreed or strongly agreed that completing the online quizzes helped them learn the material, while 24% disagreed or strongly disagreed, with the remaining 42% having a neutral opinion.

7.3.6 Student Suggestions to make the Biotransport Module more conducive for learning

The top three themes that emerged from student suggestions to make the Flipped Biotransport Module more conducive for learning are as follows, with the numbers in parentheses representing the number of students who raised the theme:

1. Create **more structure** for in-class activities (9x).

One student found the class “kind of all over the place which makes it really hard to take notes and organize them later.” Yet another student found the group problem solving “chaotic,”

preferring instead to “solve the problems independently and then review the correct answer.”

Another student suggested “multiple choice questions instead of free responses,” which may suggest their preference for the order associated with clicker questions used in other modules of the class.

2. Provide **more practice problems** (7x).

This feedback relates less to the Flipped Classroom model than the class in its entirety, as this has been a common request throughout the semester. In fact, one student expressed that she enjoyed the Flipped Biotransport Module because she got to do more practice problems.

3. **Recap** information from the video lectures in class (5x).

While a number of students asked for “brief reviews” or “mini recaps,” one respondent went as far as suggesting the instructor “redo the main derivations in class.” In contrast to the requests for recapping the information from the video, a couple of respondents suggested “less time addressing quiz in class” and “not too much direct repeating of the videos in class, more moving on from the basic material.”

7.3.7 Student Suggestions to make the transition to the Flipped Module smoother

The top three themes that emerged from student suggestions to smoothen the transition to the Flipped Biotransport Module are as follows, with the numbers in parentheses representing the number of students who raised the theme:

1. Set **clearer expectations** for the Flipped Module (5x).

One student suggested that the instructor should “notify students so they don’t think the videos and quiz are as impromptu and supplemental as the random readings we sometimes get...”

Another said, “Because we were not notified that this was Flipped Classroom, I did not pay as much attention as I should have to the videos.” A third student who had a hard time adapting to the Flipped Classroom commented that the instructor “sort of just posted videos online with no pretext whatsoever. I had no idea what this was about until just now, so it was extremely awful. We jumped into it with no preparation.”

It was interesting that the students did not seem as concerned about the benefits of the Flipped Classroom, or why they were subjected to it. They instead seemed more focused on knowing what is expected of them, which may be due to the survey not set up to garner such responses.

2. **Flip other modules** in the class (4x).

Four students suggested flipping the other modules in the class as well, although they do not list

reasons for their suggestion.

3. Allow **more time** to complete pre-class activities (3x).

Students wanted “more time to watch the videos and answer the quiz.” This appears to be due to the shorter interval between the Tuesday and Thursday classes as compared to the interval between the Thursday and Tuesday classes, which includes the weekend.

7.3.8 Results from Student Work

The online quizzes had a mean completion rate of 98% (Table 7.2).

Table 7.2: Almost all the students completed the online quizzes. The student that missed the Biomass Transport quiz is different from the student that missed the Biofluid Transport quiz.

Lesson	Number Completed	Total	% Completed
Biomass Transport	43	44	98%
Biofluid Transport	43	44	98%

7.3.9 Results from Classroom Observations

Despite being instructed to work in groups of 4–5, a number of individuals worked alone or in pairs. If the question was open-ended, students tended to immediately begin discussing the problem; if the question involved mathematical calculations, students tended to work alone before consulting their group. Students used their cell phones to research answers for open-ended questions, but also to access social media, specifically Facebook. Students worked at very different paces, with some students struggling, while others were done quickly. This made it challenging to pace the class. A few students did not work on the in-class questions, and only paid attention when the answers were being addressed.

7.3.10 Instructor Reflections on Flipping the Classroom

The instructor found that creating video lectures was manageable with assistance. Using the tablet and screencasting software to create the video lectures was straightforward after getting guidance from Cornell's Academic Technologies Center. The instructor also found that scripting the video lecture greatly reduced the need for video editing.

The instructor was able to quickly and easily address misconceptions. Viewing the quiz responses the night before class alerted the instructor to common misconceptions, and gave him time to formulate a coherent response.

The instructor found structuring the in-class activity very challenging. It was difficult to get

everyone working in groups, a problem that was exacerbated by the lecture hall setup. Some students who quickly solved the practice questions got bored while students who were struggling were consulting the instructor instead of their peers.

Fielding open-ended questions was also immensely challenging, as it was impossible to anticipate the wide variety of student responses.

Having every student bring a device that can connect to the internet may allow for the entire class to conduct research together. Students can work in groups to ensure that at least one group member has access to the internet. Polling students at the start of class may be necessary to identify students who require assistance in obtaining a device.

7.4 Discussion

The YouTube Viewership data (~60% mean view duration) and the online quiz completion rates (98%) suggest that a number of students took the quizzes without watching the videos in their entirety. This behavior may be partially explained by the online survey finding that a number of students were not aware that they needed to know all the material in the videos. This behavior may in turn explain why a number of students wanted the instructor to recap the material during class. Setting clearer expectations would encourage more students to watch the video lectures in their entirety.

While the majority of the freshmen in the class found the transition to the Flipped Classroom

module easy or somewhat easy to adapt to, 18% found it difficult or somewhat difficult. While learning about the purported benefits of the Flipped Classroom may help these particular students adapt better, they seem more concerned about the instructor “giving warning” so they do not go into class “with no preparation.” These ideas were also echoed by students who did adapt easily to the Flipped Classroom. This group of students appeared more concerned about what was expected of them, and how they can do well in the class.

While the instructor did not detect any concerns regarding the effectiveness or use of the Flipped Classroom model per se, a handful of students expressed interest in how the material covered in the video lectures fit into the big picture. As such, highlighting this information in the video lectures may further increase their value to student learning.

This study sought to address if it is possible to implement the Flipped Classroom on a limited scale without first selling the idea to students. These data suggest that students will easily adapt to the modular use of the Flipped Classroom when the instructor clearly informs them of what is expected of them, and what their responsibilities are, not unlike informing students of the rules of an activity.

Limitations of this study were that the first author, who is also the instructor, is a graduate teaching assistant who had no prior experience teaching this course, and no prior experience implementing the Flipped Classroom model. He did, however, get a lot of guidance from the professor of the course.

The content of the Biotransport Module was developed specially for this class, and there were no prior lectures to copy from. The author's experience thus more accurately represents the experience of a new faculty member developing the course content for a course they have been assigned, rather than that of an experienced faculty member wanting to try the Flipped Classroom for the first time.

No attempt was made to evaluate the efficacy of the Flipped Classroom model as this was a new class. No comparison with previous years was possible, and there was only one section in the class.

7.5 Conclusions

The majority of the freshmen in this class found the transition to the Flipped Classroom module easy or somewhat easy to adapt to. Setting clearer expectations for the Flipped Module and creating more structure for the in-class activities may further smoothen the transition, especially for students who had difficulty adapting. Educators may consider these strategies as they implement the Flipped Classroom in a modular fashion, either for appropriate topics or as a step to eventually flipping the entire course.

7.6 Acknowledgements

We would like to thank my students and co-instructors in BME 1310, Bailey Cooper, Meghnaa Tallapragada, my peers in ALS 6016, and Benjamin Moss from the Cornell Academic

Technologies Center for their support and feedback throughout this study.

REFERENCES

1. Ostrom, Q. T. *et al.* CBTRUS Statistical Report: Primary Brain and Central Nervous System Tumors Diagnosed in the United States in 2006-2010. *Neuro-Oncol.* **15**, ii1–ii56 (2013).
2. Corso, C. D. & Bindra, R. S. Success and Failures of Combined Modalities in Glioblastoma Multiforme: Old Problems and New Directions. *Semin. Radiat. Oncol.* **26**, 281–298 (2016).
3. Giese, A., Bjerkvig, R., Berens, M. e. & Westphal, M. Cost of Migration: Invasion of Malignant Gliomas and Implications for Treatment. *J. Clin. Oncol.* **21**, 1624–1636 (2003).
4. Lefranc, F., Brotchi, J. & Kiss, R. Possible Future Issues in the Treatment of Glioblastomas: Special Emphasis on Cell Migration and the Resistance of Migrating Glioblastoma Cells to Apoptosis. *J. Clin. Oncol.* **23**, 2411–2422 (2005).
5. Olbricht, W. The Blood-Brain Barrier and Drug Delivery. *Chem. Eng. Prog.* **109**, 31–34 (2013).
6. Lonser, R. R., Sarntinoranont, M., Morrison, P. F. & Oldfield, E. H. Convection-enhanced delivery to the central nervous system. *J. Neurosurg.* **122**, 697–706 (2014).
7. Hersh, D. S. *et al.* Emerging Applications of Therapeutic Ultrasound in Neuro-oncology: Moving Beyond Tumor Ablation. *Neurosurgery* **79**, (2016).
8. Zhou, Z., Singh, R. & Souweidane, M. M. Convection-Enhanced Delivery for Diffuse Intrinsic Pontine Glioma Treatment. *Curr. Neuropharmacol.* **15**, 116–128 (2017).
9. Westphal, M. *et al.* A phase 3 trial of local chemotherapy with biodegradable carmustine (BCNU) wafers (Gliadel wafers) in patients with primary malignant glioma. *Neuro-Oncol.* **5**, 79–88 (2003).

10. Bobo, R. H. *et al.* Convection-enhanced delivery of macromolecules in the brain. *Proc. Natl. Acad. Sci.* **91**, 2076–2080 (1994).
11. Morrison, P. F., Laske, D. W., Bobo, H., Oldfield, E. H. & Dedrick, R. L. High-flow microinfusion: tissue penetration and pharmacodynamics. *Am. J. Physiol.-Regul. Integr. Comp. Physiol.* **266**, R292–R305 (1994).
12. Miranpuri, G. *et al.* Convection Enhanced Delivery: A Comparison of infusion characteristics in ex vivo and in vivo non-human primate brain tissue. *Ann. Neurosci.* **20**, 108–114 (2013).
13. Sampson, J. H. *et al.* Poor drug distribution as a possible explanation for the results of the PRECISE trial: Clinical article. *J. Neurosurg.* **113**, 301–309 (2010).
14. Olanow, W. *et al.* Gene delivery of neurturin to putamen and substantia nigra in Parkinson disease: A double-blind, randomized, controlled trial. *Ann. Neurol.* **78**, 248–257 (2015).
15. Kunwar, S. *et al.* Phase III randomized trial of CED of IL13-PE38QQR vs Gliadel wafers for recurrent glioblastoma. *Neuro-Oncol.* **12**, 871–881 (2010).
16. Jahangiri, A. *et al.* Convection-enhanced delivery in glioblastoma: a review of preclinical and clinical studies. *J. Neurosurg.* **126**, 191–200 (2016).
17. Efficacy and safety of AP 12009 in patients with recurrent or refractory anaplastic astrocytoma (SAPPHIRE). *ClinicalTrials.gov [Internet]. Bethesda (MD): National library of Medicine (US)* (2008).
18. Raghavan, R., Brady, M. L. & Sampson, J. H. Delivering therapy to target: improving the odds for successful drug development. *Ther. Deliv.* **7**, 457–481 (2016).
19. Mason, T. J. Therapeutic ultrasound an overview. *Ultrason. Sonochem.* **18**, 847–852 (2011).

20. O'Brien, W. D. Ultrasound–biophysics mechanisms. *Prog. Biophys. Mol. Biol.* **93**, 212–255 (2007).
21. Mitragotri, S. Healing sound: the use of ultrasound in drug delivery and other therapeutic applications. *Nat. Rev. Drug Discov.* **4**, 255–260 (2005).
22. Liu, Y. *et al.* Ultrasound-Enhanced Drug Transport and Distribution in the Brain. *AAPS PharmSciTech* **11**, 1005–1017 (2010).
23. Olbricht, W., Sistla, M., Ghandi, G., Lewis, G. & Sarvazyan, A. Time-reversal acoustics and ultrasound-assisted convection-enhanced drug delivery to the brain. *J. Acoust. Soc. Am.* **134**, 1569–1575 (2013).
24. Lewis Jr., G. K. *et al.* Time-reversal Techniques in Ultrasound-assisted Convection-enhanced Drug Delivery to the Brain: Technology Development and In Vivo Evaluation. *Proc. Meet. Acoust.* **11**, 020005 (2010).
25. Lewis, G. K., Schulz, Z. R., Pannullo, S. C., Southard, T. L. & Olbricht, W. L. Ultrasound-assisted convection-enhanced delivery to the brain in vivo with a novel transducer cannula assembly. *J. Neurosurg.* **117**, 1128–1140 (2012).
26. Courtney, C. R. P. *et al.* Manipulation of particles in two dimensions using phase controllable ultrasonic standing waves. *Proc. R. Soc. Math. Phys. Eng. Sci.* [rspa20110269](https://doi.org/10.1098/rspa.2011.0269) (2011). doi:10.1098/rspa.2011.0269
27. Gherardini, L. *et al.* A new immobilisation method to arrange particles in a gel matrix by ultrasound standing waves. *Ultrasound Med. Biol.* **31**, 261–272 (2005).
28. Woodside, S. M., Piret, J. M., Gröschl, M., Benes, E. & Bowen, B. D. Acoustic force distribution in resonators for ultrasonic particle separation. *AIChE J.* **44**, 1976–1984 (1998).

29. Raeymaekers, B., Pantea, C. & Sinha, D. N. Manipulation of diamond nanoparticles using bulk acoustic waves. *J. Appl. Phys.* **109**, 014317 (2011).
30. Hertz, G. & Mende, H. Der Schallstrahlungsdruck in Flüssigkeiten. *Z. Für Phys.* **114**, 354–367
31. O’Neill, B. E. *et al.* Pulsed High Intensity Focused Ultrasound Mediated Nanoparticle Delivery: Mechanisms and Efficacy in Murine Muscle. *Ultrasound Med. Biol.* **35**, 416–424 (2009).
32. Fink, M. Time reversal of ultrasonic fields. I. Basic principles. *IEEE Trans. Ultrason. Ferroelectr. Freq. Control* **39**, 555–566 (1992).
33. Thomas, J.-L. & Fink, M. A. Ultrasonic beam focusing through tissue inhomogeneities with a time reversal mirror: application to transskull therapy. *IEEE Trans. Ultrason. Ferroelectr. Freq. Control* **43**, 1122–1129 (1996).
34. Fink, M., Montaldo, G. & Tanter, M. Time-Reversal Acoustics in Biomedical Engineering. *Annu. Rev. Biomed. Eng.* **5**, 465–497 (2003).
35. Pitt, W. G., Hussein, G. A. & Staples, B. J. Ultrasonic drug delivery – a general review. *Expert Opin. Drug Deliv.* **1**, 37–56 (2004).
36. Vlachos, F., Tung, Y.-S. & Konofagou, E. Permeability dependence study of the focused ultrasound-induced blood-brain barrier opening at distinct pressures and microbubble diameters using DCE-MRI. *Magn. Reson. Med. Off. J. Soc. Magn. Reson. Med. Soc. Magn. Reson. Med.* **66**, 821–830 (2011).
37. Schneider, M. Characteristics of SonoVue™. *Echocardiography* **16**, 743–746 (1999).

38. Gorce, J.-M., Arditi, M. & Schneider, M. Influence of bubble size distribution on the echogenicity of ultrasound contrast agents: A study of SonoVue™. *Invest. Radiol.* **35**, 661–671 (2000).
39. Thorne, R. G. & Nicholson, C. In vivo diffusion analysis with quantum dots and dextrans predicts the width of brain extracellular space. *Proc. Natl. Acad. Sci.* **103**, 5567–5572 (2006).
40. Nance, E. A. *et al.* A Dense Poly(Ethylene Glycol) Coating Improves Penetration of Large Polymeric Nanoparticles Within Brain Tissue. *Sci. Transl. Med.* **4**, 149ra119-149ra119 (2012).
41. Wang, S. *et al.* Direct brain infusion can be enhanced with focused ultrasound and microbubbles. *J. Cereb. Blood Flow Metab.* **37**, 706–714 (2017).
42. Pardridge, W. M. CNS Drug Design Based on Principles of Blood-Brain Barrier Transport. *J. Neurochem.* **70**, 1781–1792 (1998).
43. Sindhvani, N., Ivanchenko, O., Lueshen, E., Prem, K. & Linninger, A. A. Methods for Determining Agent Concentration Profiles in Agarose Gel During Convection-Enhanced Delivery. *IEEE Trans. Biomed. Eng.* **58**, 626–632 (2011).
44. Ivanchenko, O., Sindhvani, N. & Linninger, A. Experimental Techniques for Studying Poroelasticity in Brain Phantom Gels Under High Flow Microinfusion. *J. Biomech. Eng.* **132**, 051008–051008 (2010).
45. Linninger, A. A., Somayaji, M. R., Mekarski, M. & Zhang, L. Prediction of convection-enhanced drug delivery to the human brain. *J. Theor. Biol.* **250**, 125–138 (2008).
46. Krauze, M. T. *et al.* Reflux-free cannula for convection-enhanced high-speed delivery of therapeutic agents. *J. Neurosurg.* **103**, (2005).

47. Gill, T. *et al.* In vitro and in vivo testing of a novel recessed-step catheter for reflux-free convection-enhanced drug delivery to the brain. *J. Neurosci. Methods* **219**, 1–9 (2013).
48. Chen, Z.-J. *et al.* A realistic brain tissue phantom for intraparenchymal infusion studies. *J. Neurosurg.* **101**, 314–322 (2004).
49. Sillay, K. *et al.* Benchmarking the ERG valve tip and MRI Interventions Smart Flow neurocatheter convection-enhanced delivery system's performance in a gel model of the brain: employing infusion protocols proposed for gene therapy for Parkinson's disease. *J. Neural Eng.* **9**, 026009 (2012).
50. Chen, Z.-J., Broaddus, W. C., Viswanathan, R. R., Raghavan, R. & Gillies, G. T. Intraparenchymal drug delivery via positive-pressure infusion: experimental and modeling studies of poroelasticity in brain phantom gels. *IEEE Trans. Biomed. Eng.* **49**, 85–96 (2002).
51. Pluen, A., Netti, P. A., Jain, R. K. & Berk, D. A. Diffusion of macromolecules in agarose gels: comparison of linear and globular configurations. *Biophys. J.* **77**, 542–552 (1999).
52. Gu, W. Y., Yao, H., Vega, A. L. & Flagler, D. Diffusivity of Ions in Agarose Gels and Intervertebral Disc: Effect of Porosity. *Ann. Biomed. Eng.* **32**, 1710–1717 (2004).
53. Syková, E. & Nicholson, C. Diffusion in Brain Extracellular Space. *Physiol. Rev.* **88**, 1277–1340 (2008).
54. Bird, R. B., Stewart, W. E. & Lightfoot, E. N. *Transport Phenomena*. (New York: Wiley, 2002).
55. Neeves, K. B., Lo, C. T., Foley, C. P., Saltzman, W. M. & Olbricht, W. L. Fabrication and characterization of microfluidic probes for convection enhanced drug delivery. *J. Controlled Release* **111**, 252–262 (2006).

56. Lewis, G., Wang, P., Lewis, G., Olbricht, W. & Ebbini, E. S. Therapeutic Ultrasound Enhancement of Drug Delivery to Soft Tissues. *AIP Conf. Proc.* **1113**, 403–407 (2009).
57. Lewis, G. K. & Olbricht, W. A phantom feasibility study of acoustic enhanced drug perfusion in neurological tissue. in *Life Science Systems and Applications Workshop, 2007. LISA 2007. IEEE/NIH* 67–70 (2007). doi:10.1109/LSSA.2007.4400886
58. Chen, X., Astarly, G. W., Sepulveda, H., Mareci, T. H. & Sarntinoranont, M. Quantitative assessment of macromolecular concentration during direct infusion into an agarose hydrogel phantom using contrast-enhanced MRI. *Magn. Reson. Imaging* **26**, 1433–1441 (2008).
59. Yushkevich, P. A. *et al.* User-Guided 3D Active Contour Segmentation of Anatomical Structures: Significantly Improved Efficiency and Reliability. *Neuroimage* **31**, 1116–1128 (2006).
60. Crank, J. *The mathematics of diffusion.* (Oxford university press, 1979).
61. Osuga, T. & Han, S. Proton magnetic resonance imaging of diffusion of high- and low-molecular-weight contrast agents in opaque porous media saturated with water. *Magn. Reson. Imaging* **22**, 1039–1042 (2004).
62. Arnott, S. *et al.* The agarose double helix and its function in agarose gel structure. *J. Mol. Biol.* **90**, 269–284 (1974).
63. Brady, M., Raghavan, R., Chen, Z.-J. & Broaddus, W. C. Quantifying Fluid Infusions and Tissue Expansion in Brain. *IEEE Trans. Biomed. Eng.* **58**, 2228–2237 (2011).
64. Iyer, R. R. *et al.* Tracking accuracy of T2- and diffusion-weighted magnetic resonance imaging for infusate distribution by convection-enhanced delivery: Laboratory investigation. *J. Neurosurg.* **115**, 474–480 (2011).

65. Blakeley, J. & Grossman, S. A. Chapter 17 - Chemotherapy with cytotoxic and cytostatic agents in brain cancer. in *Neuro-Oncology* (eds. Aminoff, M. J., Boller, F. & Swaab, D. F.) **104**, 229–254 (Elsevier, 2012).
66. Agarwala, S. S. & Kirkwood, J. M. Temozolomide, a Novel Alkylating Agent with Activity in the Central Nervous System, May Improve the Treatment of Advanced Metastatic Melanoma. *The Oncologist* **5**, 144–151 (2000).
67. Mano, Y. *et al.* Intraparenchymal ultrasound application and improved distribution of infusate with convection-enhanced delivery in rodent and nonhuman primate brain. *J. Neurosurg.* 1–11 (2015). doi:10.3171/2015.3.JNS142152
68. Hancock, H. A. *et al.* Investigations into Pulsed High-Intensity Focused Ultrasound–Enhanced Delivery: Preliminary Evidence for a Novel Mechanism. *Ultrasound Med. Biol.* **35**, 1722–1736 (2009).
69. Dasgupta, A. *et al.* Ultrasound-mediated drug delivery to the brain: principles, progress and prospects. *Drug Discov. Today Technol.* **20**, 41–48 (2016).
70. Paxinos, G. & Watson, C. *The rat brain in stereotaxic coordinates: hard cover edition.* (Academic press, 2006).
71. Schindelin, J. *et al.* Fiji: an open-source platform for biological-image analysis. *Nat. Methods* **9**, 676 (2012).
72. Unger, E. C. *et al.* Therapeutic applications of lipid-coated microbubbles. *Adv. Drug Deliv. Rev.* **56**, 1291–1314 (2004).
73. Ruifrok, A. & Johnston, D. Quantification of histochemical staining by color deconvolution. *Anal. Quant. Cytol. Histol. Int. Acad. Cytol. Am. Soc. Cytol.* **23**, 291–299 (2001).

74. Morrison, P. F., Chen, M. Y., Chadwick, R. S., Lonser, R. R. & Oldfield, E. H. Focal delivery during direct infusion to brain: role of flow rate, catheter diameter, and tissue mechanics. *Am. J. Physiol.* **277**, R1218-1229 (1999).
75. Bohne, G., Richter, E., Woehlecke, H. & Ehwald, R. Diffusion Barriers of Tripartite Sporopollenin Microcapsules Prepared from Pine Pollen. *Ann. Bot.* **92**, 289–297 (2003).
76. Saunders, N. R., Dziegielewska, K. M., Møllgård, K. & Habgood, M. D. Markers for blood-brain barrier integrity: how appropriate is Evans blue in the twenty-first century and what are the alternatives? *Neurogenomics* 385 (2015). doi:10.3389/fnins.2015.00385
77. Shekhar, H., Rychak, J. J. & Doyley, M. M. Modifying the size distribution of microbubble contrast agents for high-frequency subharmonic imaging. *Med. Phys.* **40**, n/a-n/a (2013).
78. Singh, R. *et al.* Volume of distribution and clearance of peptide-based nanofiber after convection-enhanced delivery. *J. Neurosurg.* 1–9 (2017). doi:10.3171/2017.2.JNS162273
79. Sirianni, R. W. *et al.* Radiolabeling of Poly(lactic-co-glycolic acid) (PLGA) Nanoparticles with Biotinylated F-18 Prosthetic Groups and Imaging of Their Delivery to the Brain with Positron Emission Tomography. *Bioconjug. Chem.* **25**, 2157–2165 (2014).
80. Noble, C. O. *et al.* Novel Nanoliposomal CPT-11 Infused by Convection-Enhanced Delivery in Intracranial Tumors: Pharmacology and Efficacy. *Cancer Res.* **66**, 2801–2806 (2006).
81. Timbie, K. F. *et al.* MR image-guided delivery of cisplatin-loaded brain-penetrating nanoparticles to invasive glioma with focused ultrasound. *J. Controlled Release* **263**, 120–131 (2017).
82. Sawyer, A. J. *et al.* Convection-enhanced delivery of camptothecin-loaded polymer nanoparticles for treatment of intracranial tumors. *Drug Deliv. Transl. Res.* **1**, 34–42 (2011).

83. Stephen, Z. R. *et al.* Redox-Responsive Magnetic Nanoparticle for Targeted Convection-Enhanced Delivery of O6-Benzylguanine to Brain Tumors. *ACS Nano* **8**, 10383–10395 (2014).
84. Rosch, J. G. Transport in the Perivascular Spaces of the Brain: Visualization of Convection-Enhanced Delivery. (2017). doi:<http://doi.org/10.7298/X4PR7SZS>
85. Wolak, D. J. & Thorne, R. G. Diffusion of Macromolecules in the Brain: Implications for Drug Delivery. *Mol. Pharm.* **10**, 1492–1504 (2013).
86. Lieberman, D. M., Laske, D. W., Morrison, P. F., Bankiewicz, K. S. & Oldfield, E. H. Convection-enhanced distribution of large molecules in gray matter during interstitial drug infusion. *J. Neurosurg.* **82**, 1021–1029 (1995).
87. Neeves, K. B., Sawyer, A. J., Foley, C. P., Saltzman, W. M. & Olbricht, W. L. Dilation and degradation of the brain extracellular matrix enhances penetration of infused polymer nanoparticles. *Brain Res.* **1180**, 121–132 (2007).
88. MacKay, J. A., Deen, D. F. & Szoka, F. C. Distribution in brain of liposomes after convection enhanced delivery; modulation by particle charge, particle diameter, and presence of steric coating. *Brain Res.* **1035**, 139–153 (2005).
89. Li, K. *et al.* Real-time magnetic resonance imaging visualization and quantitative assessment of diffusion in the cerebral extracellular space of C6 glioma-bearing rats. *Neurosci. Lett.* **543**, 84–89 (2013).
90. Zhang, C. *et al.* Convection enhanced delivery of cisplatin-loaded brain penetrating nanoparticles cures malignant glioma in rats. *J. Controlled Release* **263**, 112–119 (2017).

91. Graybiel, A. M. & Ragsdale, C. W. Histochemically distinct compartments in the striatum of human, monkeys, and cat demonstrated by acetylthiocholinesterase staining. *Proc. Natl. Acad. Sci. U. S. A.* **75**, 5723–5726 (1978).
92. Graybiel, A. M., Flaherty, A. W. & Giménez-Amaya, J.-M. Striosomes and Matrisomes. in *The Basal Ganglia III* (eds. Bernardi, G., Carpenter, M. B., Di Chiara, G., Morelli, M. & Stanzione, P.) 3–12 (Springer New York, 1991). doi:10.1007/978-1-4684-5871-8_1
93. Friedman, A. *et al.* A Corticostriatal Path Targeting Striosomes Controls Decision-Making under Conflict. *Cell* **161**, 1320–1333 (2015).
94. Langley, K. C., Bergson, C., Greengard, P. & Ouimet, C. C. Co-localization of the D1 dopamine receptor in a subset of DARPP-32-containing neurons in rat caudate–putamen. *Neuroscience* **78**, 977–983 (1997).
95. Berendse, H. W., Graaf, Y. G.-D. & Groenewegen, H. J. Topographical organization and relationship with ventral striatal compartments of prefrontal corticostriatal projections in the rat. *J. Comp. Neurol.* **316**, 314–347 (1992).
96. Chronister, R. B., Farnell, K. E., Marco, L. A. & White, L. E. The rodent neostriatum: A golgi analysis. *Brain Res.* **108**, 37–46 (1976).
97. Voříšek, I. & Syková, E. Evolution of Anisotropic Diffusion in the Developing Rat Corpus Callosum. *J. Neurophysiol.* **78**, 912–919 (1997).
98. Dodt, H.-U. *et al.* Ultramicroscopy: three-dimensional visualization of neuronal networks in the whole mouse brain. *Nat. Methods* **4**, 331 (2007).
99. Clancy, B. & Cauller, L. J. Reduction of background autofluorescence in brain sections following immersion in sodium borohydride. *J. Neurosci. Methods* **83**, 97–102 (1998).

100. Chen, M. Y. *et al.* Surface properties, more than size, limiting convective distribution of virus-sized particles and viruses in the central nervous system. *J. Neurosurg.* **103**, 311–319 (2005).
101. Wang, M. *et al.* A Murine Model for Quantitative, Real-Time Evaluation of Convection-Enhanced Delivery (RT-CED) Using an 18[F]-Positron Emitting, Fluorescent Derivative of Dasatinib. *Mol. Cancer Ther.* **16**, 2902–2912 (2017).
102. Moses, W. W. Fundamental limits of spatial resolution in PET. *Nucl. Instrum. Methods Phys. Res. Sect. Accel. Spectrometers Detect. Assoc. Equip.* **648**, S236–S240 (2011).
103. Zhou, J. *et al.* Highly penetrative, drug-loaded nanocarriers improve treatment of glioblastoma. *Proc. Natl. Acad. Sci.* **110**, 11751–11756 (2013).
104. Lehman, J. F., Greenberg, B. D., McIntyre, C. C., Rasmussen, S. A. & Haber, S. N. Rules Ventral Prefrontal Cortical Axons Use to Reach Their Targets: Implications for Diffusion Tensor Imaging Tractography and Deep Brain Stimulation for Psychiatric Illness. *J. Neurosci.* **31**, 10392–10402 (2011).
105. Ciesielska, A. *et al.* Anterograde Axonal Transport of AAV2-GDNF in Rat Basal Ganglia. *Mol. Ther.* **19**, 922–927 (2011).
106. Yazdan-Shahmorad, A. *et al.* Widespread optogenetic expression in macaque cortex obtained with MR-guided, convection enhanced delivery (CED) of AAV vector to the thalamus. *J. Neurosci. Methods* **293**, 347–358 (2018).
107. Ksendzovsky, A. *et al.* Convection-enhanced delivery of M13 bacteriophage to the brain. *J. Neurosurg.* **117**, 197–203 (2012).
108. Ruggeri, F. *et al.* Non-specific interactions between soluble proteins and lipids induce irreversible changes in the properties of lipid bilayers. *Soft Matter* **9**, 4219–4226 (2013).

109. Abreu, M. S. C., Estronca, L. M. B. B., Moreno, M. J. & Vaz, W. L. C. Binding of a Fluorescent Lipid Amphiphile to Albumin and its Transfer to Lipid Bilayer Membranes. *Biophys. J.* **84**, 386–399 (2003).
110. Charbonneau, D. M. & Tajmir-Riahi, H.-A. Study on the Interaction of Cationic Lipids with Bovine Serum Albumin. *J. Phys. Chem. B* **114**, 1148–1155 (2010).
111. Engwer, C., Hillen, T., Knappitsch, M. & Surulescu, C. Glioma follow white matter tracts: a multiscale DTI-based model. *J. Math. Biol.* **71**, 551–582 (2015).
112. Giese, A. & Westphal, M. Glioma Invasion in the Central Nervous System. *Neurosurgery* **39**, 235–252 (1996).
113. Tsukamoto, A. *et al.* 1-MHz ultrasound enhances internal diffusivity in agarose gels. *Appl. Acoust.* **74**, 1117–1121 (2013).
114. Lavon, I. & Kost, J. Mass transport enhancement by ultrasound in non-degradable polymeric controlled release systems. *J. Controlled Release* **54**, 1–7 (1998).
115. Farrer, A. Development and Characterization of Tissue-Mimicking Gelatin Phantoms for use with MRgFUS. (2014).
116. Madsen, E. L., Frank, G. R. & Dong, F. Liquid or Solid Ultrasonically Tissue-Mimicking Materials with Very Low Scatter. *Ultrasound Med. Biol.* **24**, 535–542 (1998).
117. Lewis, G. Medical Ultrasound For Brain Drug Delivery And Rehabilitation Medicine. (2012).
118. Kiyatkin, E. A. & Sharma, H. S. Permeability of the blood–brain barrier depends on brain temperature. *Neuroscience* **161**, 926–939 (2009).
119. Bishop, J. L. & Verleger, M. A. The flipped classroom: A survey of the research. in *ASEE National Conference Proceedings, Atlanta, GA* (2013).

120. Bergmann, J. & Sams, A. *Flip your classroom: Reach every student in every class every day*. (International Society for Technology in Education, 2012).
121. O’Flaherty, J. & Phillips, C. The use of flipped classrooms in higher education: A scoping review. *Internet High. Educ.* **25**, 85–95 (2015).
122. Deslauriers, L., Schelew, E. & Wieman, C. Improved Learning in a Large-Enrollment Physics Class. *Science* **332**, 862–864 (2011).
123. Coursera’s Flipped Classroom Field Guide. Available at:
<https://docs.google.com/document/d/1arP1QAKSyVcxKYYgTJWCrJf02NdephTVGQltsw-S1fQ/edit?pli=1#bookmark=id.bslf3vgya1li>. (Accessed: 2nd March 2015)
124. McLaughlin, J. E. *et al.* The Flipped Classroom: A Course Redesign to Foster Learning and Engagement in a Health Professions School. *Acad. Med.* **89**, 236–243 (2014).
125. Mason, G. S., Shuman, T. R. & Cook, K. E. Comparing the Effectiveness of an Inverted Classroom to a Traditional Classroom in an Upper-Division Engineering Course. *IEEE Trans. Educ.* **56**, 430–435 (2013).
126. Kim, M. K., Kim, S. M., Khera, O. & Getman, J. The experience of three flipped classrooms in an urban university: an exploration of design principles. *Internet High. Educ.* **22**, 37–50 (2014).
127. Wilson, S. G. The Flipped Class: A Method to Address the Challenges of an Undergraduate Statistics Course. *Teach. Psychol.* 0098628313487461 (2013).
doi:10.1177/0098628313487461
128. Warter-Perez, N. & Dong, J. Flipping the classroom: How to embed inquiry and design projects into a digital engineering lecture. in *Proceedings of the 2012 ASEE PSW Section Conference* (American Society for Engineering Education Washington DC, 2012).

129. Stelzer, T., Brookes, D. T., Gladding, G. & Mestre, J. P. Impact of multimedia learning modules on an introductory course on electricity and magnetism. *Am. J. Phys.* **78**, 755–759 (2010).
130. Moravec, M., Williams, A., Aguilar-Roca, N. & O’Dowd, D. K. Learn before Lecture: A Strategy That Improves Learning Outcomes in a Large Introductory Biology Class. *CBE-Life Sci. Educ.* **9**, 473–481 (2010).
131. Young, T. P., Bailey, C. J., Guptill, M., Thorp, A. W. & Thomas, T. L. The Flipped Classroom: A Modality for Mixed Asynchronous and Synchronous Learning in a Residency Program. *West. J. Emerg. Med.* **15**, 938–944 (2014).
132. Pierce, R. & Fox, J. Vodcasts and Active-Learning Exercises in a “Flipped Classroom” Model of a Renal Pharmacotherapy Module. *Am. J. Pharm. Educ.* **76**, (2012).
133. Robbins, N. B. & Heiberger, R. M. Plotting Likert and other rating scales. in *Proceedings of the 2011 Joint Statistical Meeting* (2011).